ISTANBUL BİLGİ UNIVERSITY
INSTITUTE OF GRADUATE PROGRAMS
ELECTRICAL & ELECTRONICS ENGINEERING MASTER
DEGREE PROGRAM

DESIGN, FABRICATION, AND IMPLEMENTATION OF A LOW-COST PIEZORESISTIVE FORCE ENCODING SENSOR

Ömer Gökalp Akcan
119815029

Assoc. Prof. Yiğit Dağhan Gökdel
Assist. Prof. Eray A. Baran

ISTANBUL
2022

DESIGN, FABRICATION, AND IMPLEMENTATION OF A LOW-COST PIEZORESISTIVE FORCE ENCODING SENSOR

DÜŞÜK MALİYETLİ BİR PİYEZOREZİSTİF KUVVET KODLAMA SENSÖRÜNÜN TASARIMI, ÜRETİMİ, VE UYGULAMASI

Ömer Gökalp Akcan

119815029

APPROVED BY:

Thesis Supervisor	**:** Assoc. Prof. Yiğit Dağhan Gökdel (Istanbul Bilgi University)	....
Thesis Co-supervisor	**:** Assist. Prof. Eray A. Baran (Istanbul Bilgi University)	....
Member of a Jury	**:** Assoc. Prof. Onur Ferhanoğlu (Istanbul Technical University)	....
Member of a Jury	**:** Assist. Prof. Baykal Sarıoğlu (Istanbul Bilgi University)	....
Member of a Jury	**:** Assist. Prof. Mehmet Ayyıldız (Istanbul Bilgi University)	....

Date of approval: 20.01.2022

Total number of pages:

Keywords (English):

1) Paper substrate

2) Piezoresistive sensor

3) Force sensor

4) Disposable device

5) Soft robots

Keywords (Turkish):

1) Kağıt alt tabaka

2) Piyezorezistif sensör

3) Kuvvet Sensörü

4) Kullan at cihaz

5) Yumuşak robot

Fahre fort, übe nicht allein die Kunst,
sondern dringe auch in ihr Inneres; sie verdient es,
denn nur die Kunst und die Wissenschaft
erhöhen den Menschen bis zur Gottheit.

Ludwig van Beethoven

ACKNOWLEDGEMENTS

This work would not have been possible without the support, patience, and faith of many people who have a very important place in my life.

First of all, I would like to thank my thesis advisor, Assoc. Prof. Yiğit Dağhan Gökdel, with my sincere wishes. The opportunity he gave me while I was still in my first year of undergraduate has created what I am today. If we count undergraduate and graduate education, I am grateful to him for everything he has taught me for six years. His perspective, vast knowledge, kind and motivating style, and fatherly demeanor made my life and research tenacity more productive.

Another important person in my life is our dear teacher Assist. Prof. Özgür Gül. He was an unprecedented person with his unique style and character. One of the main reasons it has a very important place in my memory is that he always discusses our ideas and often rejects them, thus making us overthink and trust our minds. I, unfortunately, lost him on January 24^{th}, 2021, and will never forget the unique character who dedicated his life to academia. Rest in peace, the best researcher I have ever met. His beautiful daughter, Deniz, if you grow up and discover this thesis work one day, I would like to remember him with you.

I am very happy to recognize my thesis co-advisor, Assist. Prof. Eray Baran, and to have carried out this study with him. His competence in motion control systems expanded the scope of my thinking during the meetings we held. Although I met him late, I had the opportunity to work with him during my master's degree. He taught me to stay alive and proceed under all circumstances. I think he must have realized that I am an excited character because he once said to me, "think twice, speak once," while exchanging ideas on a subject. I would like to thank a lot him for his support in both my personal and professional life.

As a member of the Biosensor and Force Encoder Research Groups, I would like to thank Kuter Erdil, one of my closest friends and confidants during my undergraduate and graduate education. His camaraderie, motivation, and the fact that he brought me back to my senses while contemplating and wrestling with my mind enabled me to have a happy, peaceful and productive three years. Without his clarity and foresight ability, our studies could not have been completed. I would like to thank Tuğçe Ayraç, İpek Hilal Kacar, Berfin Gedlaç, Berkay Alçiçek, Batuhan İstanbullu and Elif Teker, who have always kept me fit with their support and entertaining nature.

I would like to thank Doğukan Korkut for his friendship, helpfulness, and kindness, who provided me with the greatest contributions to this work. Working with him was very enjoyable and instructive for me.

Finally, I would like to express my deepest gratitude to my beloved family Nevriye, Cem, and Ece Naz Akcan, and my love Ayşin Arseven. Throughout this challenging marathon, I have always felt their patience, support, faith, respect, and love for me. I am aware that I test their patience with my skeptical and stubborn character on many issues, but this has never lessened their support for me. Besides, I would like to thank my dear friends, Meral Gonca Kurt, Beliz Basiç, Buse Naz Yıldırım, Cengiz Uygur, Zahit Başyiğit, and Gautier Aubert. They are very precious people to me. We are always together and share the happiest moments of our lives, ideas, joyful times, happinesses, confusions, and what we learned. I am so glad to know them.

ABSTRACT

This thesis demonstrates design, implementation, and experimental results of a low-cost disposable flexible sensor system capable of both impact localization and measurement. Proposed flexible sensor structure utilizes a special series of Bristol paper as the main fabrication material, which is coated with electric paint graphite paste and silver paste. Implemented sensor system uses a planar absolute encoder-like sensing topology to locate the impact and has a low-cost and quick manufacturing process.

The size of the structure is 210 $mm \times 18.56$ mm with the thickness of approximately 340 μm. It has an electronic read-out consisting of three identical Wheatstone bridge circuits and instrumentation amplifiers for each bit. It can detect the external forces in the range of 0.6N to 12N with a spatial resolution of 2.4 cm and 0.55 cm in horizontal and vertical axes, respectively. The proposed sensor structure is tested in a series of experiments using a robotic setup consisted of a pantograph mechanism and a direct drive linear motor. The experiments illustrate the results with measurement sensitivity as small as 1N and proper fatigue resilience against repetitive loads.

Key words: paper substrate, piezoresistive sensor, force sensor, position sensor, disposable device, perforated structure, flexible medium, robotics system, soft robots, read-out circuit.

ÖZET

Bu tez, hem kuvvet lokalizasyonu hem de ölçüm yapabilen düşük maliyetli tek-kullanımlık esnek bir sensör sisteminin tasarımını, uygulamasını ve deneysel sonuçlarını göstermektedir. Önerilen esnek sensör yapısı, ana üretim malzemesi olarak elektrikli boya grafit macunu ve gümüş macunu ile kaplanmış özel bir dizi Bristol kağıdı kullanır. Uygulanan sensör sistemi, etkiyi bulmak için lineer mutlak kodlayıcı benzeri bir algılama topolojisi kullanır ve düşük maliyetli ve hızlı bir üretim sürecine sahiptir.

Yapının boyutu 210 $mm \times 18.56$ mm ve kalınlığı yaklaşık 340 μm'dir. Üç özdeş Wheatstone köprü devresinden ve her bir bit için enstrümantasyon amplifikatöründen oluşan bir elektronik okumaya sahiptir. Yatay ve dikey eksenlerde sırasıyla 2.4 cm ve 0.55 cm uzamsal çözünürlük ile 0.6N ila 12N aralığındaki dış kuvvetleri algılayabilir. Önerilen sensör yapısı, bir pantograf mekanizması ve bir doğrudan tahrikli lineer motordan oluşan bir robotik kurulum kullanılarak bir dizi deneyde test edilmiştir. Deneyler, 1N kadar küçük ölçüm hassasiyeti ve tekrarlayan yüklere karşı uygun yorulma direnci ile sonuçları göstermektedir.

Anahtar kelimeler: kağıt alt tabaka, piyezorezistif sensör, kuvvet sensörü, konum sensörü, Kullan at cihaz, delikli yapı, esnek ortam, robotik sistem, yumuşak robotlar, okuma devresi.

TABLE OF CONTENTS

ACKNOWLEDGEMENTS iv
ABSTRACT vi
ÖZET vii
LIST OF FIGURES x
LIST OF TABLES xvi
LIST OF SYMBOL xvii
LIST OF ACRONYMS/ABBREVIATIONS 1
1. INTRODUCTION 2
2. PROPOSED SYSTEM 5
3. PROPOSED DESIGN 8
3.1. Paper Substrate 8
3.2. Piezoresistive Layer 11
3.3. Hole Ablation 20
3.4. Proposed Force Encoder Structure 27
4. IMPLEMENTATION 32
4.1. Materials 32
4.2. Methods 34
4.3. Proposed Fabrication Process 35
5. ELECTRONICS 39
5.1. Proposed Read-Out Circuitry 39
6. EXPERIMENTS 44
6.1. Test Setup 44
6.2. Test Results 46
7. DISCUSSION 54
8. CONCLUSIONS AND FUTURE WORKS 56
REFERENCES 57
APPENDIX A: MANUFACTURING OF THE SILK STENCILS 67
APPENDIX B: DATASHEETS 68

B.1. Graphite 68
B.2. Silver Ink 69
B.3. Dual Edge Connector 70
B.4. Silicone Mold 71
APPENDIX C: Main Algorithm 72
APPENDIX D: Main Algorithm Library-1 83
APPENDIX E: Main Algorithm Library-2 87

LIST OF FIGURES

2.1 The system diagram of the proposed piezoresistive linear absolute force encoder system. System harbors a paper-based piezoresistive sensor along with 3D silicone mold structure, a read-out circuit and, a real-time controller (Dynomotion® KFlop & KAnalog series motion controller). 5

3.1 Effect of three different substrate materials are observed by bending them with an increasing arc length. The arc lengths of (a) are between 140 mm to 95 mm, (b) are between 90 mm to 45 mm, and (c) are between 40 mm to 30 mm. 9

3.2 Behaviour of three different substrates for various bending ratio. The fitting line equations for (a) the Bristol paper, (b) Alex Schöller paper, and (c) Photography paper are $2.1715x^{-0.967}$, $4.908e^{-0.084}$, and $17.255e^{-0.073x}$, respectively. 10

3.3 Conceptual drawing that demonstrates the working principle of the proposed 3-bit linear absolute encoder structure. The structure consists of eight different segments, three different conductive electrical paths (EP), and various graphite coatings. It is important to note that the graphite coatings actually forms a 3-bit linear absolute encoder as in its truth table. 12

3.4 Photo of fabricated piezoresistive lines with alternating widths, all measurements are in micrometers. 14

3.5 Close up view of the piezoresistive lines fabricated with various widths. The design values of the widths of the lines are located in the upper right corner of each of them. 15

3.6 Plot of the widths of the fabricated piezoresistive lines (w_l) and designed piezoresistive lines drawn with reference to the minimum reproducible and repeatable piezoresistive line width (230 μm). . . 16

3.7 Illustration of piezoresistive layer designs M1 and M2. w_{gap} values are 1200 µm and 270 µm for M1 and M2 model, respectively. . . 17
3.8 Photo of fabricated piezoresistive lines with changing gaps, all measurements are in micrometers. 18
3.9 Close up view of the piezoresistive lines fabricated with various gaps. The design values of the gap of the lines are located in the upper right corner of each of them. 19
3.10 Plot of the designed versus fabricated gap distance (w_{gap}) between the adjacent piezoresistive line pairs. The first value where the materials do not diffuse to each other is the eighth data. 20
3.11 The behaviour of Bristol paper for various layers. The fitting line equations for the single layer, and double layer are $2.1735x^{-0.967}$, and $3.3653x^{-0.902}$, respectively. 21
3.12 The fabricated view of the holes having 1 mm diameter that are cut by increasing the power level by 1% from 50% to 100% while keeping the speed and frequency constant. 22
3.13 Fabricated view of holes having 1 mm diameter that are cut by increasing speed by 1% from 50% to 100% with determined 67% power level. 22
3.14 Plot of the fabricated holes values which are designed as 1000 μm, according to the various laser speed level testing to determine the most appropriate laser speed level. 23
3.15 Fabrication view of various holes designed from 20 μm to 1000 μm with 20 μm resolution cut by laser's determined 67% power, 100% speed and 5000 Hz frequency. 23
3.16 Close up view of ablated holes with various diameters. The design values of the holes are located in the upper left corner of each of them. 24
3.17 Plot of the test of the perforation of designed holes versus ablated holes that are cut under the optimized values of power, speed, and frequency of the laser, is emphasized. 25

3.18 Simulation results of ablated holes with various hole diameters within a defined segment area ($L_{g3} \times w_p$): (a) designed as 820 μm and fabricated as 980 μm, (b) designed as 760 μm and fabricated as 935 μm, (c) designed as 680 μm and fabricated as 839 μm, (d) designed as 620 μm and fabricated as 755 μm, (e) designed as 560 μm and fabricated as 678 μm, and (f) designed as 500μm and fabricated as 593 μm. 25

3.19 The fabrication view of the gap values that is between the determined 0.5 μm diameter designed holes changing from 20 μm to 1000 μm with 20 μm resolution, cut by laser's determined 67% power, 100% speed and 5000 Hz frequency. 27

3.20 Simulation results of ablated holes at various pattern within a defined segment area ($L_{g3} \times w_p$): (a) non-ablated, (b) ablated with 1500 μm gap, (c) ablated with 1000 μm gap, (d) ablated with 500 μm gap, (e) ablated with the minimum producible gap of 380 μm, and (f) all-ablated holes. 27

3.21 Technical drawing of the proposed 3-bit paper-based linear absolute force encoder structure and its design parameters. (a) The top view of the paper-based sensing structure that harbors eight segments. (b) a close-up view of the piezoresistive lines and ablated holes. (c) a side view of the sensing structure. 28

3.22 Technical modelling of the proposed silicone molding body along with the paper-based piezoresistive force encoder sensor and its design parameters. (a) top view of the upper part of the silicone mold structure. (b) side view of the upper part of the silicone mold structure. (c) side view of the base part of the silicone mold structure. (d) 3D view of the structure. This silicone mold structure protects the sensing structure and electronics circuits and reduces the force exerting active area, and, in turn, increases the stress acting a piezoresistive layer. 30

4.1 Illustration of the fabrication process of the linear absolute encoder force sensor. (a) Ag paste coated onto the Strathmore® 400 series Bristol paper as a base material with stencil mask (mask I) using silk screen printing method. (b) graphite paste coated onto the Ag coated Strathmore® 400 series Bristol paper with stencil mask (mask II) using silk screen printing method. (c) laser ablation (Epilog Mini 18, 30W). 35

4.2 (a) view of the silk stencil (mask I) to coat Ag paste onto the Strathmore Bristol paper, (b) view of the silk stencil (mask II) to coat graphite paste. (c) close up view of emulsified, and (d) open pores of the mask. 36

4.3 Side view of the paper-based structure sandwiched in between two silicone molds. The sensing system is getting poked with the linear motor tip. The gap between the upper and lower parts of the silicone mold S_{GAP} completely closes when a force of 12N or higher is exerted. 37

4.4 (a) The fabricated view of a paper-based piezoresistive linear absolute force encoder, (b) a close-up view of Ag and graphite layers along with its perforated structure, (c) microscope view of the fibrous structure of the Strathmore® 400 series Bristol paper with a 20X magnification ratio, and (d) microscope view of the graphite printing onto the paper substrate with a 20X magnification. 38

5.1 Schematics of conventional read-out circuits. (a) Voltage divider circuit, (b) Wheatstone bridge circuit. 39

5.2 The block diagram of the proposed electronic read-out circuitry that composed of a Wheatstone bridge circuit with one positively changing piezoresistor and a subsequent instrumental amplifier, INA118P, to amplify the voltage signal acquired through the resistance change. 40

5.3 Simplified schematic of the instrumental amplifiers (Texas Instruments® INA118P). 41

5.4 (a) and (b) top and bottom views of the schematic of the proposed electronic read-out circuit. (c) and (d) top and bottom views of the printed circuit board for the proposed electronic read-out circuit. An implemented PCB has dimensions of 54 *mm* x 44 *mm* and its components are shown inset. 42
5.5 Plot of the output voltage change (ΔV) as a function of resistance change (ΔR). Blue line corresponds to the theoretical results of the proposed read-out circuit, whereas red line corresponds to the experimental results of the system with implemented PCB. 43
6.1 View of the experimental setup used to monitor magnitude and localization of the exerted force on the proposed sensing system. . 45
6.2 A calibration graph of the force encoder sensor shows the hysteresis behaviour of the proposed sensor by plotting the normalized voltage changes versus the bending force. The smooth lines represent the incremental F_{load} dependent ΔV/V value, whereas the dashed lines represent the gradually decreasing load force from 14N to zero. . . 47
6.3 Illustrates the performance of the sensor while getting actuated in the most sensitive linear region. The dashed line in the this part represents the curve fitted equation of $y = 0.15x - 0.0686$ with an R-squared value of 0.99. 48
6.4 The paper-based sensor is continuously triggered on the x-direction with the help of the pantograph robotic arm. Shows the analog output of the sensor system. 49
6.5 The paper-based sensor is continuously triggered on the x-direction with the help of the pantograph robotic arm. Plots the digital version of the same output after careful thresholding. 50
6.6 The output voltage of the system under the application of 1N point-forces with period 1.25 seconds. 51
6.7 The output voltage of the system under the application of 1N static forces with period of 20 seconds, together with their respective error values. 52

6.8 The output voltage of the system under combined application of 1N point-force and static force with the average of 0.3 seconds time response. 53
A.1 The production stages of the silk stencil which using for the fabrication method of screen-printing. 67

LIST OF TABLES

3.1 Constraints of our proposed paper-based piezoresistive force encoding sensor. . . . 11
3.2 Designed and average fabricated values of the piezoresistive line width (w_l) with their accuracy and precision rates. . . . 17
3.3 Designed and fabricated values of the gap (w_{gap}) between adjacent piezoresistive line pairs with their accuracy and precision rates. . . 21
3.4 Designed and ablated values of the hole diameters (w_o) with their accuracy and precision rates. . . . 26
3.5 Parameters and related values of the proposed system indicated in Figures 3.3, 3.21, and 3.22. . . . 31
4.1 Comparison of the features of the selected elastic dielectric materials. 33
4.2 Comparison of the features of the selected conductive materials. . . 34
5.1 Pin functions of Texas Instruments® INA118P. . . . 41
7.1 Comparison of specifications of our proposed paper-based piezoresistive force encoding sensor regarding its detection capability of the force magnitude and its impact localization to the other works. 55

LIST OF SYMBOL

E	Modulus of elasticity
E_{eff}	Effective Young's Modulus
F_{load}	Force loading of linear motor
G	Gain of the instrumental amplifier
L_c	Length of the silicone mold bulge
L_{con1}	Length of the connector port
L_{con2}	Length of the connector
L_g	Length of the piezoresistive line
L_{g_3}	Length of the graphite layer on one segment
L_h	Distance between the silicone mold bulges
L_{oo}	Horizontal distance between two ablated holes
L_{p_1}	Length of eight segment
L_{p_2}	Length of the force encoder
L_{pad}	Length of the contact pad
L_{pcb}	Length of the PCB housing
L_s	Length of the paper strip
L_{seg}	Length of the silicon region for eight segment
L_{sm}	Length of the silicon mold
R	Electrical resistance
R_G	Gain setting resistance
R_{REF}	Reference resistance
R_{PR}	Resistance value of piezoresistive layer
S_{GAP}	Gap between the upper and lower parts of silicone mold.
t_c	Thickness of the silicone mold bulge
t_{cl}	Thickness of the silver layer
t_g	Thickness of the graphite layer
t_p	Thickness of the paper substrate
t_{s1}	Thickness of the upper part of the silicon mold

t_{s2}	Thickness of the base part of the silicon mold
V_{exp}	Experimental results of the voltage change
V_{IN}	Input voltage
V_{IN-}	Negative input voltage
V_{IN+}	Positive input voltage
V_{-}, V_{EE}	Negative voltage supply
V_{+}, V_{CC}	Positive voltage supply
V_{teo}	Theoretical results of the voltage change
V_{OUT}	Output voltage
w_{bit}	Distance between each graphite layer bit
w_{cl}	Width of the silver line
w_{con1}	Width the connector
w_{con2}	Width the connector port
w_{ear}	Width of the ear
w_{g}	Width of the graphite layer
w_{gap}	Distance between two graphite lines
w_{l}	Width of the graphite line
w_{o}	Diameter of the ablated hole
w_{ol}	Distance between the hole and graphite line
w_{oo}	Vertical distance between two ablated holes
w_{p}	Width of the force encoder
w_{pad}	Width of the contact pad
w_{pcb}	Width of the PCB housing
w_{s}	Width of the paper strip
w_{seg}	Width of the silicon region for eight segment
$\delta_{AA'}$	Contact area deflection
σ_{max}	Maximum stress
ρ	Conductivity of the material

LIST OF ACRONYMS/ABBREVIATIONS

CMRR	Common-mode rejection ratio
EP	Electrical path
FEM	Finite element modelling
GND	Ground
INA	Instrumentation amplifier
IPA	Isopropyl alcohol
PCB	Printed circuit board
PDMS	polydimethylsiloxane
PLA	Polylactic acid
PR	Piezoresistor
PU	polyurethane
PVDF	polyvinylidene fluoride
RMSE	Root mean squared error
SNR	Signal-to-noise ratio

1. INTRODUCTION

In recent years, flexible sensing techniques have gained attention due to their widespread use in industrial and medical applications. Carrying the potential for a relatively low-cost, decent performance and durability, flexible sensors can provide solutions in various fields such as human motion and health monitoring [1], intelligent braille recognition [2], robotics [3], physical and chemical sensing [4] and smart prosthetics and textile [5, 6]. The fundamental advantage of a flexible sensor also referred to as a wearable or flexible sensor, lies in the feasibility of temporary topology variation depending on the exerted pressure and several intrinsic parameters like low Young's Modulus value. Hence, these sensors prove to be useful for impact localization, and measurement for different applications [7, 8]. A variety of flexible materials such as polyimide [9–11], polydimethylsiloxane (PDMS) [12–14], polyurethane (PU) [15], polyvinylidene fluoride (PVDF) [16–18], polymer [19, 20] and hydrogel [21–23] have been used as the main substrate for the fabrication of these flexible sensors.

The operational principles of these flexible sensors, on the other hand, range from the traditional capacitive [24] and strain-based measurement technologies [25,26] to the more recently adopted triboelectric/tactile [27,28] or piezoresistive (PR) [29,30] sensing methods. Among the existing measurement techniques, piezoresistive materials have been widely used for flexible sensing applications due to their considerably low costs and ease of fabrication. Additionally, the piezoresistive materials come with the advantages of firm adherence to a vast majority of coating surfaces and considerably high response to action rates generated by external excitation (i.e., mechanical forces).

The topological structure of the soft measurement devices also plays a crucial role in producing specific sensing systems. Various different topologies have been reported to acquire high sensitivity systems such as bucky paper structure [31], bump structure [32,33], micro-pillar structure [34,35], coplanar structure [36], Cracking structure [37], matrix structure [38, 39] and multi-layered structure [40, 41] for force and pressure detection sensors. The majority of those structures require dedicated and costly production technologies. Moreover, in practical applications, the forces applied over any one of those structures are often not optimized to a specific direction which in turn yields deformations in the lateral directions.

Looking from the application point of view, soft tactile sensors have predominantly been required by the robotic systems interacting with the surrounding environment. The recent advances in soft robotic applications increase the demand for such flexible sensing systems. Concentrating on this gap, a skin-like flexible electronic system for compact and reversible assembly of soft robots has been proposed, which uses a relatively complex circuitry, and fabrication process [42]. A similar robotic skin structure is proposed in [43] through the utilization of a piezoresistive pressure sensor with a polyimide-based flexible and low-cost material, where the complexity in the electronic circuitry is compensated by the simplicity in the fabrication technique. The real-time application compatibility issue is addressed with enhanced sensitivity on a relatively large contact area for the flexible pressure, force and tactile sensors respectively in [44], [45] and [46]. However, complicated fabrication processes in the production phase come with the drawback of high costs, which limit the widespread use of those sensors. Similar trade-offs between the cost and the sensitivity can be observed in stretchable smart skin-inspired sensors [47], and capacitive ionic sensors [48] used in multi-functional robotic position, force, and tactile sensing applications.

Focusing on the demand for a low-cost and uncomplicated fabrication method, flexible and robust sensor structures for robotic and artificial skin applications have been proposed in [49], and [50], providing solutions for an effective and precise localization with sufficient resolution. However, with the capacitive structures yielding slight variations due to the applied force, relatively low sensitivity levels and small detection ranges are attained in those studies. Therefore, the utilization of sensitive, repeatable, and low-cost, flexible sensors in robotic applications with considerably fast fabrication processes is still an open-ended research problem.

Addressing this problem, the presented study demonstrates a piezoresistive force encoder structure for the realization of force sensing and localization on soft surfaces. The novelty of the presented structure lies (i) in an absolute encoder-like sensing topology (ii) being tested on disposable materials, which brings the advantage of reduced cost and ease of manufacturing for soft sensing applications. The proposed sensor structure utilizes Strathmore® 400 series Bristol paper coated Bare Conductive graphite paste as an elastic dielectric and silver paste as a connector between peripheral electronic circuitry and force sensing unit. The absolute encoder topology reduces the requirements of the complex read-out circuitry, which is required by matrix-wise distributed groups of sensors. The proposed sensor structure has been tested on several experiments using feedback-controlled precise robotic systems. The experiment results validate the proposed structure's efficiency and efficacy by consistently accurate measurements, short response times to the applied external forces, and a considerably high level of precision even under relatively small external loads.

The rest of this paper is organized as follows: In Chapter 2, the proposed system and operation principle is presented. Afterwards, the proposed design and its fabrication process are elaborated in Chapter 3 and 4, respectively. Afterward, electronic read-out circuitry is presented in Chapter 5. The experimental setup integrated into the sensing structure and its results are explained and demonstrated in Chapter 6. Finally, a comparative evaluation of the experimental results is presented considering the novelties in this study and the existing literature in Chapter 7 and 8.

2. PROPOSED SYSTEM

Proposed system is illustrated in Figure 2.1. It harbors three fundamental components. These are (i) a robotic system, (ii) a novel low-cost position and force sensing device that consists of a 3-bit paper-based linear absolute encoder, (iii) a customized read-out circuitry. A generic pantograph robot is opted in this study with the main aim of testing the overall performance of the novel and low-cost sensing device that is presented in this work. The novelty of this work lies in the position and force sensing device of this illustrated system.

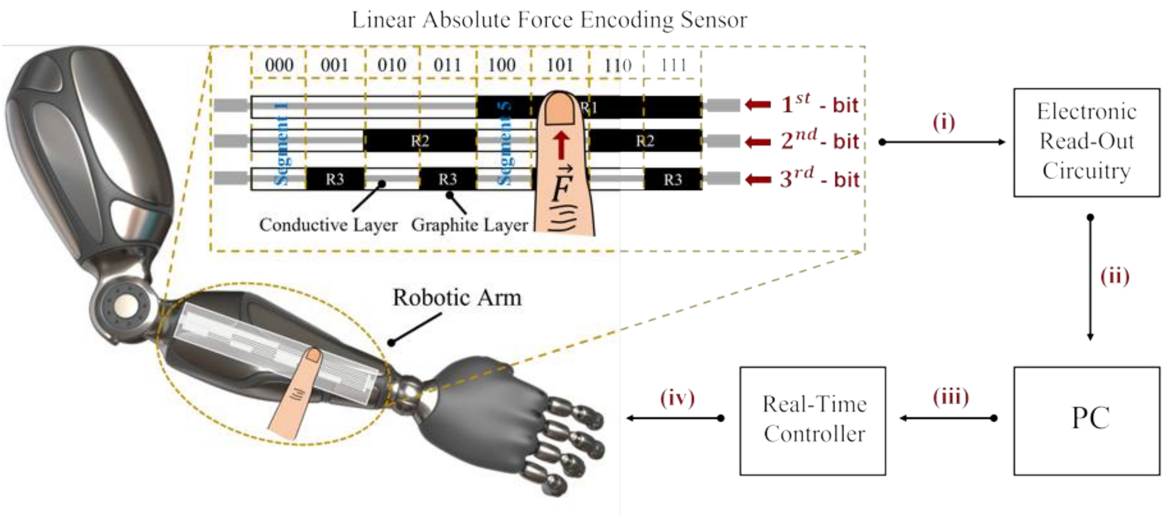

Figure 2.1: The system diagram of the proposed piezoresistive linear absolute force encoder system. System harbors a paper-based piezoresistive sensor along with 3D silicone mold structure, a read-out circuit and, a real-time controller (Dynomotion® KFlop & KAnalog series motion controller).

This device has two essential parts (1) a paper-based linear absolute encoder sandwiched between two silicone layers that act as a performance-improving protective skin which ensures that a force is applied to a particular area on the sensor and the pressure is increased in this area, recovers itself after removing the exerted force and prevents permanent deformation on the paper structure, and (2) a detecting circuitry that is basically composed of a conventional Wheatstone Bridge circuitry and a following instrumentation amplifier circuit with a high signal-to-noise ratio (SNR).

Generic absolute encoder structures are position measurement systems that are typically used in electrical motors. In this work, we prefer the same detecting methodology for the measurement and localization of the force signal in a planar form. This proposed linear absolute force encoder system uses a low-cost Strathmore® 400 series Bristol paper as the main substrate, Bare Conductive® Electric paint graphite for detection, and silver paste (Baku Bk-426) for electrical connections. This novel approach makes the structure low-cost and disposable whereas safely providing the targeted position and force data as feedback signals to the system.

As it is emphasized in Section 1, numerous collisions having different modalities and intensity values occur between moving robotic system and obstacles along its path. The robotic system represents a general use case both for the validation and actual implementation of the sensor structure. In order to validate the system, a pantograph robot working together with a linear motor is implemented. Here, the pantograph system is used to provide the precise spacing between the points of interaction and the linear motor is used to apply a controlled force reference on the precisely positioned sensor. The force and position of collisions arising in part (i) in Figure 2.1 can be detected by our proposed low-cost sensing structure in order to improve the performance of the autonomous system significantly.

The linear absolute force encoder structure, which is located at the heart of the presented study. When a force is applied onto this force encoding structure on one of the segments shown in Figure 2.1, the topology of the piezoresistive graphite layer coated on the paper substrate changes. Through the deformation caused by the external force, a considerable change in resistance value at the point of interaction can be sensed. This resistance change is transformed to a voltage signal through the readout circuitry. An instrumentation amplifier following a generic Wheatstone Bridge circuit is used in order to take the output signal of the sensor and precisely transform it to a voltage signal that is fed into the real-time controller, as shown in parts (i) & (ii) of Figure 2.1, respectively.

A real-time controller (Dynomotion® KFlop & KAnalog series motion controller) is used to deliver a voltage signal from the read-out circuit to process data in discrete and continuum environments. The impact position is calculated using the standard absolute encoder logic: The application of an external force on anyone of the rows changes the measured resistance value. By appropriate binary thresholding of each row, one can convert the measured analogue voltage to a digital output. The positions and the force values of the collisions are collected with software run on a PC. The same real-time controller is also used to drive the robotic system.

3. PROPOSED DESIGN

This chapter presents design produce of the paper-based piezoresistive 3-bit force encoding sensor. Section 3.1 explains how determine the substrate material. Subsequently, Section 3.2 discusses the design of piezoresistive graphite layer. Section 3.3 discusses the design of ablation hole. Finally, Section 3.4 summarizes the proposed force encoder structure and share its design parameters and related dimensions.

3.1. Paper Substrate

Paper is used as the substrate material in this work. Therefore, its material properties and behaviours play an essential role in developing a sufficiently flexible, robust, and low-cost force encoding sensor. For selecting the most suitable substrate material, various papers were observed. A silver paste as a conduction line, and a piezoresistive material, as a sensing material, is coated on three different substrates with a single-line (Strip) form. The materials that are coated are examined in terms of stress response, durability, and compatibility under the different bending ratios [51].

We chose three different substrates, namely of Strathmore® 400 series Bristol paper, Alex Schöller paper, and Photography paper. These paper types are chosen due to their flexibility, robustness, and porous structures. A structure with different radius and arc lengths as illustrated in Figure 3.1 is designed for our experimental setup. The arc lengths consist of 23 different semicircles on the structure changing from 30 *mm* to 140 *mm* with a step size of 5 *mm*, corresponding to a radius of 9.54 *mm* to 44.56 *mm*. This testing structure is fabricated from PLA (Polylactic acid) material using a 3D printer [51].

This structure is implemented to observe the resistance changes resulting from 23 different bending ratios. Thereby, the substrate material and its optimal bending ratio is determined according to the error rate obtained from the experiments.

(a) (b) (c)

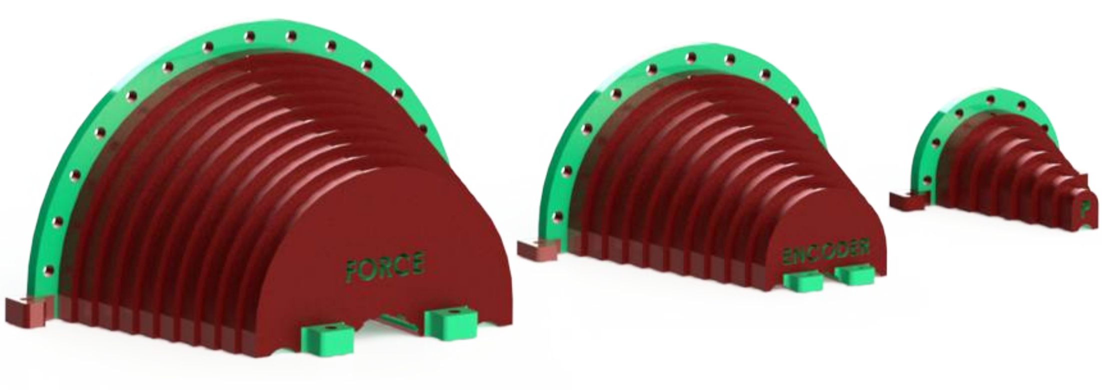

Figure 3.1: Effect of three different substrate materials are observed by bending them with an increasing arc length. The arc lengths of (a) are between 140 mm to 95 mm, (b) are between 90 mm to 45 mm, and (c) are between 40 mm to 30 mm.

Figure 3.2 plots the normalized resistance changes $\Delta R/R$ of the strip strain sensors fabricated with three different substrates under the application of gradually augmenting bending ratio with 23 different radius values.Initial resistance values of the strain sensors are taken as an initial reference point when calculating the normalized resistance change $\Delta R/R$.

When the radius-dependent bending ratio value is gradually increased from 30 mm to 140 mm with a step size of 5 mm, corresponding to a radius of 9.54 mm to 44.56 mm, the normalized resistance change ($\Delta R/R$) of the Strathmore® 400 series Bristol paper is monitored. It is seen that the normalized resistance change decreases from 0.2291 to 0.0586 Ω/Ω with an average error margins of 0.0239 V/V as emphasized in Figure 3.2. The equation and R-squared value of the fitting line are determined in Figure 3.2 as $2.1715x^{-0.967}$ and 0.9395, respectively.

Moreover, it is also reported for the other strips that when their radius-dependent bending ratio value is gradually increased from 30 mm to 140 mm with a step size of 5 mm, corresponding to a radius of 9.54 mm to 44.56 mm, the normalized resistance change ($\Delta R/R$) changes irregularly from 1.279 to 0.1421 Ω/Ω with an average error

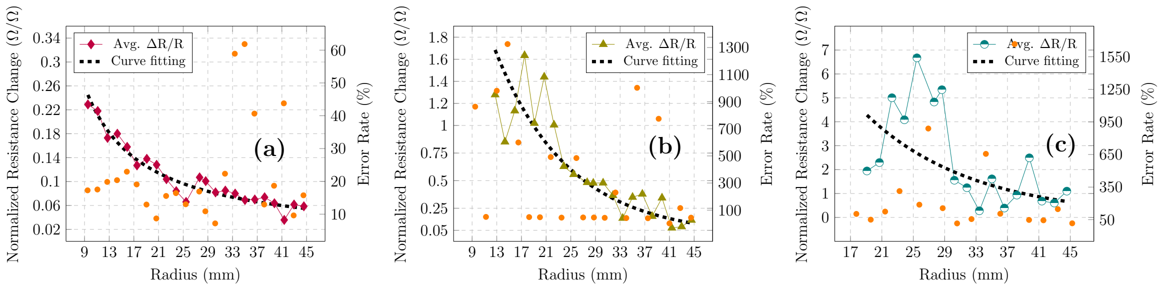

Figure 3.2: Behaviour of three different substrates for various bending ratio. The fitting line equations for (a) the Bristol paper, (b) Alex Schöller paper, and (c) Photography paper are $2.1715x^{-0.967}$, $4.908e^{-0.084}$, and $17.255e^{-0.073x}$, respectively.

margins of 0.652 V/V, and 1.944 to 1.09 Ω/Ω with an average error margins of 2.275 V/V, for Alex Schöller paper, and Photography paper, respectively, as shown in Figure 3.2. The equations and R-squared values of the fitting lines are determined in the Figure 3.2 as $4.908e^{-0.084}$ and 0.7222 for the Alex Schöller paper and $17.255e^{-0.073x}$ and 0.2815 for the Photography paper.

As a result of these experiments, it is observed that the surface structure of photographic paper is not suitable for the adhesion of graphite. Since it does not have a porous structure. Consequently, plastic deformations and fractures occur in the graphite layer at high bending rates. However, Strathmore®00 series Bristol paper and Alex Schöller paper has a porous structure. Due to their high surface adhesion and absorbability of piezoresistive material, it is determined that these papers still contain the piezoresistive material even at high bending rates. Strathmore®00 series Bristol paper has lowest error according to the results. It can be seen that the normalized resistance changes of the sensors fabricated with Strathmore®00 series Bristol paper are more linear under varying bending ratios compared to Alex Schöller paper and Photography paper. Additionally, bending with a radius of 30.2394 mm, and hence 95 mm arc length, is selected as an optimal point with a lowest error rate 7.18 % for the piezoresistive strain sensor produced with Strathmore®00 series Bristol paper [51].

Table 3.1: Constraints of our proposed paper-based piezoresistive force encoding sensor.

	Design Constraints
(1)	$L_{p2} \approx$ average human arm circumference.
(2)	$420\ mm^2 \leqslant$ Spatial resolution $(L_{g_3} \times w_p) \leqslant 580\ mm^2$
(3)	$17.5\ mm \leqslant L_{g3}$.
(4)	Serpentine piezoresistive layer topology
(5)	w_l, w_g, $w_{gap} \leqslant$ Error rate between designed and fabricated (%5)

3.2. Piezoresistive Layer

Piezoresistive effect is used as a sensing mechanism to measure resistance changes in this work. Dimensions and design of the piezoresistive layer play a vital role to develop and achieving a more sensitive and robust force encoder structure. In order to optimize the piezoresistive layer, some constraints are necessary to consider. For work, important constraints are tabulated in Table 3.1. The listed constraints specify the length of the force encoding sensor (L_{p2}), the impact are of an average human finger ($L_{g_3} \times w_p$), the width of the impact area of a human finger under maximum force (L_{g3}), the piezoresistive layer topology associated with the precisely sensing, and finally the maximum error rates required of the sensing mechanism dimensions to detect exerting force magnitude and its location with high-sensitivity.

Linear absolute encoder structure is preferred as the force encoding sensor structure in this thesis. The working logic of the linear absolute encoder structure is based on a binary coding system in order to detect the location and magnitude of the applied force. A conceptual drawing demonstrating the working principle of the linear absolute force encoder is depicted in Figure 3.3. In this design, the 3-bit force encoder has eight segments, as emphasized in the Figure 3.3. Each segment has the same size ($L_{g_3} \times w_p$) and is composed of three rows, one under the other. As shown in Figure 3.3, the first four consecutive columns (C1 to C4) of the first row (R1) do not have any graphite coating, whereas the remaining consecutive columns (C5 to C8) of the same row are all coated with a thin layer of graphite. The first row of each segment is

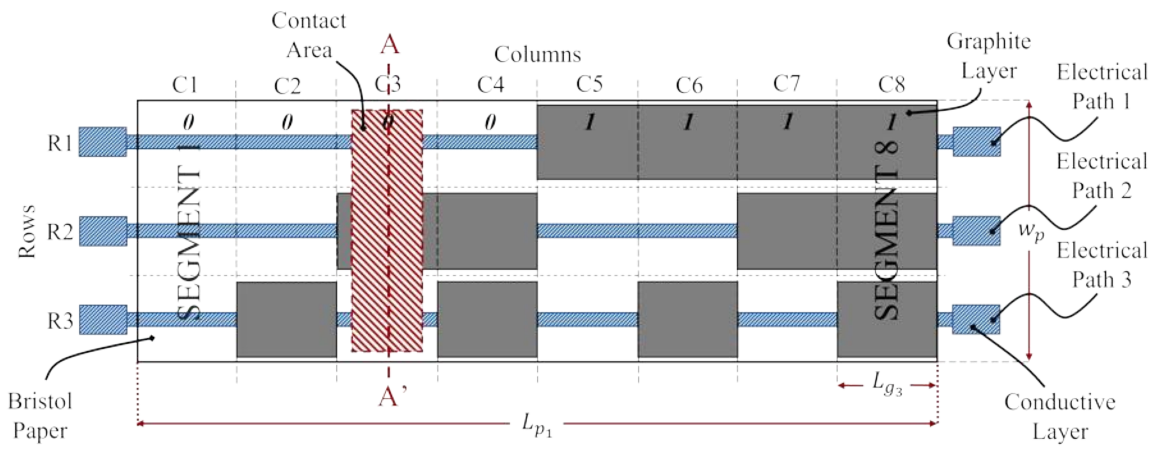

Figure 3.3: Conceptual drawing that demonstrates the working principle of the proposed 3-bit linear absolute encoder structure. The structure consists of eight different segments, three different conductive electrical paths (EP), and various graphite coatings. It is important to note that the graphite coatings actually forms a 3-bit linear absolute encoder as in its truth table.

electrically connected to each other thanks to a silver conductive path. With this form, graphite-coated areas would correspond to high digital [52]. In contrast, uncoated areas would represent a digital low in the subsequent electronic detection part as illustrated in Figure 3.3. The other rows (R2 and R3) of the segments are processed with the same method to form a 3-bit truth table on the proposed linear absolute force encoder structure.

Let us presume that a force is applied on Segment 3 of the linear absolute force encoder structure given in Figure 3.3. A deformation occurs on each row (R1 to R3) of column 3 (C3). The exerted force and hence the corresponding deformation do not have any significant electrical effect because R1 and R3 of this segment do not include any graphite coating but just conductive layers to ensure the electrical connection. On the other hand, the same deformation forms an effective resistance change in the graphite layer coated on R2 of Segment 3. In that way, even though we apply a considerable force on Segment 3, we read a substantial resistance change only from the electrical path (EP) II but not from EP I and III. Therefore, one should note that each segment outputs a different electrical signal when a force is exerted. For instance, a force applied on Segment 3 yields to a digital read-out of 010, whereas one can acquire a read-out of 110 once the same force is applied on Segment 7. Consequently, the proposed linear absolute encoder structure enables an optimum way of detecting the externally applied force location.

First three constraints are about the length of the proposed linear absolute encoding structure, an average human finger impact area, and the spread size of the average human finger under maximum force. The length of the proposed linear absolute force encoder structure (L_{p2}) is chosen as 210 mm being the width of a generic A4 sheet that is comparable to an average human arm circumference [53]. The dimensions of the electrical pads (EP) are chosen according to the Dual edge card connector (Amtek® 5FP1B1SND-08T0BLT-01) structure which is used as a electrical connection between the read-out circuit and the sensor. The other dimensions are relatively selected according to the criteria explained above.

The length of each segment (L_{g3}) is selected to be 24 mm for the proposed structure. On the other hand, considering that the contact region of an average human finger is approximately ranging between 420 mm^2 to 580 mm^2 [54], the width of each segment (w_p) should be in the range between 17.5 mm and 24 mm. Hence, 1/16 of an A4 paper, 18.5625 mm is preferred as the desired width of the sensor (w_p). The details and the rest of the all other design parameters will be shared in Section 3.4.

The fourth constraint mentioned above is the topological structure of the piezoresistive layers. The design of the piezoresistive layer plays a significant role in order to be able to obtain a high-sensitivity and a low-cost force encoding sensor.

Well-known resistance formula is given in Equation 3.1 [55], where R represents the electrical resistance of the piezoresistive layer, ρ expresses the conductivity of the material, and L_g, w_g, and t_g symbolize length, width, and thickness of the resistor, respectively. L_g is determined according to the length of each segment (L_{g3}).

$$R = \rho \frac{L_g}{w_g t_g} \tag{3.1}$$

As seen in Equation 3.1, there are three critical parameters for increasing the resistance change of a piezoresistive line. t_g can be considered as constant assuming that we accomplish a coating process with uniform thickness. While the length of the line, L_g, is increased by using a serpentine structure, its width w_g should be decreased in order to be able to increase the sensitivity. Increasing sensitivity ensures the piezoresistive layer to sense applied low magnitude forces, and thus a slight contact can be measured. As can be seen from the equation 3.1, in order to increase the resistance of the piezoresistive layer, the width, w_g, and thickness, t_g, of the piezoresistive layer should be low, and the length, L_g, should be as long as possible. Thus, serpentine structure design for piezoresistive layer is preferred due to high-sensitivity according to the rigid topology and cost effective because less material is used.

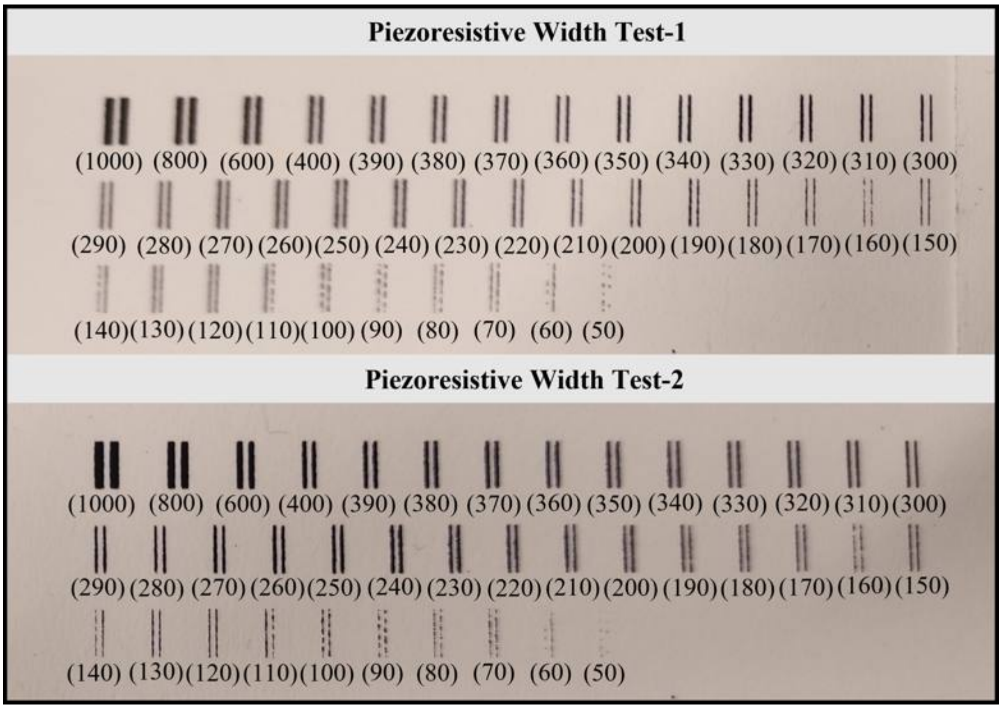

Figure 3.4: Photo of fabricated piezoresistive lines with alternating widths, all measurements are in micrometers.

For the last constraint, we performed a test to determine the piezoresistive layer width w_g that can be fabricated with the lowest-error rate and repeatability as shown in Figure 3.4. Because, we want to obtaion a precise location measurement and therefore the piezoresistive layer should not diffuse between the segments. Widths of the fabricated piezoresistive line (w_l) were designed from 50 μm to 1000 μm as shown in the in Figure 3.4. The distance between each fabricated piezoresistive line is 600 μm. After the fabrication process, the electrical connections of the lines are checked, and the first signal is received from the 230 μm piezoresistive line w_l width. For this reason, the piezoresistive line designed with a width of 230 μm is taken as the minimum feature size that ensures electrical connectivity.

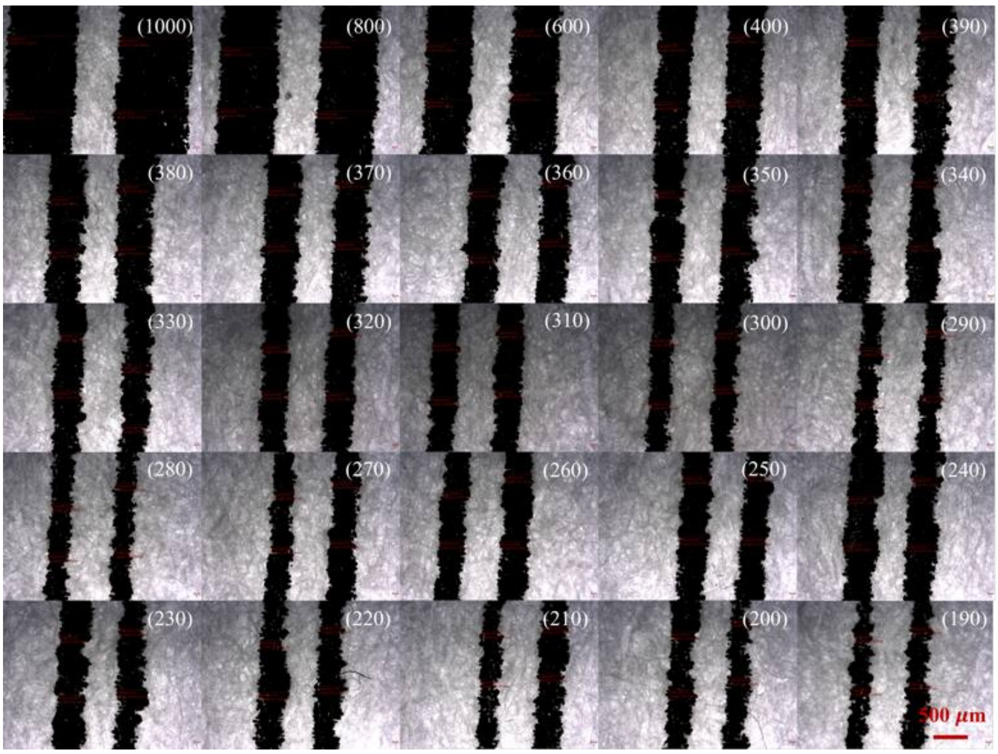

Figure 3.5: Close up view of the piezoresistive lines fabricated with various widths. The design values of the widths of the lines are located in the upper right corner of each of them.

Figure 3.5 shows the microscope views of piezoresistive lines fabricated with various sizes from 190 μm to 1000 μm. The values emphasized in Figure 3.6 and tabulated in Table 3.2 show the average of values obtained by measuring each piezoresistive line pair at different locations under the microscope.

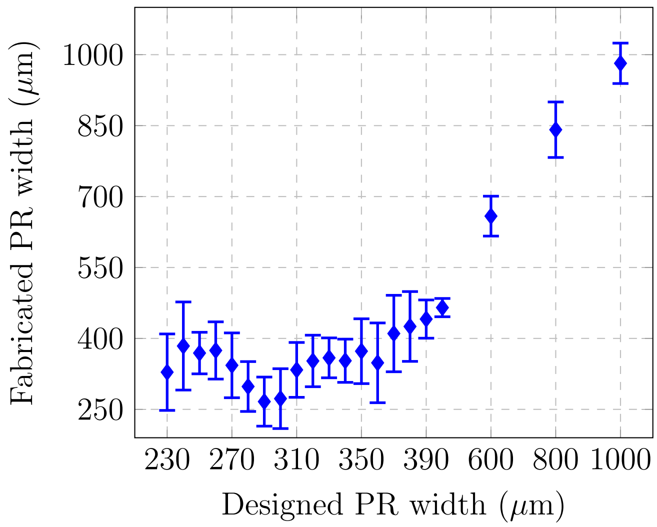

Figure 3.6: Plot of the widths of the fabricated piezoresistive lines (w_l) and designed piezoresistive lines drawn with reference to the minimum reproducible and repeatable piezoresistive line width (230 μm).

According to the test results presented in Figure 3.6 and in Table 3.2, piezoresistive line width (w_l) having 1000 μm has more high accuracy rate with 4.35% and most precision rate 2%. Considering the last constraint, piezoresistive line width (w_l), which is designed as 1000 μm and fabricated as 980 μm, is selected due to its lower diffusion with 2% precision rate.

In order to observe how many serpentine structures such as 1S-shaped, 2S-shaped, etc. the piezoresistive layer can consist of. The minimum reproducible limit of the distance between two adjacent piezoresistive lines is determined. Obtained fabrication limits are compared with ablation tests and simulations, and the most appropriate design is decided to reduce the effective Young's modulus (E_{eff}). According to the determined piezoresistive line width (w_l) and segment area ($L_{g3} \times w_p$) of the 3-bit linear force encoder sensor, possible gap distances (w_{gap}) between the piezoresistive lines were calculated, and two piezoresistive layer models were designed for possible probabilities, as illustrated in Figure 3.7.

Table 3.2: Designed and average fabricated values of the piezoresistive line width (w_l) with their accuracy and precision rates.

Designed (μm)	**Measured (μm)**	**Accuracy Rate (%)**	**Precision Rate (%)**	**Designed (μm)**	**Measured (μm)**	**Accuracy Rate (%)**	**Precision Rate (%)**
230	328.7	42.91	24.59	340	352.8	3.76	12.95
240	384	60	24.26	350	373	6.57	18.37
250	369	47.6	11.9	360	348.4	3.23	24.21
260	374.6	44.07	16.15	370	410.4	10.9	19.7
270	343	25.56	19.97	380	425.3	11.92	17.35
280	298.3	6.54	17.67	390	441	13	9.16
290	266.4	8.13	21.36	400	465.2	16.3	4.13
300	272.7	9.1	16.01	600	658.6	9.76	6.4
310	333.5	7.58	17.39	800	841.3	5.16	7.88
320	352.4	10.12	15.46	1000	980	2	4.35
330	359	8.78	11.75	-	-	-	-

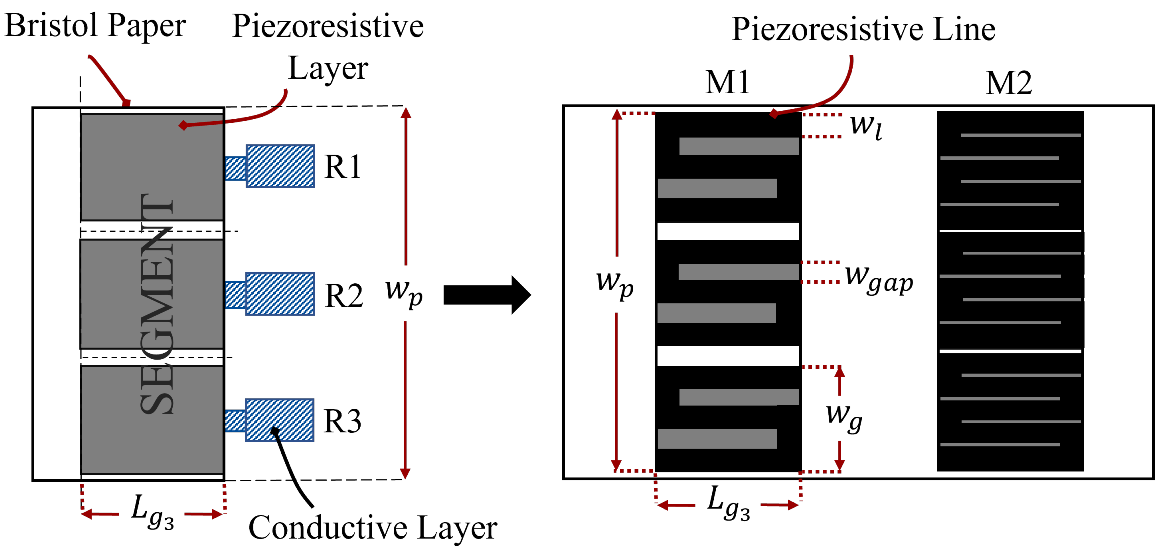

Figure 3.7: Illustration of piezoresistive layer designs M1 and M2. w_{gap} values are 1200 µm and 270 µm for M1 and M2 model, respectively.

Illustration of two different piezoresistive layer designs that can be placed in each row that are represented as R1, R2, and R3, of one segment area is given in Figure 3.7. As indicated in Figure 3.7, The piezoresistive layer structures that are represented as M1 and M2 are designed as an 1S-shaped and 2S-shaped in order to connect between segments. The models designed with determined piezoresistive line width, which is designed as 1000 μm and fabricated as 980 μm, have two different gap between adjacent piezoresistive line pairs as approximately 1200 μm and 270 μm according to the calculations in the scope of w_p. Producibility of these two gap distance were examined by the experiment presented in Figure 3.10.

In order to determine the producibility of emphasized gap distances between the two adjacent lines, different piezoresistive line pairs having a width of 1 mm and a length of 5 mm (1 mm × 5 mm) are fabricated using the silk-stencil method as shown in Figure 3.8. The distance between piezoresistive lines are changing from 10 μm to 400 μm with a step size of 10 μm and finalized with 500 μm. After the fabrication, adhesion is checked between two adjacent piezoresistive line pairs and adhesion is detected the fabricated piezoresistive line pairs up to 180 um. For this reason, the distance 190 μm gap is taken as the minimum gap distance.

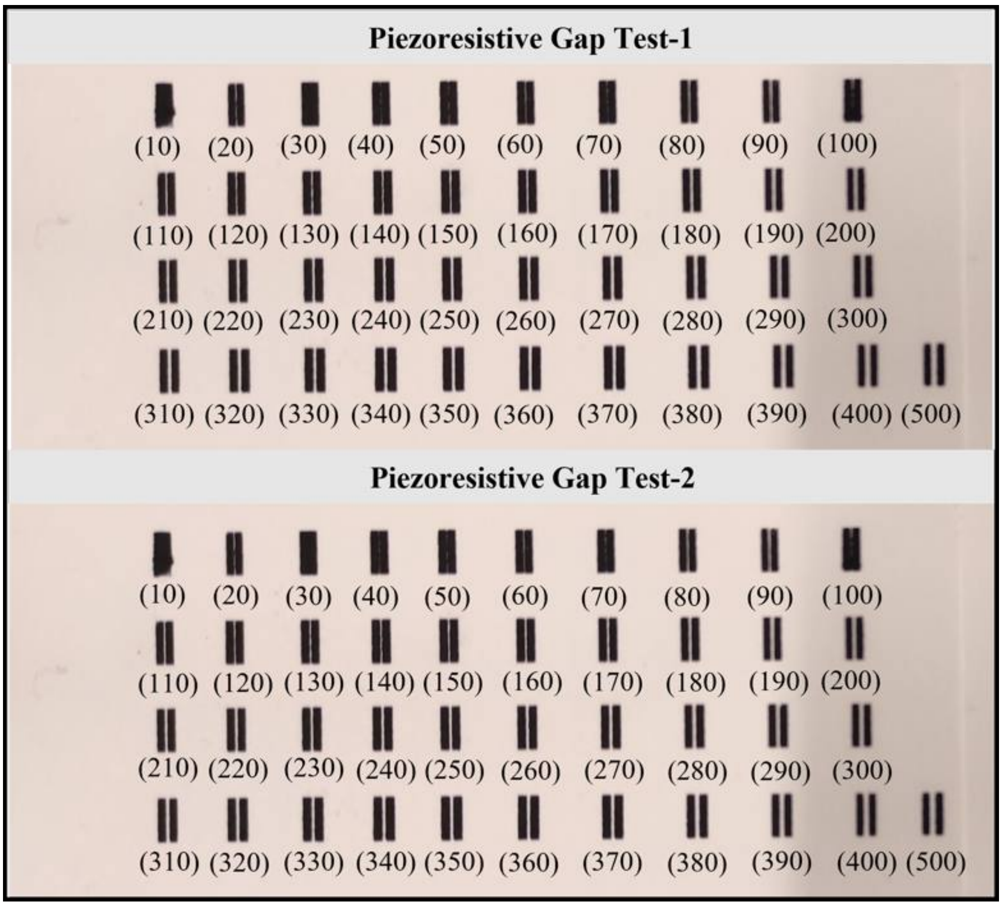

Figure 3.8: Photo of fabricated piezoresistive lines with changing gaps, all measurements are in micrometers.

Figure 3.9 shows the microscope views of fabricated lines with various sizes starting and which go up to from 10 μm - 500 μm. The values in the Figure 3.10 were found by taking the average of the values obtained by measuring over each gap between the piezoresistive line pair at different locations under the microscope.

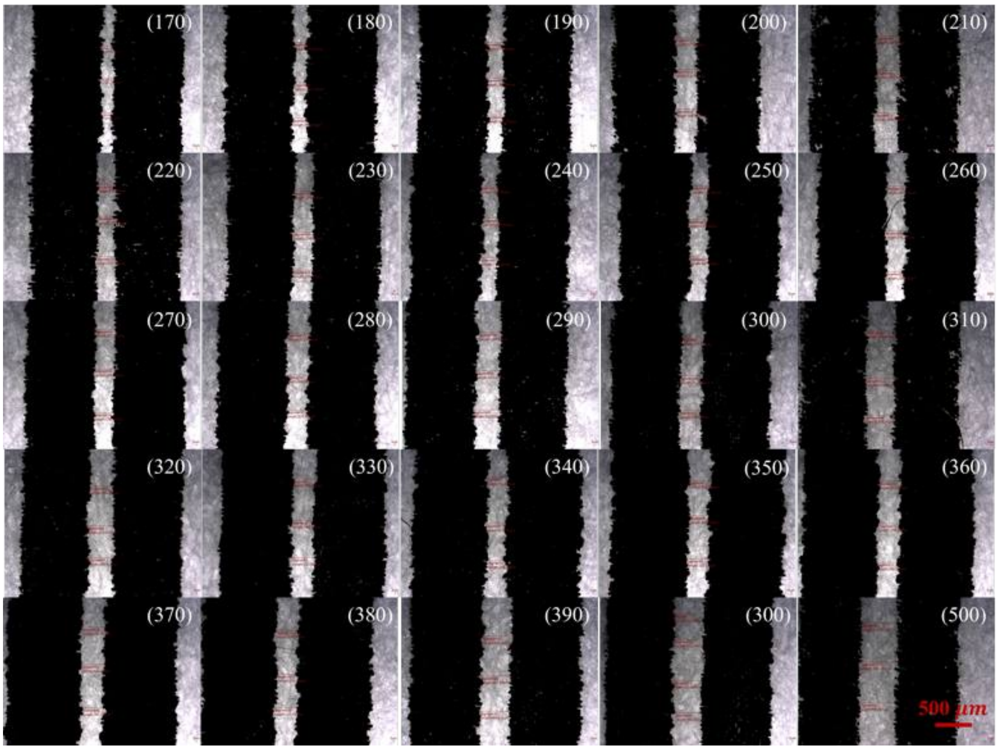

Figure 3.9: Close up view of the piezoresistive lines fabricated with various gaps. The design values of the gap of the lines are located in the upper right corner of each of them.

According to the experimental results of the gap test that is shown in Figure 3.10, gap distance (w_{gap}) designed as 240 μm and fabricated as 259 μm is determined because of its lower-error rate. However, it has approximately 7.87% accuracy rate and 29.3% precision rate. Because of this, it is not acceptable value in order to be able to fabricated 270 μm gap distance (w_{gap}). For this reason, the gap (w_{gap}) is chosen according to the piezoresistive layer designed as the M1 model, hence, it has approximately 1200 μm .

Another factor affecting the resistance change and sensitivity is the thickness of the piezoresistive line as shown in Equation 3.1. Figure 3.11 shows the normalized

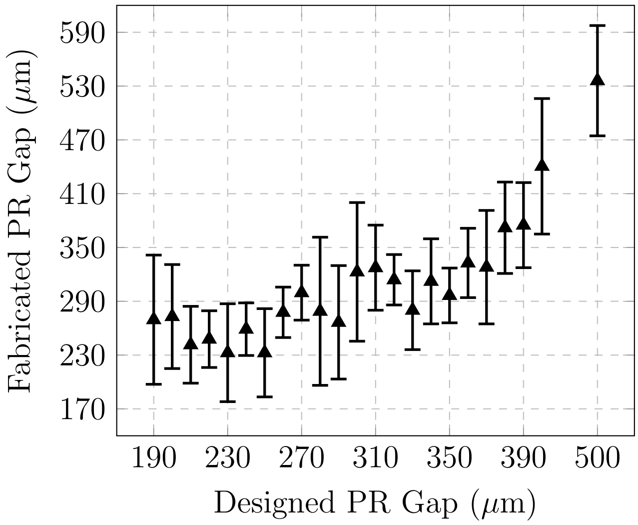

Figure 3.10: Plot of the designed versus fabricated gap distance (w_{gap}) between the adjacent piezoresistive line pairs. The first value where the materials do not diffuse to each other is the eighth data.

resistance change values according to various bending ratios of the piezoresistive line fabricated as a single or double layer on the Strathmore® 400 series Bristol paper. According to the data obtained from the experiments, the normalized resistance change ($\Delta R/R$) decreases from 0.2291 to 0.0586 Ω/Ω with an average error margins of 0.0239 Ω/Ω, and 0.4857 to 0.086 Ω/Ω with an average error margins of 0.0515 Ω/Ω for Single layer, and double layer, respectively, as shown in Figure 3.11. The equations and R-squared values of the fitting lines are determined in the Figure 3.11 as $2.1735x^{-0.967}$ and 0.9381 for the single layer, and $3.3653x^{-0.902}$ and 0.8948 for the double layer. Therefore, the single-layer thickness fabricated as a thin film is selected because of its more linearity and lower error.

3.3. Hole Ablation

Effective Young's Modulus (E_{eff}), and surface stress play an important role to develop and achieving a more sensitive, flexible, and robust force encoding structure [56,57]. Therefore, structure does not suffer from a plastic deformation under exerting force and stress density increases. In order to increase the effective Young's Modulus (E_{eff}) and surface stress of the linear absolute force encoder structure [58–60], some

Table 3.3: Designed and fabricated values of the gap (w_{gap}) between adjacent piezoresistive line pairs with their accuracy and precision rates.

Designed (μm)	**Measured (μm)**	**Accuracy Rate (%)**	**Precision Rate (%)**	**Designed (μm)**	**Measured (μm)**	**Accuracy Rate (%)**	**Precision Rate (%)**
190	269.5	41.84	72.06	310	327.5	5.64	47.45
200	273	36.5	58	320	314	1.87	28.12
210	241.5	15	42.85	330	280	15.15	43.94
220	247.8	12.63	31.64	340	312.2	8.17	47.45
230	232.7	1.17	54.6	350	296.5	15.28	30.55
240	258.9	7.87	29.3	360	332.7	7.58	38.67
250	232.6	6.96	49.2	370	328	11.35	63.27
260	277.7	6.8	28.12	380	372	2.1	50.97
270	299.6	10.96	30.64	390	375	3.85	47.45
280	278.8	0.43	82.6	400	440.5	10.13	75.58
290	266.5	8.1	63.27	500	536	7.2	61.5
300	322.8	7.6	77.33	-	-	-	-

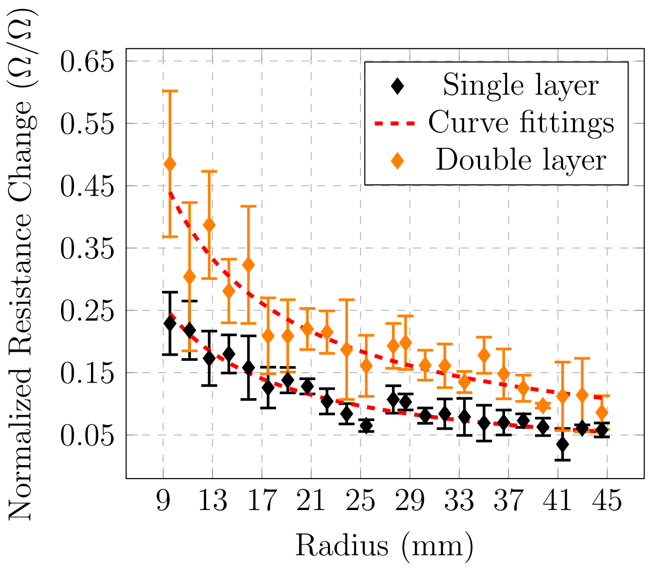

Figure 3.11: The behaviour of Bristol paper for various layers. The fitting line equations for the single layer, and double layer are $2.1735x^{-0.967}$, and $3.3653x^{-0.902}$, respectively.

aspects can be listed as follows: (1) the ablated holes diameter (w_o), and (2) the pattern of the ablated holes located in each segment.

As mentioned in section 3.2, piezoresistive line width (w_l), the gap (w_{gap}) between two adjacent piezoresistive line pair, and the S-shaped values of piezoresistive layer, that is placed in each row of one segment area, is selected 980 μm, 1200 μm, and single

S-shape, respectively, according to the fabrication results.

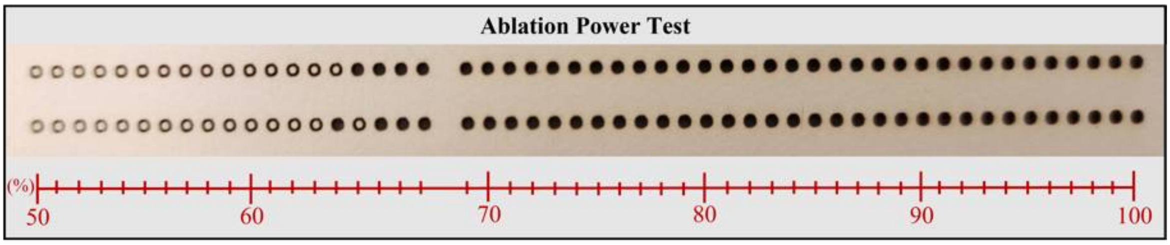

Figure 3.12: The fabricated view of the holes having 1 mm diameter that are cut by increasing the power level by 1% from 50% to 100% while keeping the speed and frequency constant.

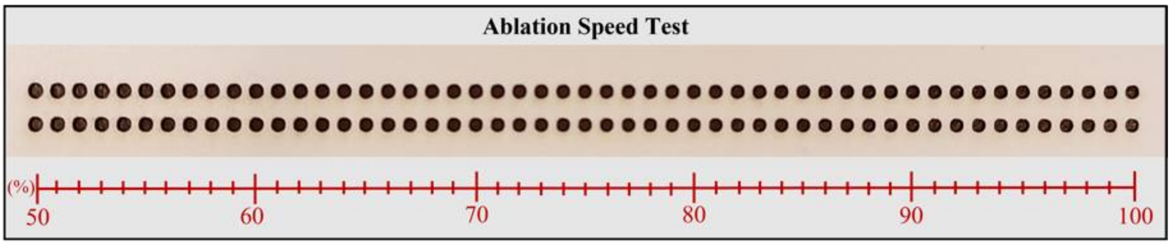

Figure 3.13: Fabricated view of holes having 1 mm diameter that are cut by increasing speed by 1% from 50% to 100% with determined 67% power level.

Firstly, as indicated in Figures 3.12 and 3.13, the laser cutter was optimized beforehand for the most precise hole ablation fabrication. This optimization determines optimal power, and speed level of the laser cutter so that the ablated hole can be fabricated as close to the designed one. For these experiments, initially, the minimum power level at which the substrate material, Strathmore Bristol paper, can be perforated is tested. As shown in Figure 3.12, while keeping the speed and frequency constant, 1 mm holes are cut by increasing the power level from 50% to 100% with a 1% step size. As a result, a minimum perforation level was achieved using 67% power.

In Figure 3.13, the determined power level (67%) and frequency of the laser cutter is kept constant, and the holes designed as 1 mm are cut by increasing the speed by 1% from 50% to 100%. In this experiment, the coherency between the designed and fabricated holes is observed. According to the test results presented in Figure 3.14, the highest amount of coherency between the designed and fabricated holes with a diameter of 1 mm is detected at 100% speed level with the least expansion ratio stemming from peripheral combustion.

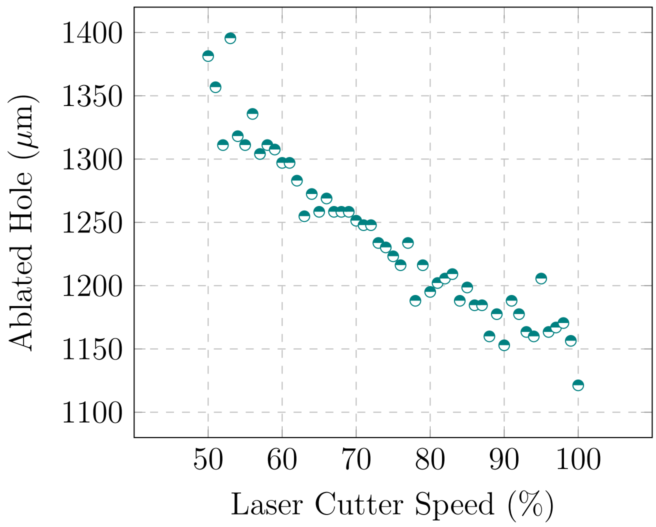

Figure 3.14: Plot of the fabricated holes values which are designed as 1000 μm, according to the various laser speed level testing to determine the most appropriate laser speed level.

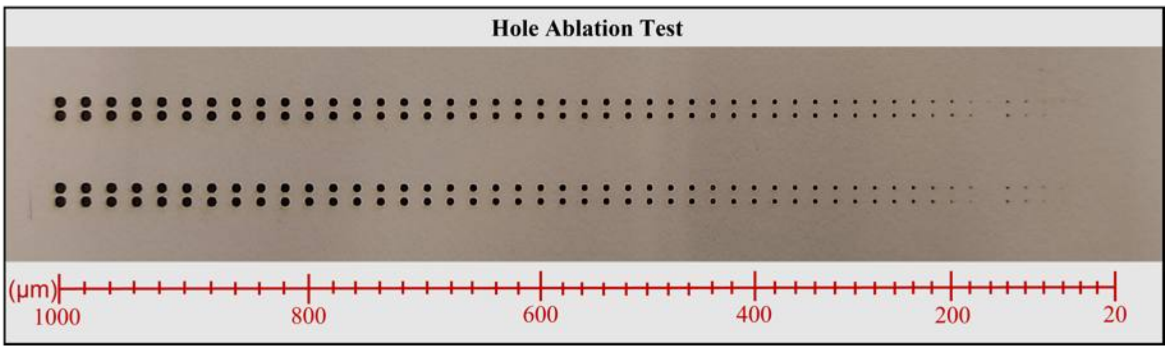

Figure 3.15: Fabrication view of various holes designed from 20 μm to 1000 μm with 20 μm resolution cut by laser's determined 67% power, 100% speed and 5000 Hz frequency.

In order to find the most suitable and precise hole ablation form, as shown in Figure 3.15, holes with various dimensions that change from 1000 μm to 20 μm with a 20 μm resolution, was designed and cut by means of a laser cutter with 67% power, 100% speed and 5000Hz frequency. The views under the microscope of the ablated holes are indicated in Figure 3.16. As can be seen in Figure 3.16, the hole dimensions that is under the 460 μm are not able to be perforated precisely with optimized laser cutting parameters. Therefore, 460 μm is taken as the minimum fabrication limit for the hole ablation. The results of the experiment carried out to compare the dimensions of the designed, and ablated holes under the 67% power, 100% speed and 5000 Hz frequency of the laser are plotted in Figure 3.17.

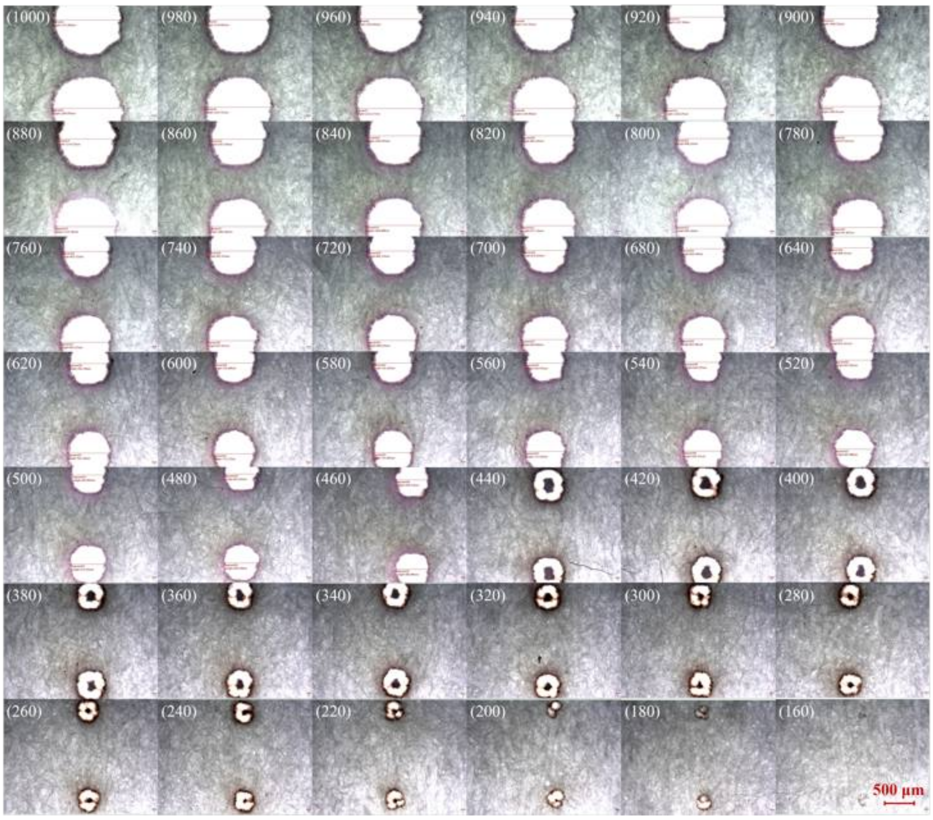

Figure 3.16: Close up view of ablated holes with various diameters. The design values of the holes are located in the upper left corner of each of them.

Based on the test results for hole sizes w_o indicated in Figure 3.17 and Table 3.4, the hole, which is designed as 500 μm and fabricated as approximately 590 μm, has most accuracy rate with 18.62%. Additionally, according to the finite-element-modeling (FEM) simulation results shown in Figure 3.18, hole diameter, which is designed as 500 μm and fabricated as approximately 590 μm, having 10.4 MPa maximum stress density σ_{max} and 342.74 μm minimum bending $\delta_{AA'}$ under 1N force loading is preferable due to its higher-stress value among the other patterns. For this reason, in order to reduce the graphite line diffusing and the peripheral combustion effect of the laser on the graphite, 500 μm hole design is selected in comparison with all the other ablated holes.

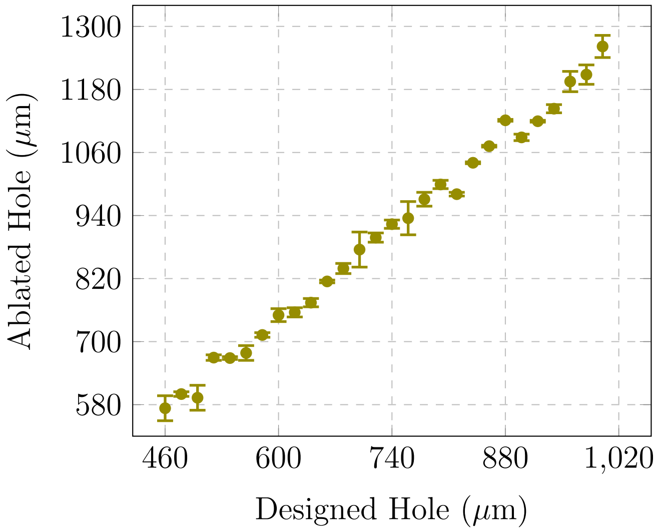

Figure 3.17: Plot of the test of the perforation of designed holes versus ablated holes that are cut under the optimized values of power, speed, and frequency of the laser, is emphasized.

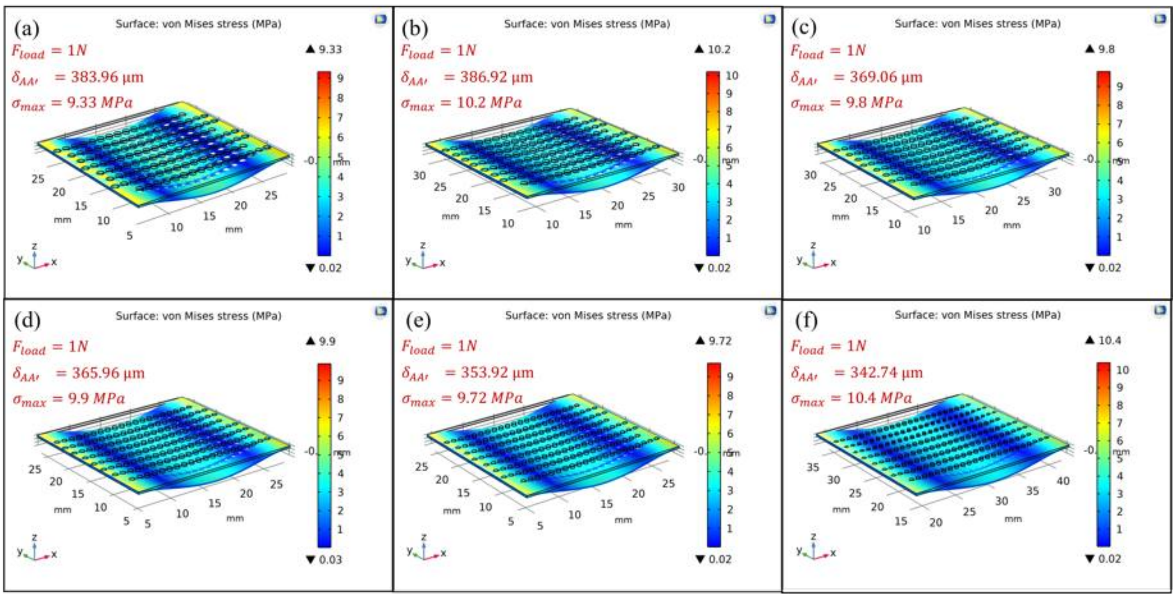

Figure 3.18: Simulation results of ablated holes with various hole diameters within a defined segment area ($L_{g3} \times w_p$): (a) designed as 820 μm and fabricated as 980 μm, (b) designed as 760 μm and fabricated as 935 μm, (c) designed as 680 μm and fabricated as 839 μm, (d) designed as 620 μm and fabricated as 755 μm, (e) designed as 560 μm and fabricated as 678 μm, and (f) designed as 500μm and fabricated as 593 μm.

However, the positioning of the designed holes on the sensor with a particular

Table 3.4: Designed and ablated values of the hole diameters (w_o) with their accuracy and precision rates.

Designed (μm)	**Measured (μm)**	**Accuracy Rate (%)**	**Precision Rate (%)**	**Designed (μm)**	**Measured (μm)**	**Accuracy Rate (%)**	**Precision Rate (%)**
1000	1261.8	26.18	21.08	720	898	24.72	8.79
980	1208.2	23.28	18.45	700	875.2	25.02	33.39
960	1195	24.48	19.33	680	839.17	23.4	9.67
940	1143.3	21.63	7.78	660	814.57	23.42	2.63
920	1119.5	21.68	1.76	640	774.15	20.96	7.91
900	1088.7	20.97	6.15	620	755.69	21.88	8.78
880	1121.24	27.41	1.75	600	750.42	25.07	12.3
860	1072	24.65	1.75	580	712.64	22.86	4.39
840	1040.4	23.85	1.76	560	678.37	21.13	14.06
820	980.65	19.59	3.51	540	668.7	23.83	2.63
800	1000	24.88	7.91	520	669.58	28.76	5.27
780	971	24.48	13.18	500	593.13	18.62	23.7
760	934.95	23.02	31.63	480	600.16	25.03	4.39
740	923.5	24.8	7.91	460	573.19	24.608	23.78

pattern is directly effective in maximizing σ_{max} under the minimum bending after the force is applied to the segment. For this reason, the gap test shown in Figure 3.20 was carried out to find out how many predetermined 593 μm holes can be placed between the piezoresistive lines in each segment. According to the test results, the minimum producible distance between ablated holes is determined as 380 μm. Based on this minimum value, various patterns were designed to observe the stress behaviour of the sensor and simulated as shown in Figure 3.20. These designed hole patterns can be listed as follows: (a) no ablation, (b) ablation with 8×12 patterns with 1500 μm gap between each hole, (c) ablation with 8×15 patterns with 1000 μm gap between each hole, (d) ablation with 8×23 patterns with 500 μm gap between each hole, (e) ablation with 8×26 patterns with minimum producible gap of 380 μm between each hole, and (f) ablation along the x-axis in dimensions 21.941×0.593 mm^2 between the piezoresistive lines as an 8×1 pattern with no gaps between the holes.

According to the finite-element-modeling (FEM) simulation results shown in Figure 3.20, hole pattern produced with a gap of 1000 μm having 10.3 MPa maximum stress density σ_{max} and 0.3281 mm minimum bending $\delta_{AA'}$ under 1N force loading is preferable due to its higher-stress value among the other patterns.

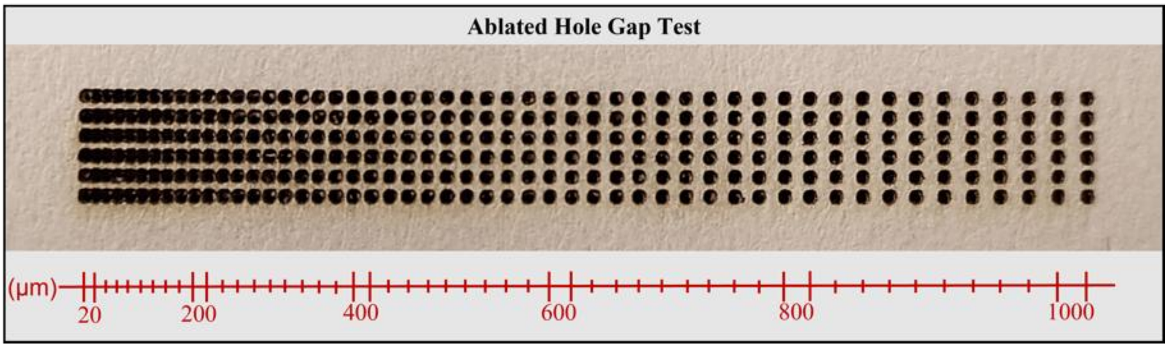

Figure 3.19: The fabrication view of the gap values that is between the determined 0.5 μm diameter designed holes changing from 20 μm to 1000 μm with 20 μm resolution, cut by laser's determined 67% power, 100% speed and 5000 Hz frequency.

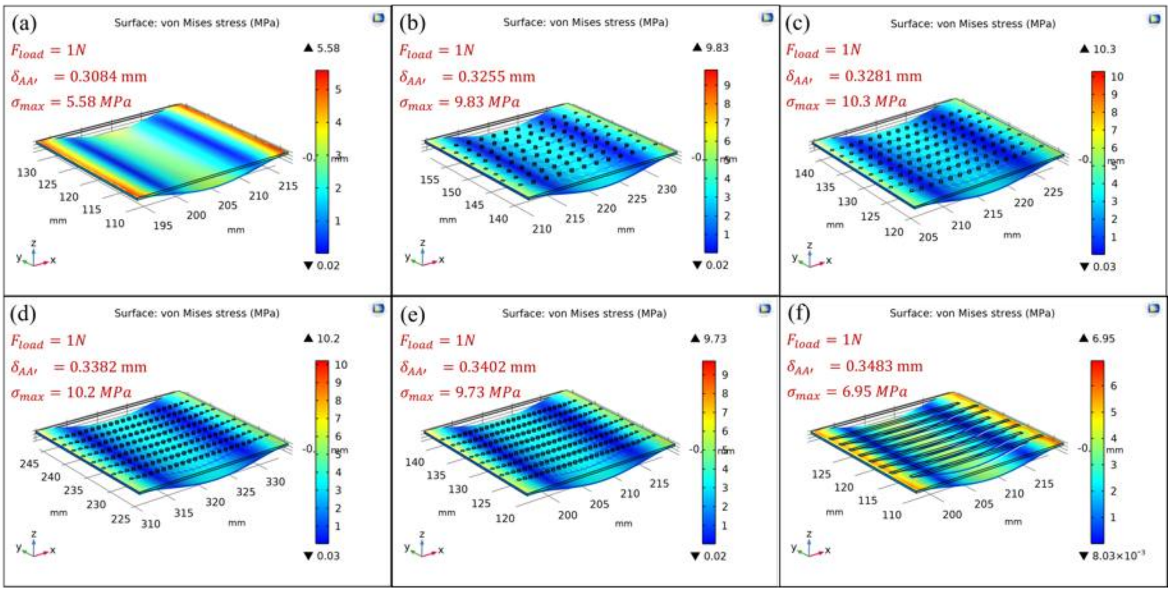

Figure 3.20: Simulation results of ablated holes at various pattern within a defined segment area ($L_{g3} \times w_p$): (a) non-ablated, (b) ablated with 1500 μm gap, (c) ablated with 1000 μm gap, (d) ablated with 500 μm gap, (e) ablated with the minimum producible gap of 380 μm, and (f) all-ablated holes.

3.4. Proposed Force Encoder Structure

The parameter of the paper-based sensing structure, which directly affects the overall performance of the system, is tabulated in Table 3.5. The illustrated force

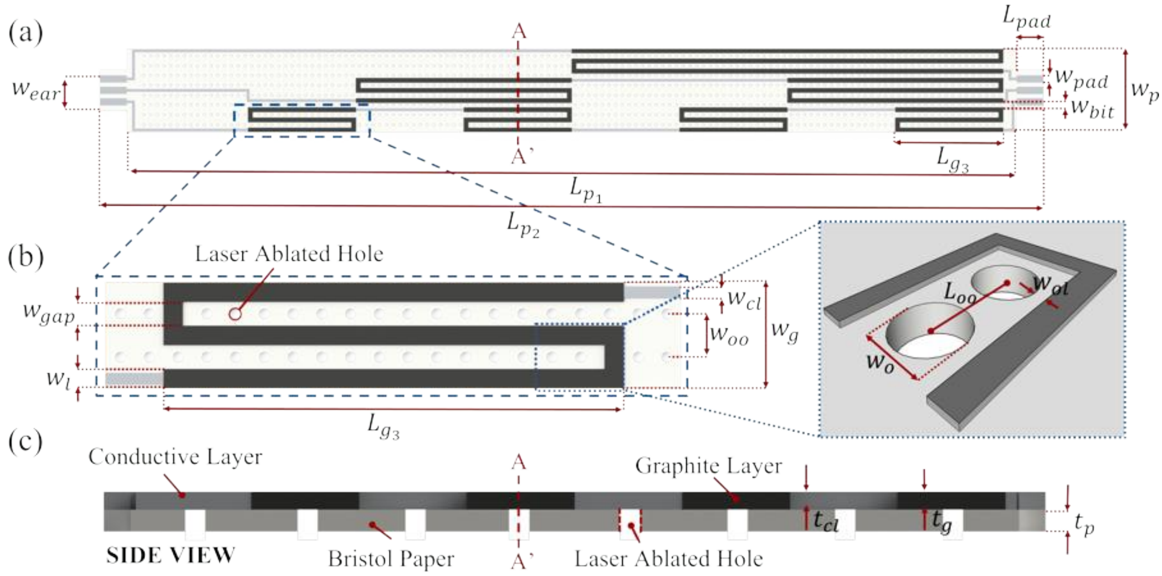

Figure 3.21: Technical drawing of the proposed 3-bit paper-based linear absolute force encoder structure and its design parameters. (a) The top view of the paper-based sensing structure that harbors eight segments. (b) a close-up view of the piezoresistive lines and ablated holes. (c) a side view of the sensing structure.

encoding structure harbours eight different segments for ease of application. Piezoresistive graphite layers are carefully coated on these segments as shown in Figure 3.21a. On the other hand, Figure 3.21b and 3.21c indicate details of top and side views of the serpentine-shaped graphite layers, respectively. In Figure 3.21, L_{p_2} and w_p indicate the length and the width of the proposed structure, respectively. w_{ear} illustrates the width of the connector housing, whereas w_{pad} defines the width of one conductive pad. Additionally, L_{g_3} depicts the length of just one segment, whereas L_{p_1} expresses the total length of the segments. Finally, L_{pad} defines the length of the conductive pad. The length of the sensor frame (L_{p_2}) has been chosen as 210 mm (long edge of a generic A4 sheet) in order to make it comparable with the length of the robotic system. Other dimensions that are displayed and then tabulated in Table 3.5 are carefully selected and scaled according to this initial choice of L_{p_2}.

Figure 3.21b illustrates just one segment of the proposed sensor in detail. The parameters, w_g, indicate the width of the piezoresistive graphite layer. Moreover, w_{gap} expresses the gap between two graphite lines, whereas w_l states the width of just one line of this graphite layer. The structure has been perforated by ablating holes having diameters of w_o in order to increase its performance, as illustrated on the right-hand side of Figure 3.21b. Ablated holes are separated from each other with a distance of w_{oo} and are positioned to w_{ol} mm away from the graphite line. The parameters stated in Figure 3.21b are chosen concerning the fabrication limits, which will be thoroughly explained in Chapter 4. Thus, w_o of perforated holes are confined by the resolution of the laser-cutting system (Epilog® Mini 18, 30 W) used to complete the ablation process. Moreover, the resolution of stencil masks limits the minimum width of the graphite line (w_l) and the gap (w_{gap}) in between them.

In Figure 3.21c, the parameters are selected regarding the precision of the silk screen-printing. The thickness of the off-the-shelf paper-substrate (t_p) is equal to 289 μm. Moreover, the thickness values t_{cl} of the conductive layer and t_g of the graphite coating are both approximately 50 μm because of the 50 μm thick silk stencils used to form these layers. Piezoresistive layers with serpentine shapes are preferred in order to increase the sensitivity and the amount of total normalized resistance change [61, 62]. Hence, a similar serpentine design, as shown in Figure 3.21 is preferred over a complete full-area coating on the segments in order to be able to detect the slightest resistance changes occurring in the system.

In order to increase the precision of the detection process, a silicone sandwich structure is shown in Figure 3.22, is employed, which decreases the force exerting area hence increases the pressure acting on the paper-based structure. This low-cost sandwich structure also acts like an artificial skin that protects the proposed force encoder system [51]. In Table 3.5, values defining the geometry of the silicone sandwich structure are tabulated. It should be noted that these values are in line with the geometry of those as mentioned above paper-based 3-bit linear absolute force encoding structure. Additionally, two connector housings are placed at the edges of this silicone structure, as shown in Figure 3.22d.

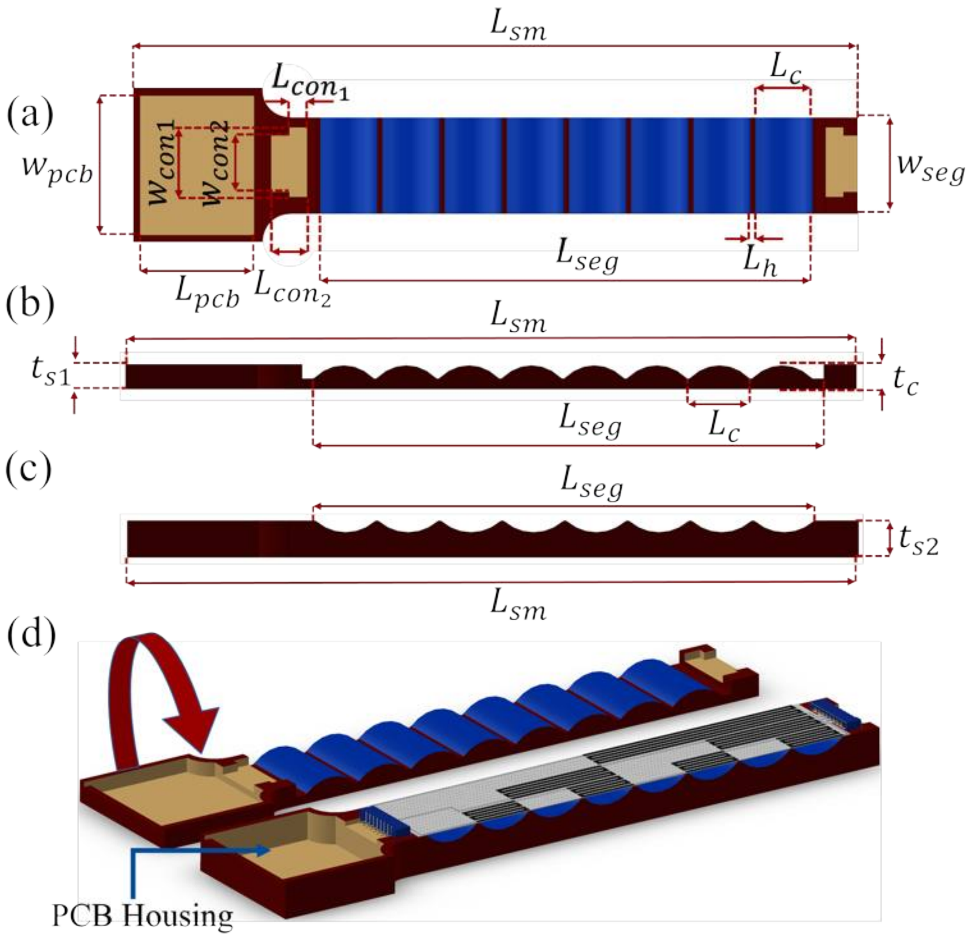

Figure 3.22: Technical modelling of the proposed silicone molding body along with the paper-based piezoresistive force encoder sensor and its design parameters. (a) top view of the upper part of the silicone mold structure. (b) side view of the upper part of the silicone mold structure. (c) side view of the base part of the silicone mold structure. (d) 3D view of the structure. This silicone mold structure protects the sensing structure and electronics circuits and reduces the force exerting active area, and, in turn, increases the stress acting a piezoresistive layer.

Table 3.5: Parameters and related values of the proposed system indicated in Figures 3.3, 3.21, and 3.22.

Prms.	**Descriptions**	**Designed (mm)**	**Measured (mm)**	**Error (%)**
w_p	Width of the force encoder	18.5625	18.576	0.07
w_{pad}	Width of the contact pad	1.6	1.5614	2.52
L_{pad}	Length of the contact pad	6.0	5.834	2.77
L_{g_3}	Length of the graphite layer on one segment	24	23.613	1.62
L_{p_1}	Length of eight segment	198	198.55	0.27
L_{p_2}	Length of the force encoder	210	208.86	0.55
w_{ear}	Width of the ear	9.125	8.845	3.07
w_g	Width of the graphite layer	5.5	5.58	1.45
w_{bit}	distance between each graphite layer bit	1.0	0.918	9.2
w_{oo}	Vertical distance between two ablated holes	2.25	2.1675	3.67
w_{cl}	Width of the silver line	0.6	0.68	13.3
w_o	Diameter of the ablated hole	0.5	0.593	18.6
L_{oo}	Horizontal distance between two ablated holes	1.5	1.462	2.54
w_{gap}	Distance between two graphite lines	1.2	1.088	9.44
w_l	Width of the graphite line	1.0	0.98	2
t_{cl}	Thickness of the silver layer	0.05	0.05	-
t_g	Thickness of the graphite layer	0.05	0.05	-
t_p	Thickness of the paper substrate	0.289	0.289	-
w_{ol}	Distance between the hole and graphite line	0.375	0.187	51.14
w_{seg}	Width of the silicon region for eight segment	37	36.89	0.3
L_{con1}	Length of the connector port	6.6	6.82	3.33
L_{seg}	Length of the silicon region for eight segment	192	193	0.52
w_{con1}	Width the connector	25.8	26.93	4.37
L_c	Length of the silicone mold bulge	24	23.82	0.75
L_{con2}	Length of the connector	14	13.64	2.58
L_h	Distance between the silicone mold bulges	1.86	1.63	12.37
w_{con2}	Width the connector port	22	21.57	1.96
L_{sm}	Length of the silicon mold	280	280	0
t_c	Thickness of the upper part of mold bulge	7.8	8.21	5.25
w_{pcb}	Width of the PCB housing	54	53.66	0.63
t_{s1}	Thickness of the upper part of the silicon mold	8.2	8.21	0.12
L_{pcb}	Length of the PCB housing	44	44.12	0.27
t_{s2}	Thickness of the base part of the silicon mold	14	13.7	2.15

4. IMPLEMENTATION

This chapter elaborates on the implementation of the paper-based piezoresistive force encoding sensor. Section 4.1 presents details about the preferred material for the fabrication process of low-cost force encoding sensor and the contents of the supporting materials. Section 4.2 explains the method used in fabrication in order to be able to obtain a robust force encoding sensor. Finally, Section 4.3 shows and explains the proposed fabrication process and final form of the fabricated force encoding sensor.

4.1. Materials

There are three main materials required to fabricate the force encoding sensor structure proposed in this thesis. These can be listed as follows: (1) a substrate material that forms the basis of the sensor structure, (2) a piezoresistive material for sensing, and (3) a conductive material to be used for electrical connection between the sensor and the read-out circuit. Main are constraints selection of these materials are: cost effectiveness, fabrication ease, flexibility, high-conductivity, and integration with each other. For these reason, various materials have been examined and presented considering the above mentioned criteria.

The materials tested and compared are listed in Table 4.1 and Table 4.2. Firstly, cellulose-based materials are investigated as the main substrate material due to their flexibility, low-cost, ease and quick fabrication form. The primary advantages of paper materials are: (1) easy being to produce and then (2) suitability for coating processes of pasty materials due to their fibrous structure [63]. Strathmore® Bristol, Alex Schoeller®, and Photography papers are chosen and analyzed as a substrate material in regard with above mentioned points. These substrate materials are suitable for silk screen printing, and laser cutting since they do not require any clean room treatment and have easily detachable textures. Unlike the other compared substrates in Chapter 3, Strathmore® Bristol paper is more preferable because of their robust texture and, therefore, their long-term durability against high force magnitudes, stability under the various bending, and lower-absorbency features.

Secondly, sensing materials are examined. It is widely preferred as a sensing material for force, pressure, and tactile sensing. It is a soft, black opaque, easily adhered to texture, water-soluble material hence it is suitable for easy and quick fabrication, and flexible material. Because of these features, graphite is preferred. Moreover, graphite does not require any cleanroom process. Gwent® C2030519P4 carbon paste and Bare Conductive® Electric paint are preferred and compared as shown in Table 4.1 to use as sensing material in the proposed system. The materials compared are discussed from two perspectives: (1) ease of production according to clean-up solvent and drying time, and (2) the amount of resistivity for a thin film. Thus, as a piezoresistive layer, Bare Conductive® Electric paint is chosen because of its good adhesion, non-toxic, low-cost, water-soluble, and shorter cleaning process presented in Table 4.1.

Finally, materials such as gold, silver and platinum paste have been compared as shown in Table 4.2 we tried to minimize the electrical loss and eliminate noise as much as possible in connection. Therefore, compared with other materials, Baku® Bk-426 is chosen to print onto paper using a silk stencil because of its low-cost, not require any clean-room process, easy and quick to fabrication with low drying time, and sufficiently high conductivity.

Table 4.1: Comparison of the features of the selected elastic dielectric materials.

Elastic Dielectric Materials	**Sheet Resistivity**	**Clean-up Solvent**	**Drying Temperature in 15 minutes**
Gwent® C2030519P4 Carbon paste	75 $\Omega/\square$ @ 25 μm thick film	Ethoxy propanol	80° C
Bare Conductive® Electric paint	55 $\Omega/\square$ @ 50 μm thick film	Water	Room temperature

Table 4.2: Comparison of the features of the selected conductive materials.

Conductive Material	**Sheet Resistivity**	**Clean-up Solvent**	**Drying Time**	**Storage Temperature**
Gwent® C2130809D5 Ag paste	100 m$\Omega/\square$	Ethoxy propanol	10 min @ 80° C	Room temp.
Gwent® C2050804P9 Pt paste	590 m$\Omega/\square$	Ethoxy propanol	30 min @ 80° C	Room temp.
Gwent® C2041206P2 Au paste	80 m$\Omega/\square$	Ethoxy propanol	30 min @ 80° C	15° C
Circuit Scribe® Beta Ag paste	25 m$\Omega/\square$	Ethoxy propanol	30 min @ 140° C	Room temp.
Baku® BK-426 Ag paste	0.1 $\Omega/\square$	Thinner	60 min @ Room temp.	Room temp.

4.2. Methods

In the literature, there are various fabrication methods for coating the sensing as mentioned above and conductive material onto a paper substrate in desired dimensions. They can be listed as follows: (1) silk screen-printing [64–66], (2) ink-jet printing [67,68], (3) the printing with a hand-crafted stencil [69–71], and (4) directly drawn on paper [72, 73]. The points to consider while choosing the fabrication method are not to damage the paper substrate, sensing and conductive material, to be low-cost, easy and quick to fabricate, and production precision. When all fabrication methods are examined in terms of the specified criteria, the silk-screen printing method is preferred as the main fabrication method in this study because it provides high-sensitivity coating and desired properties. The production steps of silk screen printing are visualized in detail in Appendix A [74].

4.3. Proposed Fabrication Process

Figure 4.1 shows steps of the fabrication process of the paper-based force encoder structure. As mentioned above, in this thesis, due to its low-cost and robustness, the main fabrication material is chosen as a 289 μm thick off-the-shelf Strathmore® 400 series Bristol paper. Furthermore, as the main fabrication method, silk screen-printing techniques are used to form both the graphite and conductive layers on the paper substrate.

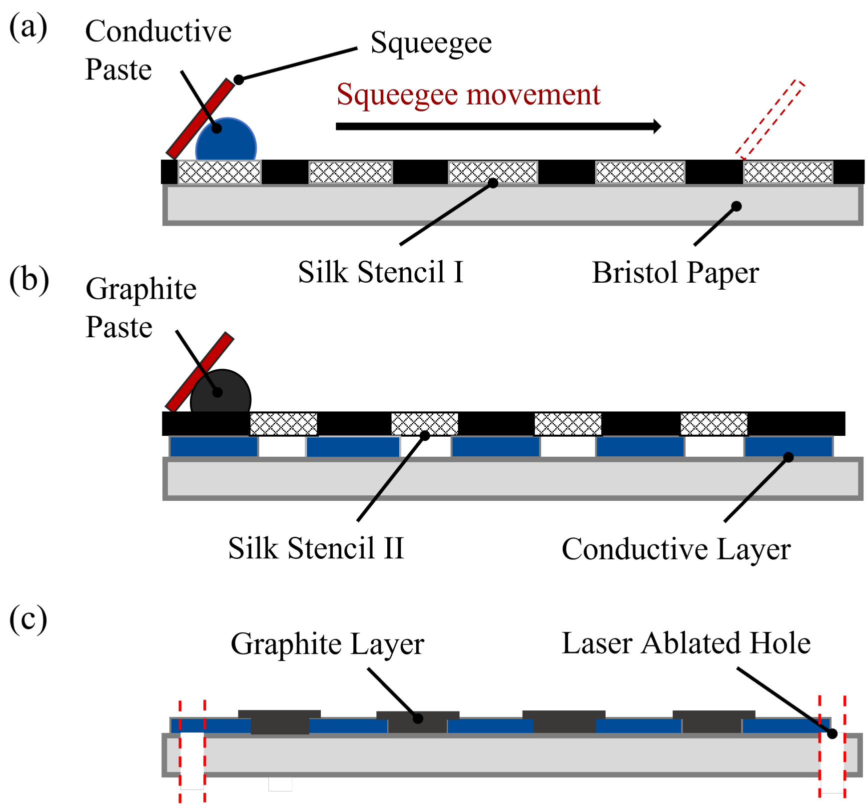

Figure 4.1: Illustration of the fabrication process of the linear absolute encoder force sensor. (a) Ag paste coated onto the Strathmore® 400 series Bristol paper as a base material with stencil mask (mask I) using silk screen printing method. (b) graphite paste coated onto the Ag coated Strathmore® 400 series Bristol paper with stencil mask (mask II) using silk screen printing method. (c) laser ablation (Epilog Mini 18, 30W).

As a first step, a 48 μm thick silk stencil mask (mask I) having a pore size of 36 μm that is shown in Figure 4.2, is used to apply a high-conductive and low resistant silver paste (Baku® Bk-426) onto the paper substrate that is indicated in Figure 4.1a with the aim of forming conductive lines between the graphite pads and peripheral electronics read-out circuitry. The conductive paste is applied onto mask I with the help of a squeegee blade as depicted in Figure 4.1a. The silver-coated layer is rested for 60 minutes to have an optimal conduction level by drying at room temperature. Following that, an electrically high-resistant graphite paste (Bare Conductive® Electric paint) having 48 μm thickness is chosen and coated using the second stencil mask onto the Ag coated paper base as depicted in Figure 4.1b.

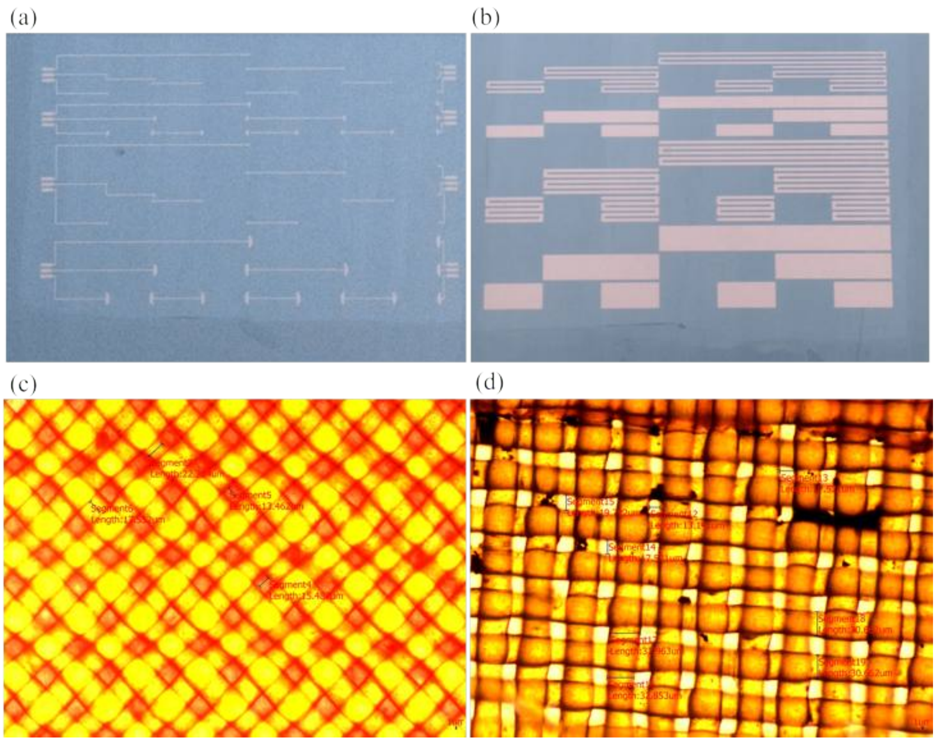

Figure 4.2: (a) view of the silk stencil (mask I) to coat Ag paste onto the Strathmore Bristol paper, (b) view of the silk stencil (mask II) to coat graphite paste. (c) close up view of emulsified, and (d) open pores of the mask.

Here it is carried out as a result of manual aligning by means of the semi-circle shaped tips of the silver layers that are used as alignment marks onto the silk stencil as depicted in Figure 4.2. The fabrication of the sensing structure continues with folding and cutting the long edge of an A4 size Strathmore® 400 series Bristol paper three times. Thus, an encoder structure having dimensions of 210 $mm \times 18.5625$ mm is obtained.

The force encoder is proposed, which its form has covered and perforated in Chapter 3. Subsequently, multiple holes are created on the structure through a laser ablation process to reduce the effective Young's Modulus and acquire more considerable bending. Hence, sensitivity under the exertion of collision force is increased. The ablation process that is depicted in Figure 4.1c is operated utilizing a laser-cutting device (Epilog® Mini 18, 30W) by arranging the specifications that are speed, power, and frequency as 100%, 67%, and 5000 Hertz, respectively.

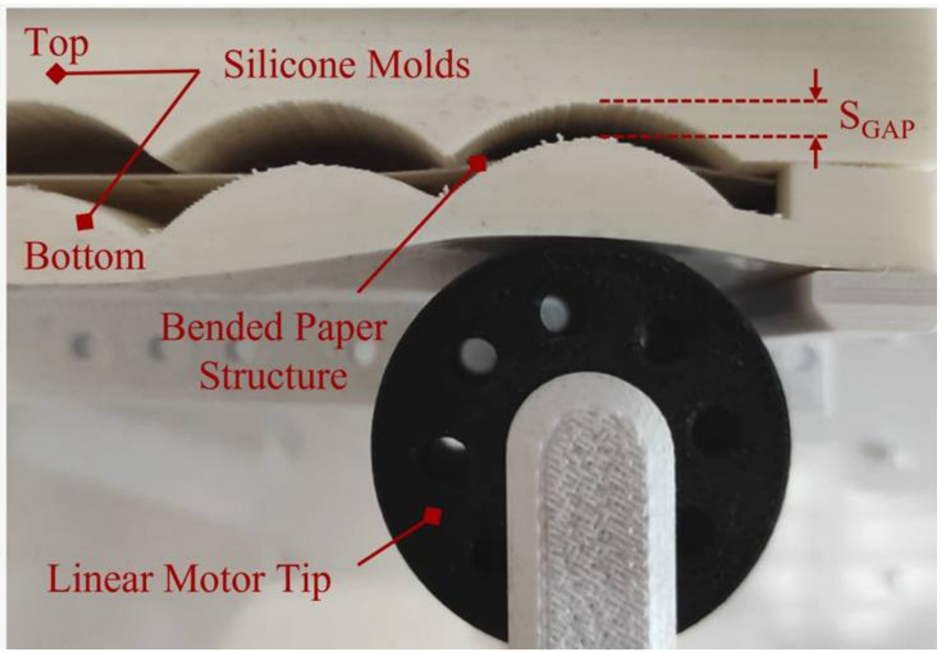

Figure 4.3: Side view of the paper-based structure sandwiched in between two silicone molds. The sensing system is getting poked with the linear motor tip. The gap between the upper and lower parts of the silicone mold S_{GAP} completely closes when a force of 12N or higher is exerted.

Finally, the silicone molds are utilized to augment the sensitivity of the overall sensing system, as illustrated in Figure 4.3. The underlying reason for employing the silicone mold is to benefit from the linear region of the resistance in case of bending. The silicone mold also acts as a protective layer, resembling an artificial skin-like structure. A depiction of the fabricated paper-based linear absolute force encoder is given in

Figure 4.4a, a close-up view of the Ag and graphite coated perforated structure that consists of piezoresistive and conductive layer shown in Figure 4.4b along with scale bar, and the microscope view of the structure of the paper material, which is the main material of the sensor. The graphite coated state is shown in Figures 4.4c and d.

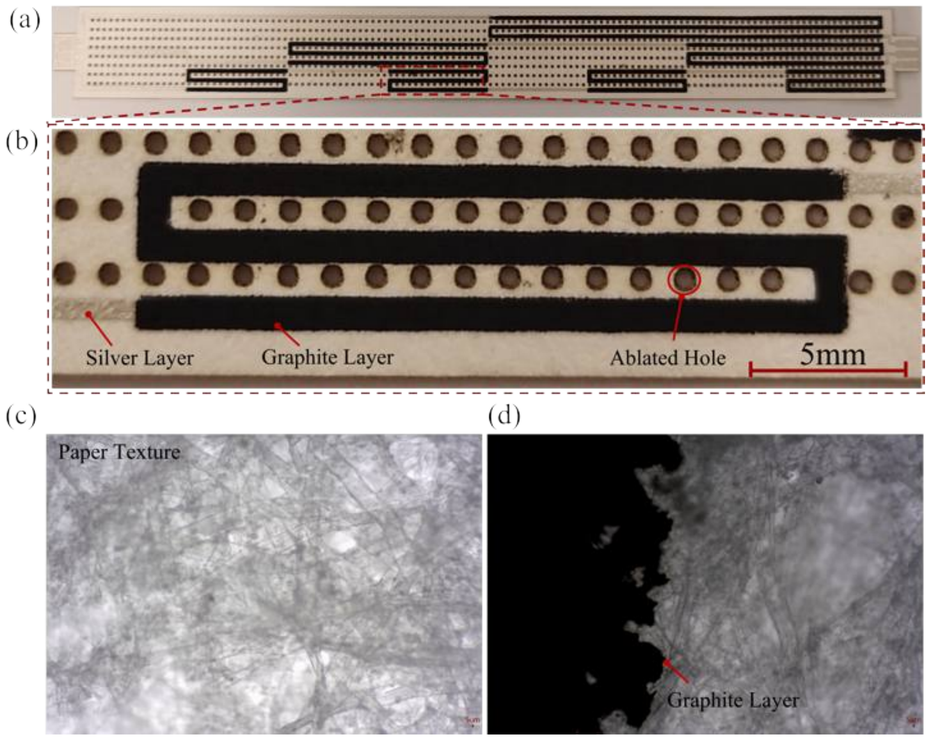

Figure 4.4: (a) The fabricated view of a paper-based piezoresistive linear absolute force encoder, (b) a close-up view of Ag and graphite layers along with its perforated structure, (c) microscope view of the fibrous structure of the Strathmore® 400 series Bristol paper with a 20X magnification ratio, and (d) microscope view of the graphite printing onto the paper substrate with a 20X magnification.

The force encoder is connected to the peripheral electronic read-out circuit via dual-edge card connectors at the end of the fabrication process. The connectors ensure the electrical connectivity between the biosensor and read-out circuit by contacting the silver pads to the connectors' insertion pins.

5. ELECTRONICS

This chapter presents the electronic read-out system and components that exist within its structure of it. Section 5.1 elaborates our proposed read-out circuitry for converting resistance changes resulting from the application of force in the piezoresistive layer into an electrical voltage signal.

5.1. Proposed Read-Out Circuitry

As mentioned in the literature, many complex circuits have been presented in flexible piezoresistive sensors. However, there are not many types of read-out systems recommended for use in disposable sensors that is paper as the substrate material. The proposed circuits are uncomplicated read-out circuits created only to detect the change that occurs due to the working principle of the material and the sensor. Since the working principle of these circuits is on balance, they work both with high performance and high sensitivity. For this reason, it constitutes an adaptation to work on paper-based sensors. The two most common read-out systems work on the balance principle. These are the voltage divider and Wheatstone bridge circuits as illustrated in Figure 5.1. However, the Wheatstone bridge circuit is chosen as the read-out circuit because it can be integrated with an instrumental amplifier for higher gain and the sensing material can be better calibrated.

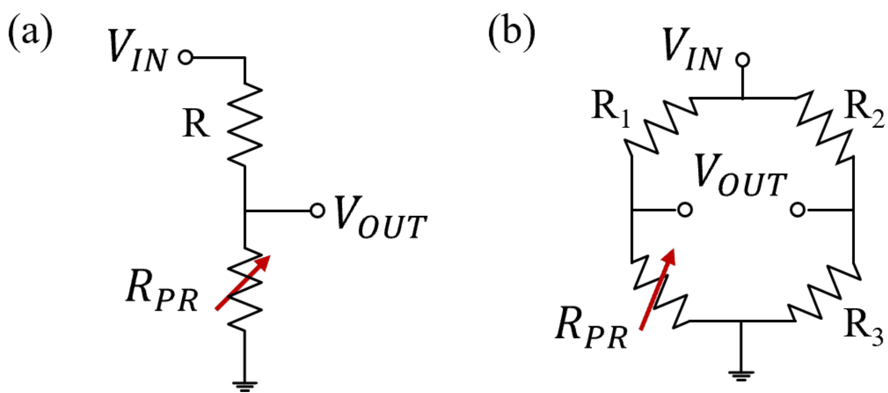

Figure 5.1: Schematics of conventional read-out circuits. (a) Voltage divider circuit, (b) Wheatstone bridge circuit.

It is above mentioned that the proposed sensing mechanism is composed of a 3-bit linear absolute encoder structure. As a result of this means that the proposed read-out circuitry has a collaboration of identical three Wheatstone bridge circuits and instrumentation amplifiers to follow each bit. In order to be able to detect the resistance change ΔR, occurring due to the linear motor's force loading F_{load}, a Wheatstone bridge circuit and an instrumentation amplifier are used.

$$V_{OUT} = V_{IN}\left(\frac{R_{PR}}{R_{PR} + R_{REF}} - \frac{R}{R + R}\right)G \tag{5.1}$$

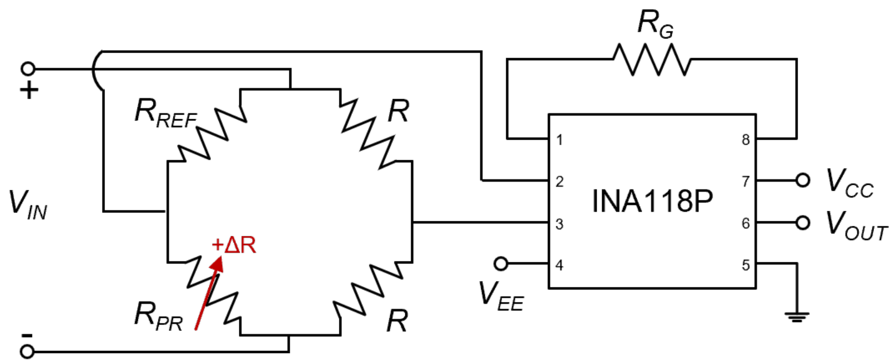

Figure 5.2: The block diagram of the proposed electronic read-out circuitry that composed of a Wheatstone bridge circuit with one positively changing piezoresistor and a subsequent instrumental amplifier, INA118P, to amplify the voltage signal acquired through the resistance change.

In order to be able to detect the resistance change ΔR occurring due to the linear motor's force loading F_{load}, a Wheatstone bridge circuit and an instrumentation amplifier are used. The fundamental aim of the circuit is to detect the changes in the unknown resistance value of R_{PR}, which tends to vary under the applied mechanical stress [64]. The calibration of the circuit relies on balancing two branches of the Wheatstone bridge circuit. In other words, the output voltage should be zero-volt in case the sensing mechanism is situated in its original position. In order to arrange the zero position of the read-out system, an identical 200 kΩ potentiometer is added into the circuit as R_{REF} shown in Figure 5.2. The linear motor triggers the system by applying force F_{load} to any segment, and the resistance value increases if the segment contains a graphite layer. Based on the respective changes of the voltage measurements, the incident force magnitude can be calculated.

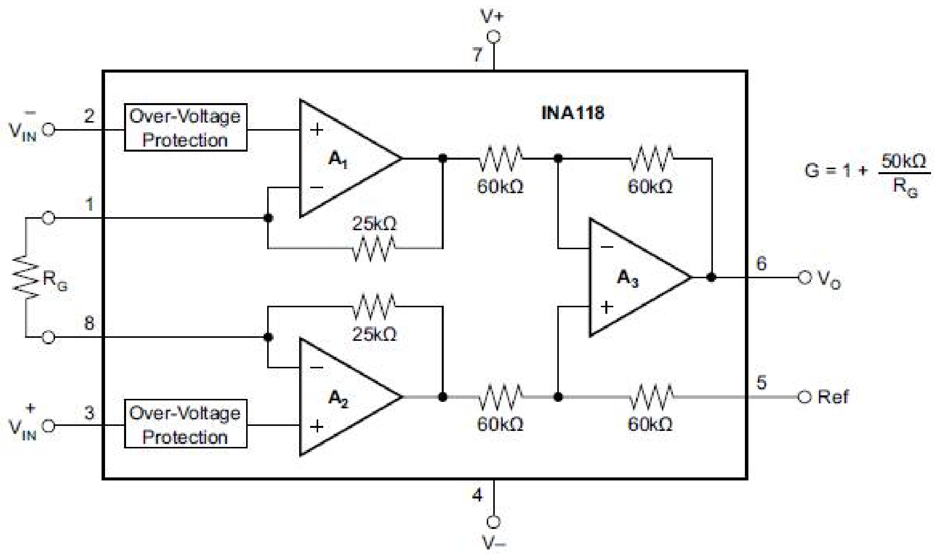

Figure 5.3: Simplified schematic of the instrumental amplifiers (Texas Instruments® INA118P).

Table 5.1: Pin functions of Texas Instruments® INA118P.

Pins	Symbols	Descriptions
1 & 8	R_G	Gain setting
2	V_{IN-}	Negative voltage input
3	V_{IN+}	Positive voltage input
4	V_-	Negative voltage supply
5	REF	Reference input
6	V_{OUT}	Output voltage
7	V_+	Positive voltage supply

$$G = \frac{50k\Omega}{R_G} + 1 \tag{5.2}$$

In order to further enhance the sensitivity of the system, the instrumentation amplifier (INA118P) shown in Figure 5.3, is integrated into the circuit [62,75,76]. The reasons for using the amplifier can be listed as follows: (1) high-CMRR (common-mode rejection ratio), (2) high-SNR (signal-to-noise ratio), (3) high input resistance, and low offset voltage, (4) low input bias current, and finally (5) low drift. Also, pins of the INA 118P is tabulated in Table 5.1. These features allow the output voltage, which varies depending on the resistance change in the piezoresistive layer, to be detected more clearly, sensitively, and perceptibly. The gain of each amplifier G is arranged as 10 V/V based on the Equation 5.2. The output voltage of the circuit under augmented stress in the piezoresistive graphite layers, is amplified via INA118P and fed into a real-time controller (Dynomotion® KFlop & KAnalog series motion controller).

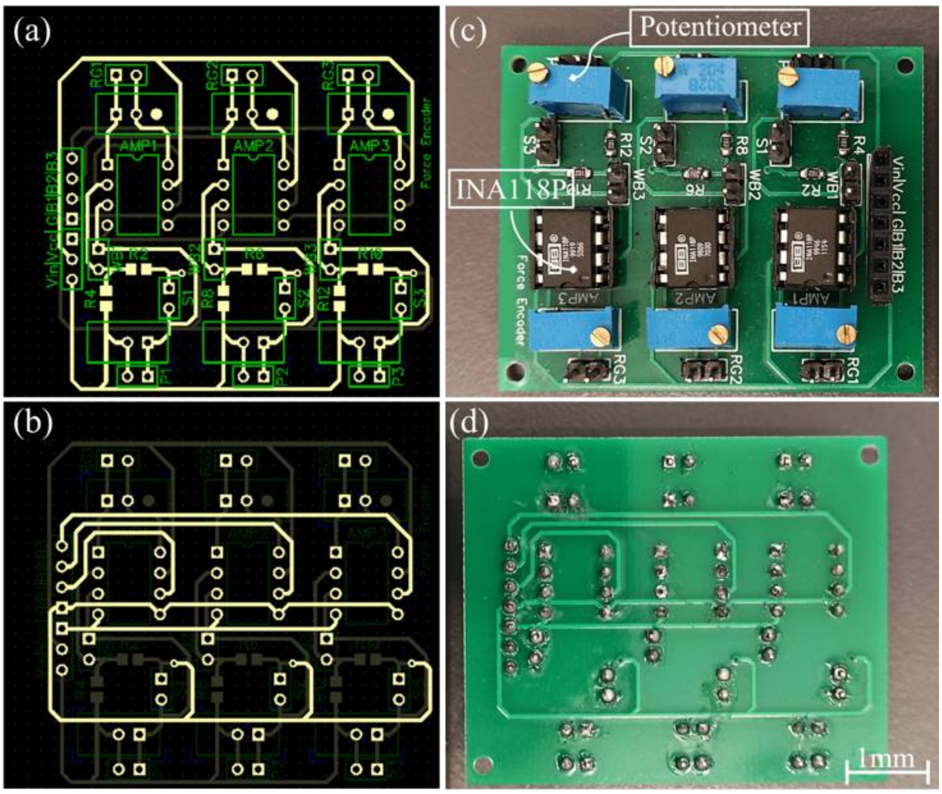

Figure 5.4: (a) and (b) top and bottom views of the schematic of the proposed electronic read-out circuit. (c) and (d) top and bottom views of the printed circuit board for the proposed electronic read-out circuit. An implemented PCB has dimensions of 54 mm x 44 mm and its components are shown inset.

The proposed electronic read-out circuit is executed utilizing surface mount devices as a printed circuit board (PCB) shown in Figures 5.4c and 5.4d. It can design with the length and width dimensions of 54 mm x 44 mm, respectively. A dual-edge card connector (Amtek® 5FP1B1SND-08T0BLT-01) is plugged onto the ears of the linear absolute force encoder structure.

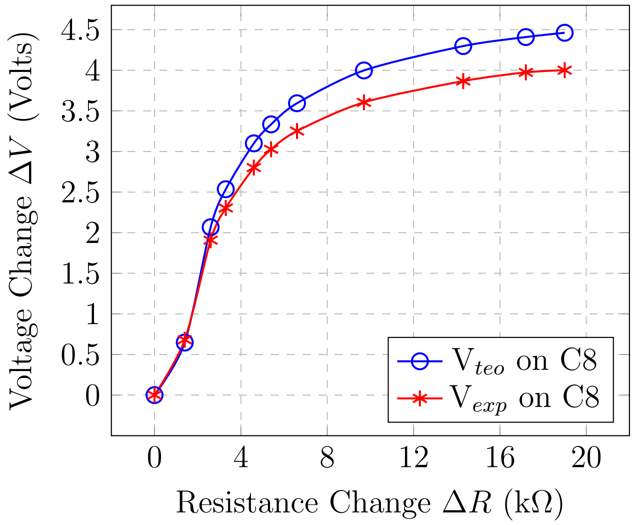

Figure 5.5: Plot of the output voltage change (ΔV) as a function of resistance change (ΔR). Blue line corresponds to the theoretical results of the proposed read-out circuit, whereas red line corresponds to the experimental results of the system with implemented PCB.

The proposed electronic read-out circuit is calculated for an increasing value of R_{PR} and plotted as V_{teo} in Figure 5.5. It is also tested with an implemented PCB, and the experimental results are indicated as V_{exp}. On the other hand, the test setup elaborately shown in Section 6 is designed to detect the magnitude of the applied force and the location where it is applied. The force is generated by a linear motor with different magnitudes.

6. EXPERIMENTS

This chapter elaborates on the experimental works of the fabricated paper-based piezoresistive force encoding sensor. Section 6.1 shows the experimental test setup of the force encoding system output. Section presents force encoding system calibration and various test results of the experiments.

6.1. Test Setup

In the following step, the proposed paper-based piezoresistive force encoding system is tested along with its electronic read-out circuit as shown in Figure 6.1, the experimental test setup that is used to characterize and test the proposed paper-based piezoresistive force encoding system. The system is composed of (1) the proposed linear absolute encoder sensor structure to sense applied force, (2) a single-channel power supply to activate the real-time controller (Dynomotion® KFlop & KAnalog series motion controller) and a three-channel power supply (Rohde&Schwarz® HMP3030) to drive the read-out system and the pantograph robot, (3) a real-time controller (Dynomotion® KFlop & KAnalog series motion controller) to collect data that occurs as a result of changes on force encoding structure and control the motion, (4) a pantograph robot arm for the lateral motion of the force encoding structure with high precision, (5) a linear motor to exert an F_{load} to mimic the ambient impact, and finally a PC to monitor and process these data is installed.

The setup is installed with its components to monitor the behaviour of the designed and implemented system is shown in Figure 6.1. The paper-based piezoresistive force encoding sensor preserved between two reverse silicone mold structures is fixed to the rail floor to prevent shaking on the structure during the force applied by the linear motor and move through the x-axis via a pantograph robot. Within the experiments, the linear motor that can move in y-axis direction with a step size of 0.5 μm easily manipulates the silicone mold structures to apply precise force owing to its rollers located to the tip of it. The known force value from the robotic system is relevantly created using Dynomotion® KFlop & KAnalog series motion controller board. Bending silicone mold structures under force application activate one segment of the paper-based force encoder structure. The location of the segment that the linear motor will trigger is determined by the pantograph robot, which arises from two identical rotary motors. As a result, a robotic pantograph presents the random segment travelling so that the linear motor can hit all of the segments with specified forces.

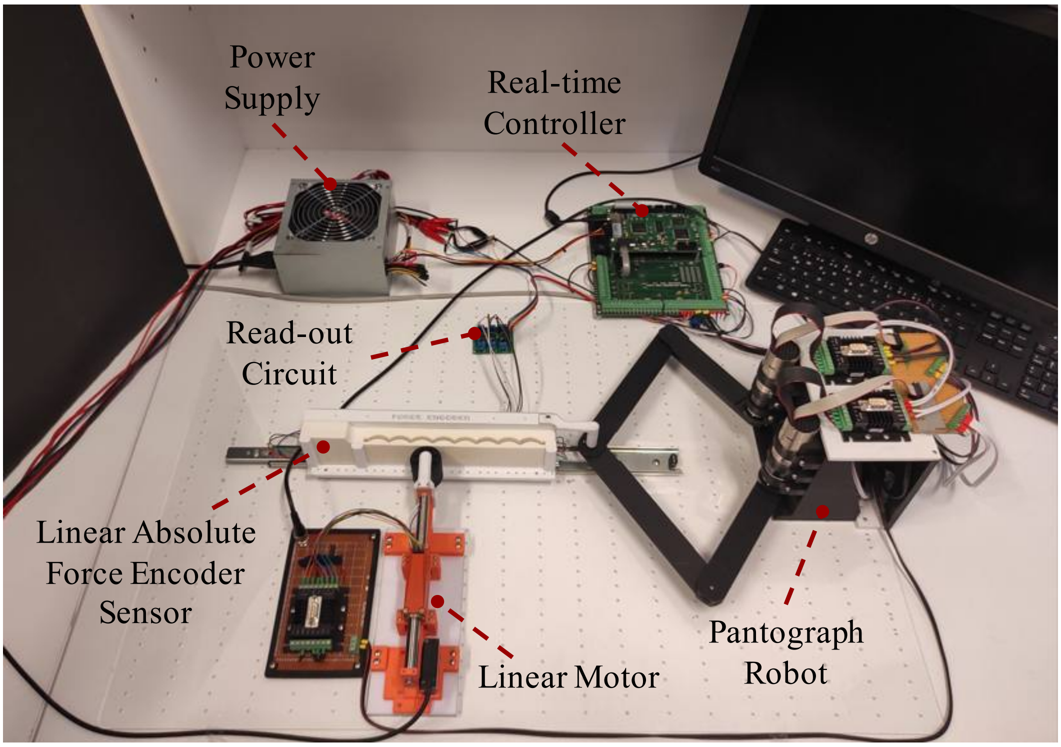

Figure 6.1: View of the experimental setup used to monitor magnitude and localization of the exerted force on the proposed sensing system.

It is previously explained that the level of resulting stress at the anchor points of the paper-based force encoder sensor increases in the direction of proportion to the magnitude of applied force and hence the amount of deflection δ_{AB} caused by the bending of the paper-based structure. Thereby, the resistance changes of related bits that contain graphite pad on its surface are monitored as voltage data through the medium of a read-out circuit. In that vein, it is aimed to detect, firstly, which normalized voltage change $\Delta V/V$ value corresponds to the loading force F_{load} and dynamic operating range of the force encoder sensor. Secondly, the location on the sensor through the voltage value corresponding to the known loading force F_{load} applied to a particular segment, and finally, the robustness against plastic deformation via the voltage value corresponding to applying in a particular configuration loading force F_{load} as the static and point.

6.2. Test Results

The behaviour of the implemented force encoder under fluctuating force loading (F_{load}) is plotted in Figure 6.2. According to the experiment, when the load force F_{load} magnitude is gradually increased from zero to 14N with the help of the linear motor indicated in Figure 6.1, the normalized changes ΔV/V due to resistance changes of the proposed force encoding sensor are monitored. As highlighted in Figure 6.2, values increase linearly for R1-C8, R2-C8, and R3-C8 locations from 0 to 3.048 V/V, from 0 to 3.877 V/V, and from 0 to 5.0387 V/V, respectively.

Apart from these, the hysteresis behaviours of the paper-based piezoresistive force encoding sensor are acquired when the load force F_{load} gradually decreases from 14N to zero while the linear motor continually moves to the negative direction on the same axis. Thus, as emphasized in 6.2, the normalized voltage changes while decreasing the magnitude of F_{load} are reported that linearly decreasing from 3.048 to 0.3565 V/V for R1-C8, 3.8770 to 0.4697 V/V for R2-C8, and 5.0387 to 0.6382 V/V for R3-C8.

Moreover, as shown in Figure 6.2, once the applied force exceeds 12N, the gap between the upper and lower part of the silicone sandwich structure shown in Figure 4.3, S_{GAP}, goes to zero. Thus one can not bend the paper-based sensor furthermore, and the change in the normalized voltage saturates even though the exerted force is further increased. As seen from the plot, the sensor has a slight hysteresis behaviour due to the plastic deformation occurring in the paper structure and piezoresistive layers. The linear part of this plot defines the dynamic range of the proposed force encoding system, and it is between 0.6 and 12N.

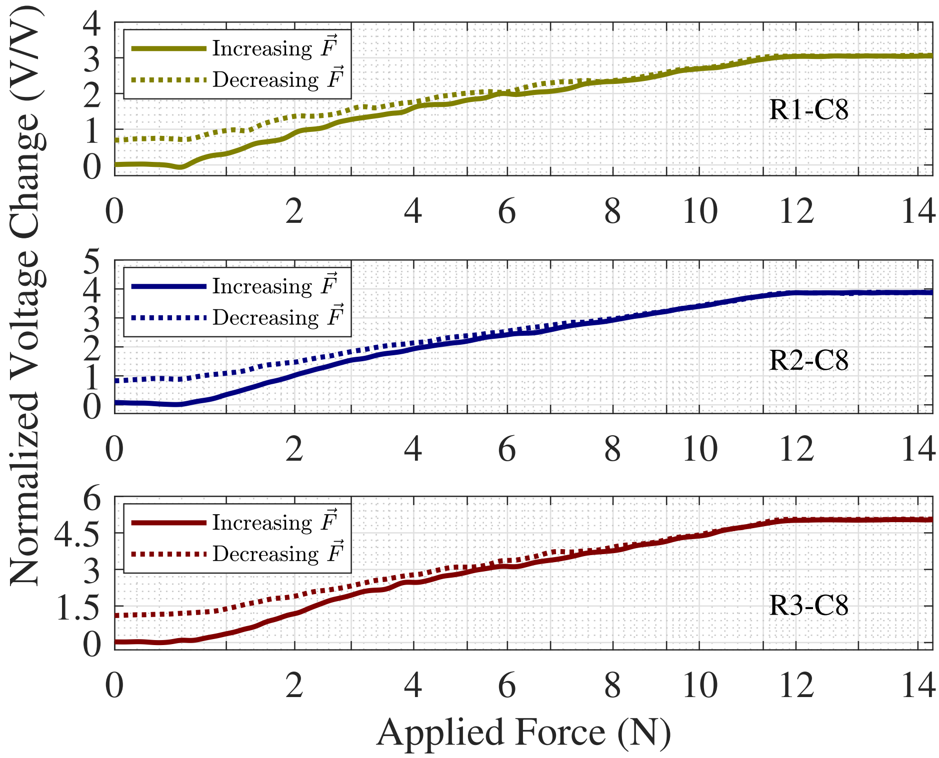

Figure 6.2: A calibration graph of the force encoder sensor shows the hysteresis behaviour of the proposed sensor by plotting the normalized voltage changes versus the bending force. The smooth lines represent the incremental F_{load} dependent ΔV/V value, whereas the dashed lines represent the gradually decreasing load force from 14N to zero.

The subsequent experiment was carried out by gradually increasing the force through the linear motor to determine the root mean squared error (RMSE) of the sensor. The applied force increases from 0.5N (minimum detectable force) to 2.5N, where the sensitivity is highest with a step size of 0.1N. The normalized voltage changes versus the applied force behaviour of the proposed force encoding sensor are plotted in Figure 6.3 for three different rows on segment 8. It is reported that normalized voltage changes ΔV/V for the first, second, and third row, respectively, linearly increase from 0.0159 to 0.3109 V/V, 0.0161 to 0.3104 V/V, and 0.0071 to 0.2984 V/V. The average error margins for the proposed sensor is measured as 0.0175 V/V. Within the same figure, The black and dashed line corresponds to the average ΔV/V (sensitivity) starting from 0.5 to 2.5 V/V, and it is defined as 0.1468 mV/(mN·mV). The linear range

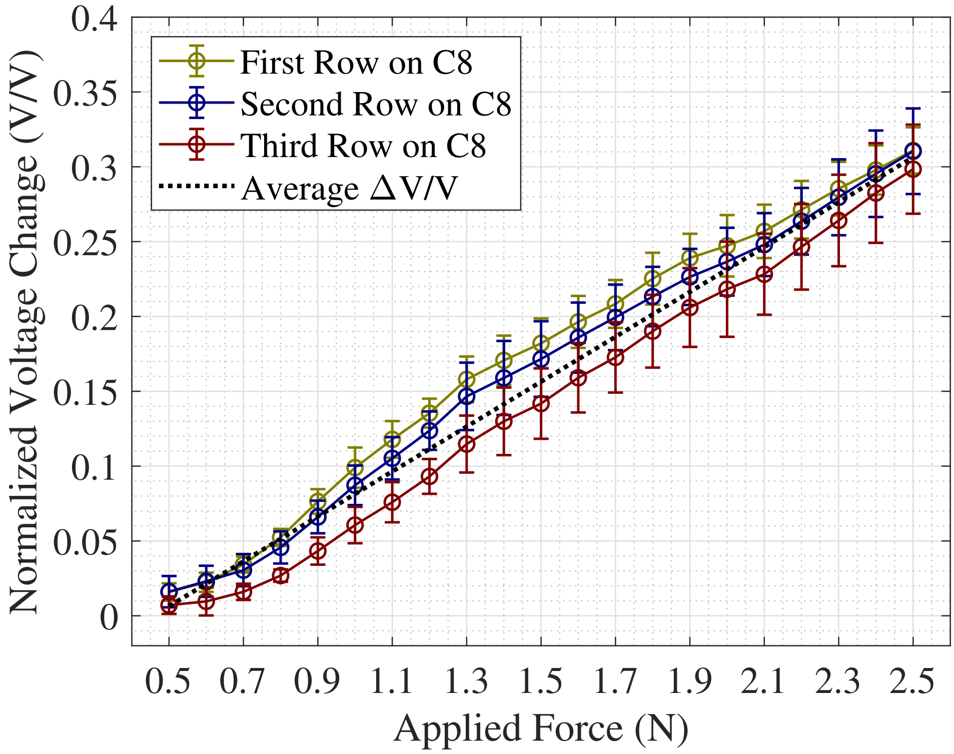

Figure 6.3: Illustrates the performance of the sensor while getting actuated in the most sensitive linear region. The dashed line in the this part represents the curve fitted equation of $y = 0.15x - 0.0686$ with an R-squared value of 0.99.

behaviour of this sensor can be modelled with $y = 0.15x - 0.0686$ with an R-squared value of 0.99.

According to these experimental results, our proposed force encoder sensor is calibrated as a mechanical process related to piezoresistive feedback converted into a normalized voltage change output. The magnitude of the randomly applied force will be obtained.

Figure 6.4 and 6.5 shows the localization experiments of the impact point using the proposed paper-based piezoresistive force encoder. In order to measure the performance of the detection, the pantograph robot arm moves through the x-axis and displace the force encoder sensor. The linear motor was rolled over the overall structure by applying force to provide temporary deformation. Bending silicone molds under a force application activate one segment of the paper-based force encoder structure.

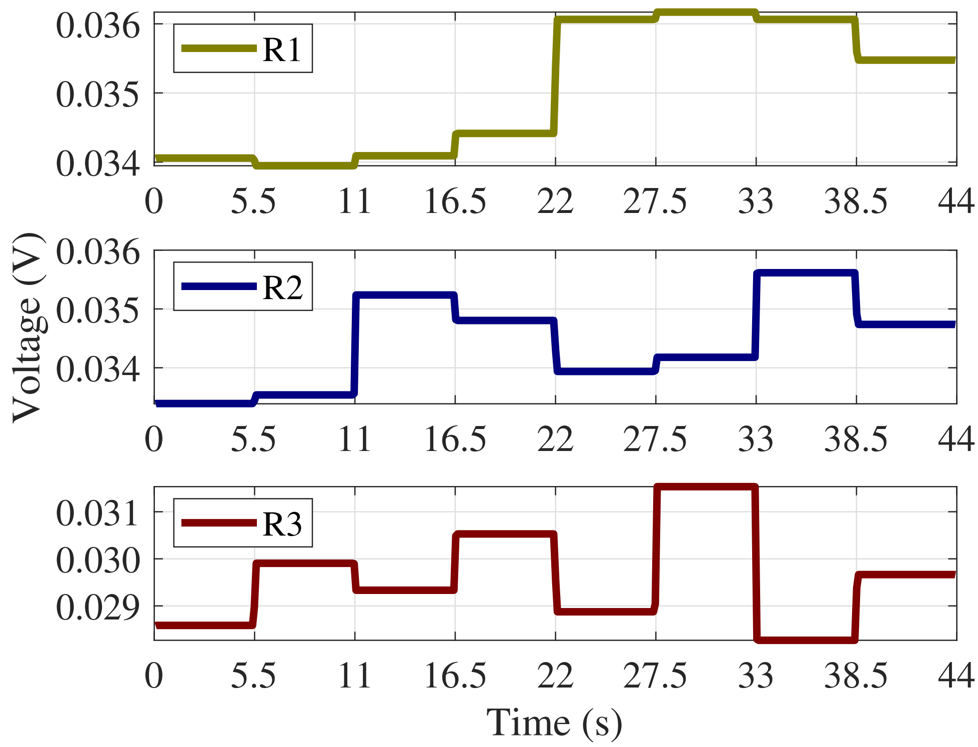

Figure 6.4: The paper-based sensor is continuously triggered on the x-direction with the help of the pantograph robotic arm. Shows the analog output of the sensor system.

The sensor is kept under a 1N force in the orthogonal direction by the linear motor. Meanwhile, the resistance changes $\Delta R/R$ on each segment was recorded by the real-time controller indicated in Figure 6.1 as a time-series data with a sampling period of $180\mu s$. The real-time measurement and control algorithm which is generated using a C code. The code is generated in the KMotion interface of the Dynomotion real-time control board.

In order to evaluate the performance of the system in a real environment, some preliminary experiments are carried out to determine the threshold levels of each segment that will provide the transition between analog and digital data. These threshold levels are then used in the real-time measurement system to determine the localization of the segment where the force is applied. The resultant changes in the voltages are recorded and the threshold values of the rows are selected using the recorded data. Figure 6.4 plots the time-dependent voltage values acquired directly from the sensor, whereas Figure 6.5 shows the digital version of the same output after applying tailored

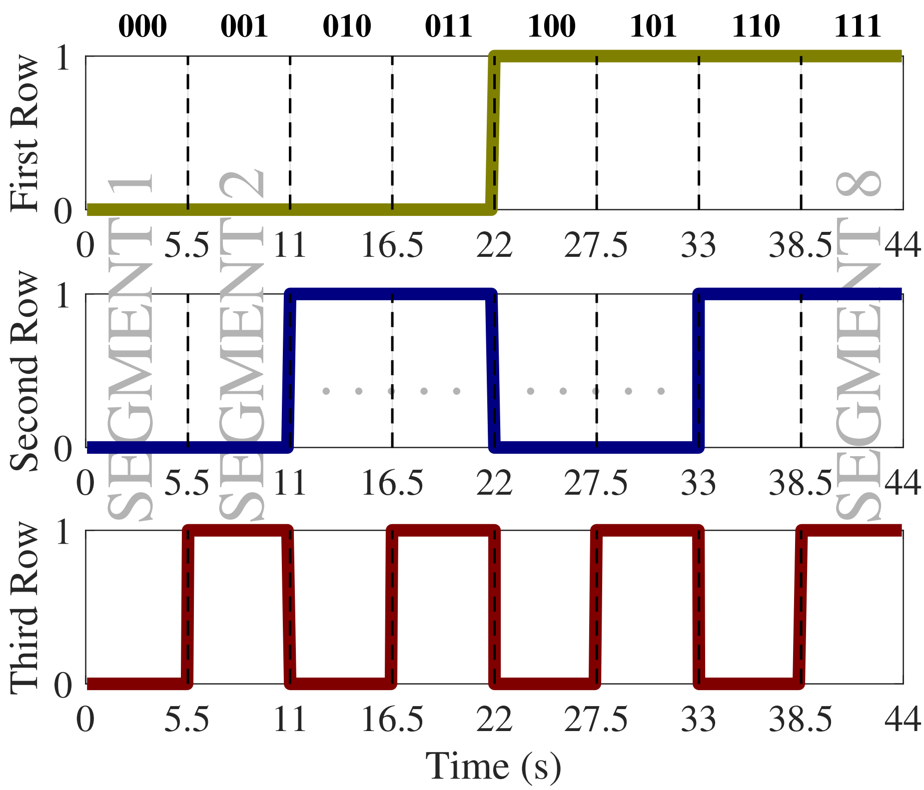

Figure 6.5: The paper-based sensor is continuously triggered on the x-direction with the help of the pantograph robotic arm. Plots the digital version of the same output after careful thresholding.

thresholding. The numerical values of those thresholds that is determined according to the experimental results shown in Figure 6.4, are 34.42 mV, 34.18 mV, and 29.16 mV, respectively for the first, second, and the third rows of the structure. In the transitions between segments, small rising and falling values are seen. The reason for this is that while the pantograph robot moves the structure along the x-axis, the cylindrical structure at the tip of the linear motor slides along the silicon structure by applying a certain force and passes over the support points in the transitions between the segments. As we emphasized in this plot, the digital output for segment 1 is 000, whereas the output for segment eight is given as 111.

After the experiments carried out to determine the magnitude of the applied force, the dynamic operating range of the system and the location of the segment where the force is applied, various force patterns were applied to the proposed paper-based force encoder structure. Therefore the robustness of the structure against plastic deformation

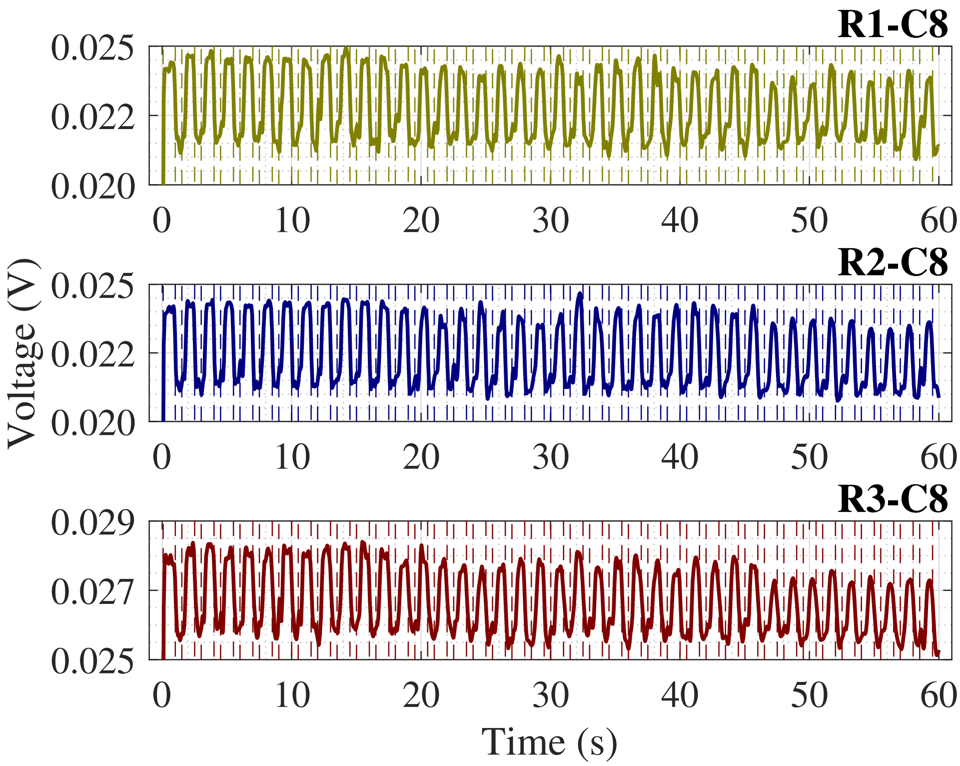

Figure 6.6: The output voltage of the system under the application of 1N point-forces with period 1.25 seconds.

and time response was tested to observe its performance in the real environment.

The response of the proposed implemented force encoding structure to various contact patterns that are point-force, static force, and combined application is monitored and plotted in Figure 6.6, 6.7, and 6.8, respectively. Once again, the 8^{th} segment of the paper-based piezoresistive sensor is employed to measure the performance of the system. The voltage output of the system, which consists of a paper-based piezoresistive force encoding sensor and a silicon mold that increases bending-enhancing, is plotted by the linear motor as a result of the various force loading patterns as point and static force applied to each bit on segment 8 using the test system along the line A-A' and within the contact area specified in Figure 3.21. Figure 6.6 demonstrates the voltage outputs of the system under successive force loads of 1N with a cyclic frequency of 0.67 Hertz (40cycles/60sec) and 0.3 seconds average frequency response precision for each row on segment 8. It is seen that the system has not undergone any significant deformation.

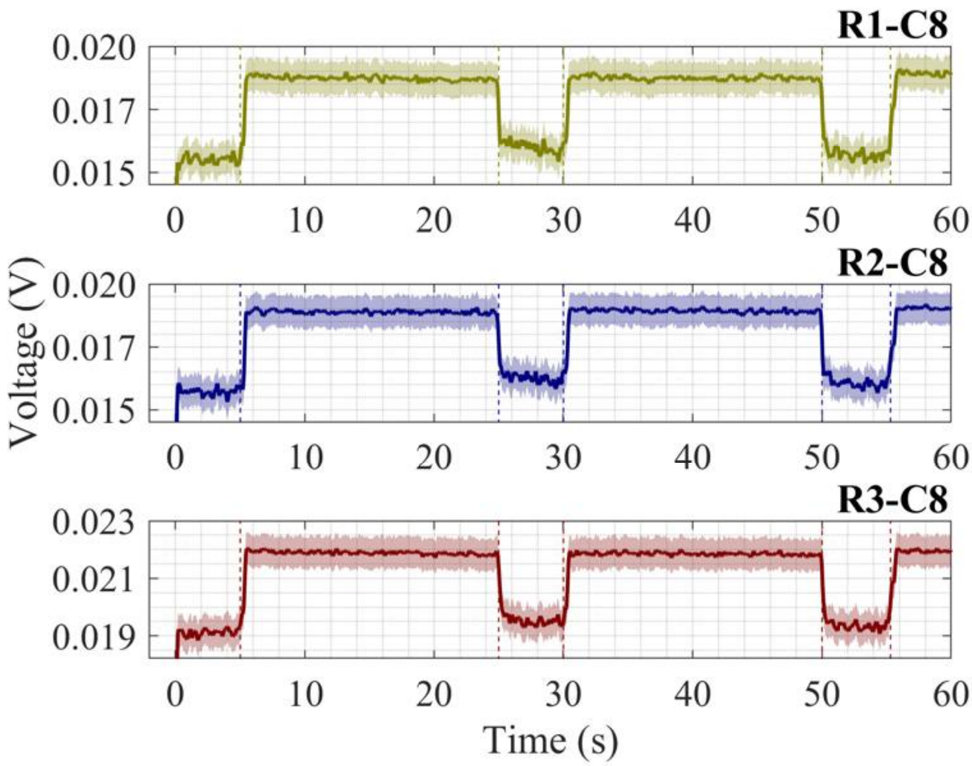

Figure 6.7: The output voltage of the system under the application of 1N static forces with period of 20 seconds, together with their respective error values.

Moreover, the proposed system is also tested for more extended static force exertions as it is plotted in Figure 6.7. This time, the system can detect and follow the actuating force that is applied without cessation for a period of 5 seconds. This experiment with static force exertion has been repeated to understand the error band of the sensor. We can state that average error value for the first bit is 0.14181 mV, 0.26128 mV for the second bit, and finally 0.19946 mV for the third bit. Additionally, the standard deviation values are reported as 0.0013, 0.0013, and 0.0011 for the first, second, and third bit, respectively.

In the last experiment, the system is tested for mixed-signals, static and alternating force exertions, and monitored. The result, which is presented in Figure 6.8 shows the voltage output of the proposed force encoder system under such force patterns. These experiments show that the proposed system performs on robotic structures in real experimental environments that do not require going up to high-frequency levels, has high response sensitivity, no considerable plastic deformation is detected, and

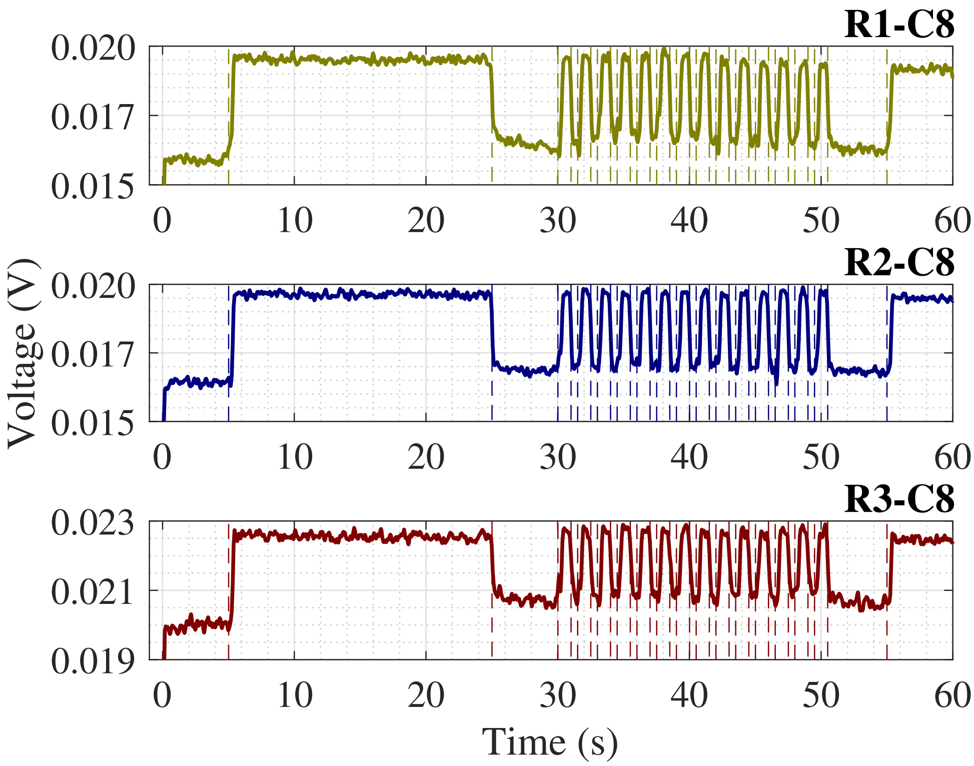

Figure 6.8: The output voltage of the system under combined application of 1N point-force and static force with the average of 0.3 seconds time response.

the low-cost disposable sensor works appropriately in the required short interval of operation time.

We report that the proposed system can detect a minimum 0.6N force (0.181 ΔV/V) and costs approximately \$0.2 per device. The sensor covers an area of 36.75 cm^2 and is able to differentiate the position of the impacts with a resolution of 2.4 cm in x- and 0.55 cm in y-directions (a 3 x 8 force encoding array is used). The measured quantities and properties peculiar to the proposed sensing system are tabulated in Table 7.1.

7. DISCUSSION

This study aims to design and fabricated a low-cost piezoresistive linear absolute force encoding sensor to measure the magnitude of the applied force, the location of the segment where the force is applied, and the robustness against to the plastic deformation under the various force patterns. Numerous fabrication methods and materials is elaborated by comparing with the literature. In this context, it has been reported that paper-based structures are sensitive enough and can be integrated into the system because they are cheap, off-the-shelf, and easy and quick to fabricate for use in robotic systems.

As clarified in the above sections, within the scope of this study, a paper-based, easy- and quick- fabricated, perforated linear absolute force encoder structure coated with a serpentine piezoresistive layer has been proposed as a novel method in order to measure the magnitude of the applied force (F_{load}) and to detect the impact location where it is applied. In this way, the magnitude and location of the applied force are precisely determined and the effective Young's Modulus (E_{eff}) is reduced.

In this study, using this proposed force encoding methodology, a sufficiently sensitive structure was improved compared to the flexible silicon-based tactile sensor [77], and the flexible polyimide-based sensors [78, 79]. Although the proposed paper-based force encoding sensor structure has lower spatial resolution, high force resolution and time response were obtained by using a low-cost, easy and quick silk-stencil fabrication method, contrary the difficult, expensive and long fabrication methods used in other studies. A brief comparison between this thesis and studies reported in [77], [78] and [79] is given in Table 7.1.

Considering the elements highlighted above, the sensitivity value obtained from the system can be improved in the future with some innovations and improvements. For example, (1) the low-cost substrate material of the system is able to be selected as a more flexible material, (2) the resolution can be reduced by designing a higher bit structure, (3) a new voltage amplifier with higher SNR can be selected, a more sensitive read-out circuit can be designed, and (4) Compared with silicone, the mold structure in which the sensor is located can be covered with a structure that has more similar physical properties to human skin.

Table 7.1: Comparison of specifications of our proposed paper-based piezoresistive force encoding sensor regarding its detection capability of the force magnitude and its impact localization to the other works.

Specifications	**This work**	**Reference [77]**	**Reference [78]**	**Reference [79]**
Substrate Material	Strathmore® 400 series Bristol paper (289 μm thick)	Silicone Rubber RTV (100 μm thick)	Polyimide (125 μm thick)	FPC
Array Form	8 × 3 (Linear absolute)	4 × 4 (Matrix)	4 × 4 (Matrix)	3 × 3 (Matrix)
Array Size (L × w × t) (mm)	198 × 18.5625 × 0.289	20 × 20 × 0.1	2.5 × 2.5 × 0.05	21 × 21 × 2.7
Spatial Resolution	24 mm × 5.5 mm	5 mm × 5 mm	0.6 mm × 0.6 mm	5 mm × 5 mm
Force Range	0.6 - 12 N	0.05 - 2 N	0 - 0.8 N	0 - 20 N
Detected Force Step	0.1 N	0.05 N	0.2 N	2 N
Sensitivity	5.5 mV/mN	0.45 V/N	206.6 mV/N	0.251 V/N
Sensing Material	Graphite paste (Bare Conductive® Electric paint)	Graphene nanoplate	Nichrome (NiCr)	Conductive rubber (INASTAMOR)
Fab. Method for Sensing Material	Silk screen printing	Spin coating	Spin coating	Spin coating
Electrode Material	Silver paste (Baku® Bk-426)	AgNF	Au	Copper
Fabrication Process	<30 minutes in laboratory	<5 hour in laboratory	<2.5 hour in any place	<3.5 minutes in laboratory
Time Response	0.3 secs	0.2 secs	Not available	Not available
BoM	$0.2	Not available	Not available	Not available

8. CONCLUSIONS AND FUTURE WORKS

In this thesis, a paper-based piezoresistive linear absolute encoder force encoding sensor system has been designed, fabricated and characterized. Implemented disposable structure is used to detect both the applied force magnitude and its position in real-time. The scope of this study does not aim to improve a gold standard force encoder device. Therefore, it is essential to note that the sensing structure is designed for single usage; hence fabricated using low-cost, off-the-shelf components has acceptable sensitivity and resolution values for robotic applications. For this purpose, the fabrication materials of the proposed disposable linear absolute force encoder are chosen as a 289 μm thick Strathmore® 400 series Bristol paper, graphite (Bare Conductive® Electric Paint), and RTV-2 silicone molds. In order to detect the applied force more precisely and to increase the clarity of the localization, approximately 50 μm thick piezoresistive graphite paste is coated on the paper-based linear absolute encoder structure. Additionally, the proposed paper-based structure has rows of closely spaced perforation on pre-specified locations to facilitate the force encoder's bending and further increase the system's sensitivity. Apart from these, a peripheral electronic read-out circuit customized for the 3-bit linear absolute force encoder structure is developed and integrated into the system. As tabulated in Table 7.1, experiment results show that the fabricated force encoder structure can measure point-force with a 0.1N step size and detect the location of the applied force in a flexible medium. At the same time, the implemented sensor has 0.6N minimum detectable force with an output of 0.0183 V/V, and sensitivity of 5.5 mV/mN. Therefore, results illustrate that the proposed system can be effectively used in flexible structures like soft robots.

As part of future work, more flexible, lower-cost, a polyimide-based force encoding sensor is developed, whose substrate material is more flexible and low-cost, has higher spatial resolution, and has integrated read-out circuitry. This sensor structure is implemented on a robotic arm and then the force feedback motion control system of the robotic arm is provided.

REFERENCES

1. Hou, C., Z. Xu, W. Qiu, R. Wu, Y. Wang, Q. Xu, X. Y. Liu and W. Guo, "A Biodegradable and Stretchable Protein-Based Sensor as Artificial Electronic Skin for Human Motion Detection", *Small*, Vol. 15, No. 11, p. 1805084, 2019.

2. Zhao, X.-F., C.-Z. Hang, H.-L. Lu, K. Xu, H. Zhang, F. Yang, R.-G. Ma, J.-C. Wang and D. W. Zhang, "A skin-like sensor for intelligent Braille recognition", *Nano Energy*, Vol. 68, p. 104346, 2020.

3. Liu, K., Y. Wu, S. Wang, H. Wang, H. Chen, B. Chen and J. Yao, "Artificial Sensitive Skin for Robotics Based on Electrical Impedance Tomography", *Advanced Intelligent Systems*, Vol. 2, No. 4, p. 1900161, 2020.

4. Takei, K., W. Gao, C. Wang and A. Javey, "Physical and chemical sensing with electronic skin", *Proceedings of the IEEE*, Vol. 107, No. 10, pp. 2155–2167, 2019.

5. Chortos, A., J. Liu and Z. Bao, "Pursuing prosthetic electronic skin", *Nature materials*, Vol. 15, No. 9, pp. 937–950, 2016.

6. Seminara, L., M. Franceschi, L. Pinna, A. Ibrahim, M. Valle, S. Dosen and D. Farina, "Electronic skin and electrocutaneous stimulation to restore the sense of touch in hand prosthetics", *2017 IEEE International Symposium on Circuits and Systems (ISCAS)*, pp. 1–4, IEEE, 2017.

7. He, S., S. Feng, A. Nag, N. Afsarimanesh, T. Han and S. C. Mukhopadhyay, "Recent Progress in 3D Printed Mold-Based Sensors", *Sensors*, Vol. 20, No. 3, p. 703, 2020.

8. Ma, Z., S. Li, H. Wang, W. Cheng, Y. Li, L. Pan and Y. Shi, "Advanced electronic skin devices for healthcare applications", *Journal of Materials Chemistry B*, Vol. 7, No. 2, pp. 173–197, 2019.

9. Han, T., A. Nag, N. Afsarimanesh, F. Akhter, H. Liu, S. Sapra, S. Mukhopadhyay and Y. Xu, "Gold/Polyimide-Based Resistive Strain Sensors", *Electronics*, Vol. 8, No. 5, p. 565, 2019.

10. Dahiya, R., "Electronic skin", *2015 XVIII AISEM Annual Conference*, pp. 1–4, IEEE, 2015.

11. Saadatzi, M. N., J. R. Baptist, Z. Yang and D. O. Popa, "Modeling and Fabrication of Scalable Tactile Sensor Arrays for Flexible Robot Skins", *IEEE Sensors Journal*, Vol. 19, No. 17, pp. 7632–7643, 2019.

12. Sun, X., J. Sun, T. Li, S. Zheng, C. Wang, W. Tan, J. Zhang, C. Liu, T. Ma, Z. Qi *et al.*, "Flexible tactile electronic skin sensor with 3D force detection based on porous CNTs/PDMS nanocomposites", *Nano-micro letters*, Vol. 11, No. 1, pp. 1–14, 2019.

13. Xie, M., K. C. Aw and W. Gao, "Skin force sensor using piezoresistive PEDOT: PSS with arabitol on flexible PDMS", *2015 IEEE SENSORS*, pp. 1–4, IEEE, 2015.

14. Wang, H., "Development of a conformable electronic skin based on silver nanowires and PDMS", *IOP Conf Ser Mater Sci Eng*, Vol. 207, pp. 0–6, 2017.

15. Li, H., T. K. Sinha, J. S. Oh and J. K. Kim, "Soft and flexible bilayer thermoplastic polyurethane foam for development of bioinspired artificial skin", *ACS applied materials & interfaces*, Vol. 10, No. 16, pp. 14008–14016, 2018.

16. Han, H., Y. Nakagawa, Y. Takai, K. Kikuchi and S. Tsuchitani, "PVdf film micro fabrication for the robotics skin sensor having flexibility and high sensitivity", *2011 Fifth International Conference on Sensing Technology*, pp. 603–606, IEEE, 2011.

17. He, H., Y. Fu, W. Zang, Q. Wang, L. Xing, Y. Zhang and X. Xue, "A flexible self-powered T-ZnO/PVDF/fabric electronic-skin with multi-functions of tactile-perception, atmosphere-detection and self-clean", *Nano Energy*, Vol. 31, pp. 37–48,

2017.

18. Mahanty, B., K. Maity, S. Sarkar and D. Mandal, "Human skin interactive self-powered piezoelectric e-skin based on PVDF/MWCNT electrospun nanofibers for non-invasive health care monitoring", *Materials Today: Proceedings*, Vol. 21, pp. 1964–1968, 2020.

19. Missinne, J. and B. Hoe, "Artificial skin based on flexible optical tactile sensors", *SPIE Newsroom*, Vol. 25, 2010.

20. De Rossi, D., F. Carpi and E. P. Scilingo, "Polymer based interfaces as bioinspired 'smart skins"', *Advances in colloid and interface science*, Vol. 116, No. 1-3, pp. 165–178, 2005.

21. Pan, X., Q. Wang, P. He, K. Liu, Y. Ni, L. Chen, X. Ouyang, L. Huang, H. Wang and S. Xu, "A bionic tactile plastic hydrogel-based electronic skin constructed by a nerve-like nanonetwork combining stretchable, compliant, and self-healing properties", *Chemical Engineering Journal*, Vol. 379, p. 122271, 2020.

22. Dai, S., S. Wang, H. Yan, J. Xu, H. Hu, J. Ding and N. Yuan, "Stretchable and self-healable hydrogel-based capacitance pressure and strain sensor for electronic skin systems", *Materials Research Express*, Vol. 6, No. 8, p. 0850b9, 2019.

23. Fu, R., L. Tu, Y. Zhou, L. Fan, F. Zhang, Z. Wang, J. Xing, D. Chen, C. Deng, G. Tan *et al.*, "A Tough and Self-Powered Hydrogel for Artificial Skin", *Chemistry of Materials*, Vol. 31, No. 23, pp. 9850–9860, 2019.

24. Huang, Y., H. Yuan, W. Kan, X. Guo, C. Liu and P. Liu, "A flexible three-axial capacitive tactile sensor with multilayered dielectric for artificial skin applications", *Microsystem Technologies*, Vol. 23, No. 6, pp. 1847–1852, 2017.

25. Sun, Q., W. Seung, B. J. Kim, S. Seo, S.-W. Kim and J. H. Cho, "Active matrix electronic skin strain sensor based on piezopotential-powered graphene transistors",

Advanced Materials, Vol. 27, No. 22, pp. 3411–3417, 2015.

26. Ge, J., L. Sun, F.-R. Zhang, Y. Zhang, L.-A. Shi, H.-Y. Zhao, H.-W. Zhu, H.-L. Jiang and S.-H. Yu, "A stretchable electronic fabric artificial skin with pressure-, lateral strain-, and flexion-sensitive properties", *Advanced materials*, Vol. 28, No. 4, pp. 722–728, 2016.

27. Yao, G., L. Xu, X. Cheng, Y. Li, X. Huang, W. Guo, S. Liu, Z. L. Wang and H. Wu, "Bioinspired triboelectric nanogenerators as self-powered electronic skin for robotic tactile sensing", *Advanced Functional Materials*, Vol. 30, No. 6, p. 1907312, 2020.

28. Klimaszewski, J., D. Janczak and P. Piorun, "Tactile robotic skin with pressure direction detection", *Sensors*, Vol. 19, No. 21, p. 4697, 2019.

29. Liu, Y.-Q., Z.-D. Chen, J.-W. Mao, D.-D. Han and X. Sun, "Laser fabrication of graphene-based electronic skin", *Frontiers in chemistry*, Vol. 7, p. 461, 2019.

30. Cataldi, P., S. Dussoni, L. Ceseracciu, M. Maggiali, L. Natale, G. Metta, A. Athanassiou and I. S. Bayer, "Carbon nanofiber versus graphene-based stretchable capacitive touch sensors for artificial electronic skin", *Advanced Science*, Vol. 5, No. 2, p. 1700587, 2018.

31. Ma, C.-W., L.-S. Hsu, J.-C. Kuo and Y.-J. Yang, "A flexible tactile and shear sensing array fabricated using a novel buckypaper patterning technique", *Sensors and Actuators A: Physical*, Vol. 231, pp. 21–27, 2015.

32. Hu, C.-F., W.-S. Su and W. Fang, "Development of patterned carbon nanotubes on a 3D polymer substrate for the flexible tactile sensor application", *Journal of Micromechanics and Microengineering*, Vol. 21, No. 11, p. 115012, 2011.

33. Wang, Y., X. Wu, D. Mei, L. Zhu and J. Chen, "Flexible tactile sensor array for distributed tactile sensing and slip detection in robotic hand grasping", *Sensors and Actuators A: Physical*, Vol. 297, p. 111512, 2019.

34. Li, X., W. Huang, G. Yao, M. Gao, X. Wei, Z. Liu, H. Zhang, T. Gong and B. Yu, "Highly sensitive flexible tactile sensors based on microstructured multiwall carbon nanotube arrays", *Scripta Materialia*, Vol. 129, pp. 61–64, 2017.

35. Chun, S., J. Kim, C. Pang *et al.*, "A transparent, glue-free, skin-attachable graphene pressure sensor with micropillars for skin-elasticity measurement", *Nanotechnology*, Vol. 30, No. 33, p. 335501, 2019.

36. Li, H., K. Wu, Z. Xu, Z. Wang, Y. Meng and L. Li, "Ultrahigh-sensitivity piezoresistive pressure sensors for detection of tiny pressure", *ACS applied materials & interfaces*, Vol. 10, No. 24, pp. 20826–20834, 2018.

37. Tolvanen, J., J. Hannu and H. Jantunen, "Stretchable and washable strain sensor based on cracking structure for human motion monitoring", *Scientific reports*, Vol. 8, No. 1, pp. 1–10, 2018.

38. Ramalingame, R., Z. Hu, C. Gerlach, D. Rajendran, T. Zubkova, R. Baumann and O. Kanoun, "Flexible piezoresistive sensor matrix based on a carbon nanotube PDMS composite for dynamic pressure distribution measurement", *Journal of Sensors and Sensor Systems*, Vol. 8, No. 1, p. 1, 2019.

39. Khan, S., R. Dahiya, S. Tinku and L. Lorenzelli, "Conformable tactile sensing using screen printed P (VDF-TrFE) and MWCNT-PDMS composites", *SENSORS, 2014 IEEE*, pp. 862–865, IEEE, 2014.

40. Büscher, G. H., R. Kõiva, C. Schürmann, R. Haschke and H. J. Ritter, "Flexible and stretchable fabric-based tactile sensor", *Robotics and Autonomous Systems*, Vol. 63, pp. 244–252, 2015.

41. Takei, Y., S. Goto, S. Takamatsu, T. Itoh and T. Kobayashi, "Flexible contact pressure sensor based on ultrathin piezoresistive silicon membrane capable of strain compensation", *Sens. Mater*, Vol. 30, pp. 2999–3007, 2018.

42. Byun, J., Y. Lee, J. Yoon, B. Lee, E. Oh, S. Chung, T. Lee, K.-J. Cho, J. Kim and Y. Hong, "Electronic skins for soft, compact, reversible assembly of wirelessly activated fully soft robots", *Science Robotics*, Vol. 3, No. 18, 2018.

43. Mirza, F., R. R. Sahasrabuddhe, J. R. Baptist, M. B. Wijesundara, W. H. Lee and D. O. Popa, "Piezoresistive pressure sensor array for robotic skin", *Sensors for Next-Generation Robotics III*, Vol. 9859, p. 98590K, International Society for Optics and Photonics, 2016.

44. Boutry, C. M., M. Negre, M. Jorda, O. Vardoulis, A. Chortos, O. Khatib and Z. Bao, "A hierarchically patterned, bioinspired e-skin able to detect the direction of applied pressure for robotics", *Science Robotics*, Vol. 3, No. 24, 2018.

45. Baptist, J. R., R. Zhang, D. Wei, M. N. Saadatzi and D. O. Popa, "Fabrication of strain gauge based sensors for tactile skins", *Smart Biomedical and Physiological Sensor Technology XIV*, Vol. 10216, p. 102160F, International Society for Optics and Photonics, 2017.

46. Pang, G., J. Deng, F. Wang, J. Zhang, Z. Pang and G. Yang, "Development of flexible robot skin for safe and natural human–robot collaboration", *Micromachines*, Vol. 9, No. 11, p. 576, 2018.

47. O'Neill, J., J. Lu, R. Dockter and T. Kowalewski, "Stretchable, flexible, scalable smart skin sensors for robotic position and force estimation", *Sensors*, Vol. 18, No. 4, p. 953, 2018.

48. Sun, J.-Y., C. Keplinger, G. M. Whitesides and Z. Suo, "Ionic skin", *Advanced Materials*, Vol. 26, No. 45, pp. 7608–7614, 2014.

49. Huang, Y., D. Fang, C. Wu, W. Wang, X. Guo and P. Liu, "A flexible touch-pressure sensor array with wireless transmission system for robotic skin", *Review of Scientific Instruments*, Vol. 87, No. 6, p. 065007, 2016.

50. Ulmen, J. and M. Cutkosky, “A robust, low-cost and low-noise artificial skin for human-friendly robots”, *2010 IEEE International conference on robotics and automation*, pp. 4836–4841, IEEE, 2010.

51. Korkut, D., K. Erdil, Ö. G. Akcan, B. Muslu, E. A. Baran and Y. D. Gökdel, “Silicone Mold Implementation for High-Sensitive Detection of Strain Sensing using Paper-Based Piezoresistive System”, *2020 IEEE International Conference on Flexible and Printable Sensors and Systems (FLEPS)*, pp. 1–4, IEEE, 2020.

52. Erdil, K., D. Korkut, Ö. G. Akcan, B. Muslu, Y. D. Gökdel and E. A. Baran, “Flexible Linear Absolute Encoder System for Force Localization in Soft Environments”, *2020 IEEE International Conference on Flexible and Printable Sensors and Systems (FLEPS)*, pp. 1–4, IEEE, 2020.

53. Ostchega, Y., R. J. Prineas, C. Dillon, M. McDowell and M. Carroll, “Estimating equations and tables for adult mid-arm circumference based on measured height and weight: data from the third National Health and Nutrition Examination Survey (NHANES III) and NHANES 1999–2000”, *Blood pressure monitoring*, Vol. 9, No. 3, pp. 123–131, 2004.

54. Abdouni, A., G. Moreau, R. Vargiolu and H. Zahouani, “Static and active tactile perception and touch anisotropy: aging and gender effect”, *Scientific reports*, Vol. 8, No. 1, pp. 1–11, 2018.

55. Liu, C., *Foundations of MEMS*, Pearson Education India, 2012.

56. Jhung, M. J. and S. O. Yu, “Study on modal characteristics of perforated shell using effective Young’s modulus”, *Nuclear engineering and design*, Vol. 241, No. 6, pp. 2026–2033, 2011.

57. Jhung, M. J. and K. H. Jeong, “Free vibration analysis of perforated plate with square penetration pattern using equivalent material properties”, *Nuclear Engineering and Technology*, Vol. 47, No. 4, pp. 500–511, 2015.

58. Carvalho, F. C. and J. F. Labuz, “Experiments on effective elastic modulus of two-dimensional solids with cracks and holes”, *International Journal of Solids and Structures*, Vol. 33, No. 28, pp. 4119–4130, 1996.

59. Wang, J. C., “Young’s modulus of porous materials”, *Journal of materials science*, Vol. 19, No. 3, pp. 801–808, 1984.

60. Kachanov, M., I. Tsukrov and B. Shafiro, “Effective moduli of solids with cavities of various shapes”, , 1994.

61. Wu, Y., I. Karakurt, L. Beker, Y. Kubota, R. Xu, K. Y. Ho, S. Zhao, J. Zhong, M. Zhang, X. Wang *et al.*, “Piezoresistive stretchable strain sensors with human machine interface demonstrations”, *Sensors and Actuators A: Physical*, Vol. 279, pp. 46–52, 2018.

62. Erdil, K., T. AYRAÇ, Ö. G. AKCAN and Y. D. GÖKDEL, “Piezoresistive disposable weight sensor with increased sensitivity”, *Turkish Journal of Electrical Engineering & Computer Sciences*, Vol. 28, No. 2, 2020.

63. Sparavigna, A. C. *et al.*, “based Metamaterials: Honeycomb and Auxetic Structures”, *International Journal of Sciences*, Vol. 3, No. 11, pp. 22–25, 2014.

64. Liu, X., M. Mwangi, X. Li, M. O’Brien and G. M. Whitesides, “based piezoresistive MEMS sensors”, *Lab on a Chip*, Vol. 11, No. 13, pp. 2189–2196, 2011.

65. Sekertekin, Y., I. Bozyel and D. Gokcen, “A flexible and low-cost tactile sensor produced by screen printing of carbon black/PVA composite on cellulose paper”, *Sensors*, Vol. 20, No. 10, p. 2908, 2020.

66. Lamas-Ardisana, P. J., P. Casuso, I. Fernandez-Gauna, G. Martínez-Paredes, E. Jubete, L. Añorga, G. Cabañero and H. J. Grande, “Disposable electrochemical paper-based devices fully fabricated by screen-printing technique”, *Electrochemistry Communications*, Vol. 75, pp. 25–28, 2017.

67. Güder, F., A. Ainla, J. Redston, B. Mosadegh, A. Glavan, T. Martin and G. M. Whitesides, "Paper-based electrical respiration sensor", *Angewandte Chemie International Edition*, Vol. 55, No. 19, pp. 5727–5732, 2016.

68. Li, Y., Y. Wang, S. Chen, Z. Wang and L. Feng, "Inkjet-printed paper-based sensor array for highly accurate pH sensing", *Analytica Chimica Acta*, Vol. 1154, p. 338275, 2021.

69. Armas, S. M., A. J. Manhan, O. Younce, P. Calvo-Marzal and K. Y. Chumbimuni-Torres, "Ready-to-use single-strip paper based sensor for multiplex ion detection", *Sensors and Actuators B: Chemical*, Vol. 255, pp. 1781–1787, 2018.

70. Cai, L., C. Xu, S. Lin, J. Luo, M. Wu and F. Yang, "A simple paper-based sensor fabricated by selective wet etching of silanized filter paper using a paper mask", *Biomicrofluidics*, Vol. 8, No. 5, p. 056504, 2014.

71. Zhu, Z., H. Zhang, K. Xia and Z. Xu, "Hand-drawn variable resistor and strain sensor on paper", *Microelectronic Engineering*, Vol. 191, pp. 72–76, 2018.

72. Ren, T.-L., H. Tian, D. Xie and Y. Yang, "Flexible graphite-on-paper piezoresistive sensors", *Sensors*, Vol. 12, No. 5, pp. 6685–6694, 2012.

73. Zhao, H., T. Zhang, R. Qi, J. Dai, S. Liu and T. Fei, "Drawn on paper: a reproducible humidity sensitive device by handwriting", *ACS applied materials & interfaces*, Vol. 9, No. 33, pp. 28002–28009, 2017.

74. Erdil, K., *Design and fabrication of a low-cost piezoresistive MEMS biosensor for aflatoxin detection*, Ph.D. Thesis, 2021.

75. Tan, X., Y. Lv, X. Zhou, Y. Wang, X. Song, G. Gu, P. Ji, X. Yang, B. Shen, Z. Feng *et al.*, "AlGaN/GaN pressure sensor with a Wheatstone bridge structure", *AIP Advances*, Vol. 8, No. 8, p. 085202, 2018.

76. Mathur, H., V. Agarwal and K. Sengar, "Finite Element Analysis of MEMS based Piezoresistive Diamond Thin Film Cantilever Pressure Sensor", *International Research Journal of Engineering and Technology*, Vol. 4, No. 02, 2017.

77. Wang, Y., L. Zhu, D. Mei and W. Zhu, "A highly flexible tactile sensor with an interlocked truncated sawtooth structure based on stretchable graphene/silver/silicone rubber composites", *Journal of Materials Chemistry C*, Vol. 7, No. 28, pp. 8669–8679, 2019.

78. Choi, W.-C., "Polymer micromachined flexible tactile sensor for three-axial loads detection", *Transactions on electrical and electronic materials*, Vol. 11, No. 3, pp. 130–133, 2010.

79. Wang, Y., K. Xi, D. Mei, G. Liang and Z. Chen, "A flexible tactile sensor array based on pressure conductive rubber for contact force measurement and slip detection", *Journal of Robotics and Mechatronics*, Vol. 28, No. 3, pp. 378–385, 2016.

APPENDIX A: MANUFACTURING OF THE SILK STENCILS

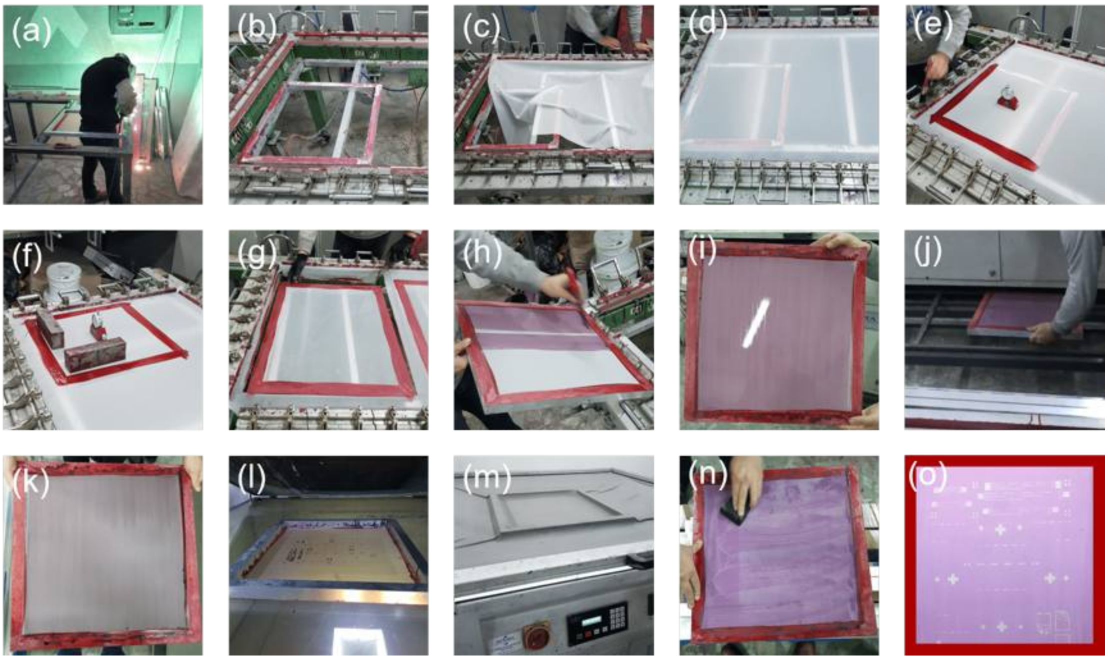

Figure A.1: The production stages of the silk stencil which using for the fabrication method of screen-printing.

(a) welding the frame.
(b) silk stretching platform.
(c) placing the silk onto the platform.
(d) stretched silk.
(e) applying an adhesive paste to bond the silk to the frame.
(f) weights loading to strengthen the bond.
(g) cutting the silk along with the frame out.
(h) applying emulsion paint.
(i) emulsified mask.
(j) emulsion drying for a while.
(k) dried emulsified .
(l) positive photolithography process.
(m) exposing UV.
(n) removing with the water
(o) ready to use view of the silk stencil.

APPENDIX B: DATASHEETS

B.1. Graphite

Bare Conductive

Electric Paint®

Technical Data Sheet
English

PRODUCT DESCRIPTION

Electric Paint is a nontoxic, water based, water soluble, electrically conductive paint. It can be used in circuits as a painted resistor element, a capacitive electrode or can function as a conductor in designs that can tolerate high resistivity. It is intended for applications with circuits using low DC voltages at low currents. **Electric Paint** adheres to a wide variety of substrates and can be applied using screen printing equipment. Its major benefits include low cost, solubility in water and good screen life. It is black in colour and can be over-painted with any material compatible with a water-based paint.

ADVANTAGES / PRODUCT BENEFITS

- High sheet resistance
- Nontoxic
- Water-soluble
- Can be used to create capacitive touch and proximity sensors
- Can be used as a potentiometer or resistive circuit element
- Compatible with many standard screen printing processes
- Low cost

TYPICAL PROPERTIES

Colour /	Black
Viscosity /	Highly viscous and shear sensitive (thixotropic)
Density /	1.16 g/ml
Sheet Resistance /	55Ω/sq at 50 micron film thickness
Vehicle /	Water-based
Drying Temperature /	**Electric Paint** should be allowed to dry at room temperature for 5 – 15 minutes. Drying time can be reduced by placing Electric Paint under a warm lamp or other low intensity heat source.

See below summary table of typical properties.

PROCESSING AND HANDLING

Screen Printing Equipment /	Manual
Screen Types /	Polyester, stainless steel (43T – 90T gauge mesh)
Typical Cure Conditions /	Room temperature (24°C) for 15 minutes
Typical Circuit Line Width /	0.5 – 10mm (43T-mesh stainless steel screen)
Clean-up Solvent /	Warm water and soap
Sheet Resistance /	Approximately 32Ω/sq when using a brush or manual screen printing
Shelf Life /	6 months after opening
Storage /	**Electric Paint** should be stored, tightly sealed in a clean, stable environment at room temperature. Composition should be thoroughly mixed prior to use.

See below graph to predict resistance using manual screen printing.

First Floor, 98 Commercial St
London E1 6LZ, United Kingdom
+44 0 207 650 7977
info@bareconductive.com

1

B.2. Silver Ink

Product Name	conductive sliver paint
Package size	153mm*93mm*95mm
Side resistance	<0.1ohms/@1mil
175-200mesh	inch monofilament polyester mesh
165-250mesh	inch stainless steel wire mesh
Curing time	71°C for 30min,93°C for 15min,121°C for 5min
Model	BK-426

B.3. Dual Edge Connector

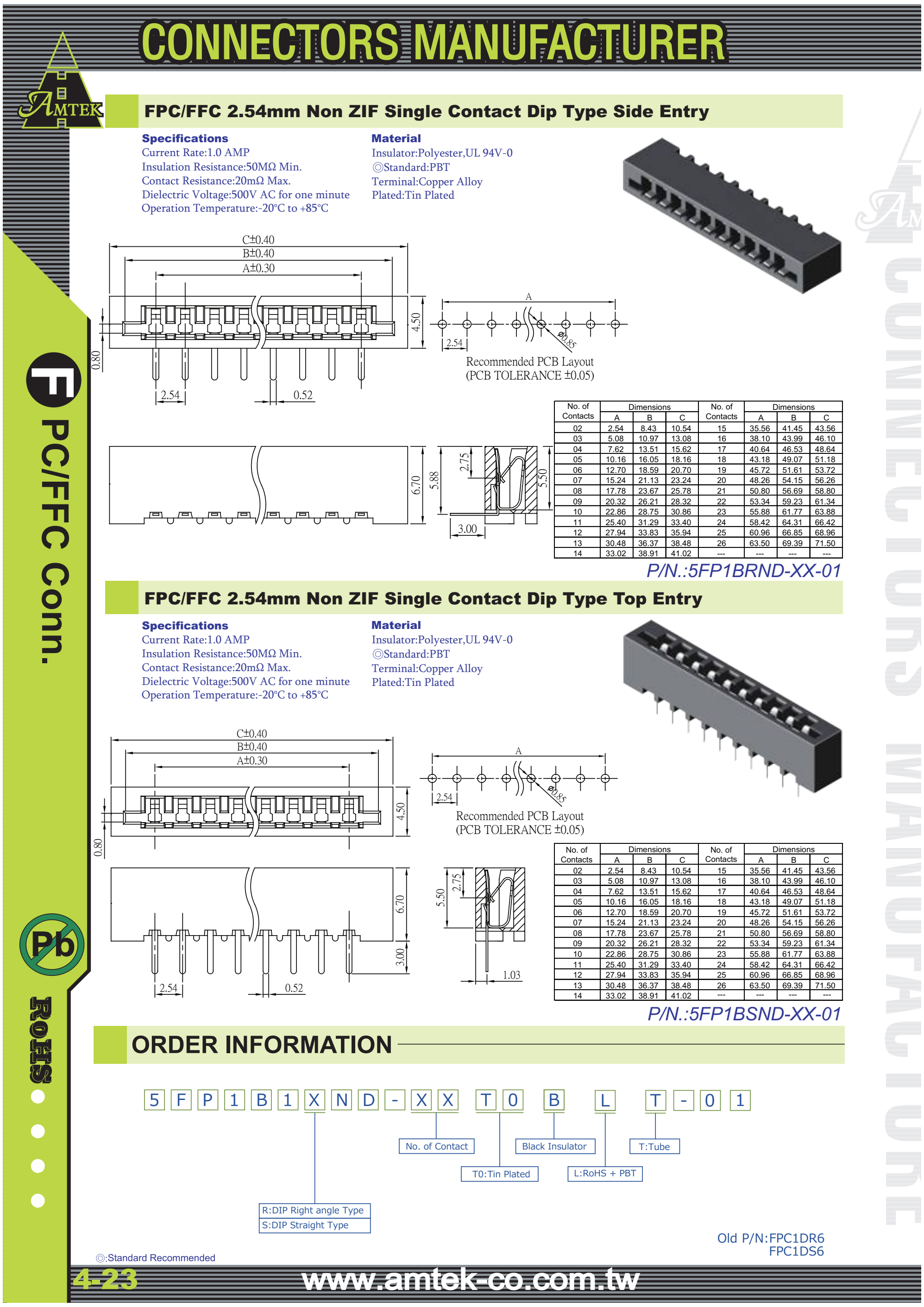

CONNECTORS MANUFACTURER

AMTEK

FPC/FFC Conn.

Pb RoHS

FPC/FFC 2.54mm Non ZIF Single Contact Dip Type Side Entry

Specifications
Current Rate:1.0 AMP
Insulation Resistance:50MΩ Min.
Contact Resistance:20mΩ Max.
Dielectric Voltage:500V AC for one minute
Operation Temperature:-20°C to +85°C

Material
Insulator:Polyester,UL 94V-0
◎Standard:PBT
Terminal:Copper Alloy
Plated:Tin Plated

C±0.40
B±0.40
A±0.30
4.50
0.80
2.54
0.52
A
2.54
ø0.85
Recommended PCB Layout
(PCB TOLERANCE ±0.05)
6.70
5.88
2.75
5.50
3.00

No. of Contacts	Dimensions A	Dimensions B	Dimensions C	No. of Contacts	Dimensions A	Dimensions B	Dimensions C
02	2.54	8.43	10.54	15	35.56	41.45	43.56
03	5.08	10.97	13.08	16	38.10	43.99	46.10
04	7.62	13.51	15.62	17	40.64	46.53	48.64
05	10.16	16.05	18.16	18	43.18	49.07	51.18
06	12.70	18.59	20.70	19	45.72	51.61	53.72
07	15.24	21.13	23.24	20	48.26	54.15	56.26
08	17.78	23.67	25.78	21	50.80	56.69	58.80
09	20.32	26.21	28.32	22	53.34	59.23	61.34
10	22.86	28.75	30.86	23	55.88	61.77	63.88
11	25.40	31.29	33.40	24	58.42	64.31	66.42
12	27.94	33.83	35.94	25	60.96	66.85	68.96
13	30.48	36.37	38.48	26	63.50	69.39	71.50
14	33.02	38.91	41.02	---	---	---	---

P/N.:5FP1BRND-XX-01

FPC/FFC 2.54mm Non ZIF Single Contact Dip Type Top Entry

Specifications
Current Rate:1.0 AMP
Insulation Resistance:50MΩ Min.
Contact Resistance:20mΩ Max.
Dielectric Voltage:500V AC for one minute
Operation Temperature:-20°C to +85°C

Material
Insulator:Polyester,UL 94V-0
◎Standard:PBT
Terminal:Copper Alloy
Plated:Tin Plated

C±0.40
B±0.40
A±0.30
4.50
0.80
A
2.54
ø0.85
Recommended PCB Layout
(PCB TOLERANCE ±0.05)
6.70
5.50
2.75
3.00
2.54
0.52
1.03

No. of Contacts	Dimensions A	Dimensions B	Dimensions C	No. of Contacts	Dimensions A	Dimensions B	Dimensions C
02	2.54	8.43	10.54	15	35.56	41.45	43.56
03	5.08	10.97	13.08	16	38.10	43.99	46.10
04	7.62	13.51	15.62	17	40.64	46.53	48.64
05	10.16	16.05	18.16	18	43.18	49.07	51.18
06	12.70	18.59	20.70	19	45.72	51.61	53.72
07	15.24	21.13	23.24	20	48.26	54.15	56.26
08	17.78	23.67	25.78	21	50.80	56.69	58.80
09	20.32	26.21	28.32	22	53.34	59.23	61.34
10	22.86	28.75	30.86	23	55.88	61.77	63.88
11	25.40	31.29	33.40	24	58.42	64.31	66.42
12	27.94	33.83	35.94	25	60.96	66.85	68.96
13	30.48	36.37	38.48	26	63.50	69.39	71.50
14	33.02	38.91	41.02	---	---	---	---

P/N.:5FP1BSND-XX-01

ORDER INFORMATION

5 F P 1 B 1 X N D - X X T 0 B L T - 0 1

No. of Contact
Black Insulator
T:Tube
T0:Tin Plated
L:RoHS + PBT
R:DIP Right angle Type
S:DIP Straight Type

Old P/N:FPC1DR6
FPC1DS6

◎:Standard Recommended

4-23 www.amtek-co.com.tw

B.4. Silicone Mold

APPENDIX C: Main Algorithm

```
#include "KMotionDef.h"
#include "MotionControl.h"
#include "MotionControl.c"


struct MotorStruct  M1, M2, M3, M4;
struct FilterStruct VOBM1, VOBM2, VOBM3, VOBM4;
struct FilterStruct AOBM1, AOBM2, AOBM3, AOBM4;
struct FilterStruct DOBM1, DOBM2, DOBM3, DOBM4;
struct FilterStruct FOBM1, FOBM2, FOBM3, FOBM4;
struct FilterStruct LPFX1, LPFX2, LPFX3, LPFX4,
struct FilterStruct LPFY1, LPFY2, LPFY3, LPFY4;
struct ABGStruct ABG1, ABG2;

double Scope00[10500],Scope01[10500],Scope02[10500],Scope03[10500];
double Scope04[10500],Scope05[10500],Scope06[10500],Scope07[10500];
double Scope08[10500],Scope09[10500],Scope10[10500],Scope11[10500];
double Scope12[10500],Scope13[10500],Scope14[10500],Scope15[10500];
double T0, dT, TNew, T1, Time, TOff,TOld;
double AccDesM1, AccDesM2, AccDesM3, AccDesM4;
double SatM1, SatM2, SatM3, SatM4;
double Pos_X_ref, Pos_Y_ref, Pos_R_ref;
double Vel_X_ref, Vel_Y_ref, Vel_R_ref;
double Acc_X_ref, Acc_Y_ref, Acc_R_ref;
double Pos_M1_ref, Pos_M2_ref, Pos_M3_ref, Pos_M4_ref;
double Vel_M1_ref, Vel_M2_ref, Vel_M3_ref, Vel_M4_ref;
double Acc_M1_ref, Acc_M2_ref, Acc_M3_ref, Acc_M4_ref;
double EndTime, w, r;
double C, K;
double T;
double M1CompCur, M2CompCur, M3CompCur, M4CompCur;
double M1CompCurF, M2CompCurF, M3CompCurF, M4CompCurF;
double M1CompCurF0, M2CompCurF0, M3CompCurF0, M4CompCurF0 = 0;
double AccS1X, AccS2X, AccS3X, AccS4X;
double AccS1Y, AccS2Y, AccS3Y, AccS4Y;
```

```
double NewMean1X, NewMean2X, NewMean3X, NewMean4X;
double NewMean1Y, NewMean2Y, NewMean3Y, NewMean4Y;
double OldMean1X, OldMean2X, OldMean3X, OldMean4X;
double OldMean1Y, OldMean2Y, OldMean3Y, OldMean4Y;
double AccXFromEnc, AccYFromEnc, AccRFromEnc;
double AccXFromAcc, AccYFromAcc,AccRFromAcc;
double AccXdiff, AccYdiff, AccRdiff;
double M1DriftAcc, M2DriftAcc, M3DriftAcc, M4DriftAcc;
double HomePos1, HomePos2, HomePos3, HomePos4, DummyVar1,DummyVar2;
int AccMeanCount = 0;
int DummyM1,DummyM2,DummyM3,DummyM4;
int Counter = 0;
int Array;
int ExpLength = 10500;
int PrintingIndex;
int Ind;
int pi =3.14159265359;



main()
{

  dT = 0.00036;

  T0 = Time_sec();
  TOld = Time_sec();

  ch0->InputMode=ENCODER_MODE;
  EnableAxis(0);

  FILE *FilePointer1;
  FILE *FilePointer2;
  char String1[256];
  char String2[256];


```

```
M1.Kn = 0.0414;
M2.Kn = 0.0414;
M3.Kn = 11.64;

M1.Mn = 0.000004108;
M2.Mn = 0.000004108;
M3.Mn = 0.240;

M1.T = dT;
M2.T = dT;
M3.T = dT;

VOBM1.G = 2500;
VOBM2.G = 2500;
VOBM3.G = 2500;

AOBM1.G = 1500;
AOBM2.G = 1500;
AOBM3.G = 1500;

DOBM1.G = 2500;
DOBM2.G = 2500;
DOBM3.G = 2500;

FOBM1.G = 1500;
FOBM2.G = 1500;
FOBM3.G = 1500;

LPFX1.G = 1000;
LPFX2.G = 1000;
LPFX3.G = 1000;
LPFX4.G = 1000;
LPFY1.G = 1000;
LPFY2.G = 1000;
LPFY3.G = 1000;
LPFY4.G = 1000;

```

```
VOBM1.T = dT;
VOBM2.T = dT;
VOBM3.T = dT;

AOBM1.T = dT;
AOBM2.T = dT;
AOBM3.T = dT;

DOBM1.T = dT;
DOBM2.T = dT;
DOBM3.T = dT;

FOBM1.T = dT;
FOBM2.T = dT;
FOBM3.T = dT;

SatM1 = 1.2;   // Max value = 2.4
SatM2 = 1.2;   // Max value = 2.4
SatM3 = 1;     // Max value = 2.4

K = 500;
C = 5;
EndTime = 30;

HomePos1 = ch0->Position/122230.9962945;
HomePos2 = ch1->Position/122230.9962945;
HomePos3 = ch2->Position/2000000;

M1.Pos[0] = 0;
M2.Pos[0] = 0;
M3.Pos[0] = 0;

M1.Pos[1] = 0;
M2.Pos[1] = 0;
M3.Pos[1] = 0;
```

```
M1.Vel[0] = 0;
M2.Vel[0] = 0;
M3.Vel[0] = 0;

M1.Vel[1] = 0;
M2.Vel[1] = 0;
M3.Vel[1] = 0;

M1.Acc[0] = 0;
M2.Acc[0] = 0;
M3.Acc[0] = 0;

M1.Acc[1] = 0;
M2.Acc[1] = 0;
M3.Acc[1] = 0;

M1.IDis[0] = 0;
M2.IDis[0] = 0;
M3.IDis[0] = 0;

M1.IDis[1] = 0;
M2.IDis[1] = 0;
M3.IDis[1] = 0;

M1.IDes[0] = 0;
M2.IDes[0] = 0;
M3.IDes[0] = 0;

M1.IDes[1] = 0;
M2.IDes[1] = 0;
M3.IDes[1] = 0;

M1.IRef[0] = 0;
M2.IRef[0] = 0;
M3.IRef[0] = 0;
```

```
M1.IRef[1] = 0;
M2.IRef[1] = 0;
M3.IRef[1] = 0;

M1.IAct[0] = 0;
M2.IAct[0] = 0;
M3.IAct[0] = 0;

M1.IAct[1] = 0;
M2.IAct[1] = 0;
M3.IAct[1] = 0;

DAC(0,0);
DAC(1,0);
DAC(6,0);

dT=0.000720;

M1.T     = dT;
M2.T     = dT;
M3.T     = dT;
VOBM1.T  = dT;
VOBM2.T  = dT;
VOBM3.T  = dT;
AOBM1.T  = dT;
AOBM2.T  = dT;
AOBM3.T  = dT;
DOBM1.T  = dT;
DOBM2.T  = dT;
DOBM3.T  = dT;
FOBM1.T  = dT;
FOBM2.T  = dT;
FOBM3.T  = dT;
```

```
for (Ind = 0; Ind<ExpLength; Ind = Ind+1)

{

  Time = Time_sec()-T0;
  TNew = Time_sec();          // Get current Time(in while loop it gets
 time at every second)

  M1.Pos[0] = ch0->Position/122230.9962945 - HomePos1;
  M2.Pos[0] = ch1->Position/122230.9962945 - HomePos2;
  M3.Pos[0] = ch2->Position/2000000 - HomePos3;

  M1.Vel[0] = VOB(&M1,&VOBM1);
  M2.Vel[0] = VOB(&M2,&VOBM2);
  M3.Vel[0] = VOB(&M3,&VOBM3);

  M1.Acc[0] = AOB(&M1,&AOBM1);
  M2.Acc[0] = AOB(&M2,&AOBM2);
  M3.Acc[0] = AOB(&M3,&AOBM3);

  M1.IDis[0] = DOB(&M1,&DOBM1);
  M2.IDis[0] = DOB(&M2,&DOBM2);
  M3.IDis[0] = DOB(&M3,&DOBM3);

  M1.For[0] = FOB(&M1,&FOBM1);
  M2.For[0] = FOB(&M2,&FOBM2);
  M3.For[0] = FOB(&M3,&FOBM3);

  if (Time>EndTime)
  {
    DAC(0,0);
    DAC(1,0);
    DAC(6,0);
    break;
  }


```

```
    //AccDesM1=0;
    //AccDesM2=0;
    //AccDesM3=0;

    AccDesM1 = -0.8*sin(2*Time) + 19*(0.4*cos(2*Time)-M1.Vel[0]) + 30*(0.20*sin(2*Time)-M1.Pos[0]);    // POSITION CONTROL
    AccDesM2 = 0.8*sin(2*Time) + 18*(-0.4*cos(2*Time)-M2.Vel[0]) + 30*(-0.20*sin(2*Time)-M2.Pos[0]);   // POSITION CONTROL
    AccDesM3 = 50*(0.02-M3.Vel[0]);      // VELOCITY CONTROL
    //AccDesM3 = 0.04*sin(2*Time) + 10*(-0.02*cos(2*Time)-M3.Vel[0]) + 30*(-0.01*sin(2*Time)-M3.Pos[0]);// POSITION CONTROL


    M1.IDes[0] = AccDesM1*(M1.Mn/M1.Kn);
    M2.IDes[0] = AccDesM2*(M2.Mn/M2.Kn);
    M3.IDes[0] = AccDesM3*(M3.Mn/M3.Kn);

    M1.IRef[0] = M1.IDes[0] + M1.IDis[0];
    M2.IRef[0] = M2.IDes[0] + M2.IDis[0];
    M3.IRef[0] = M3.IDes[0] + M3.IDis[0];

    M1.IAct[0] = Saturate(M1.IRef[0],SatM1);
    M2.IAct[0] = Saturate(M2.IRef[0],SatM2);
    M3.IAct[0] = Saturate(M3.IRef[0],SatM3);

    DummyM1 = (int)(M1.IAct[0]*-853);
    DummyM2 = (int)(M2.IAct[0]*-853);
    DummyM3 = (int)(M3.IAct[0]*853);

    DAC(0,DummyM1);
    DAC(1,DummyM2);
    DAC(6,DummyM3);
```

```
    Scope00[Counter] = Time;          // Experiment Time Value
    Scope01[Counter] = dT;            // dT Value
    Scope02[Counter] = M1.Pos[0];     // M1 Position Value
    Scope03[Counter] = M2.Pos[0];     // M2 Position Value
    Scope04[Counter] = M1.Vel[0];     // M1 Velocity Value
    Scope05[Counter] = M2.Vel[0];     // M2 Velocity Value
    Scope06[Counter] = M1.Acc[0];     // M1 Acceleration Value
    Scope07[Counter] = M2.Acc[0];     // M2 Acceleration Value
    Scope08[Counter] = M3.Pos[0];     // M3 Position Value
    Scope09[Counter] = M3.Vel[0];     // M3 Velocity Value
    Scope10[Counter] = M3.Acc[0];     // M3 Acceleration Value
    Scope11[Counter] = M3.For[0];     // M3 Force Value
    Scope12[Counter] = 0;
    Scope13[Counter] = 0;
    Scope14[Counter] = 0;
    Scope15[Counter] = 0;

    Counter = Counter+1;
    AccMeanCount = AccMeanCount+1;

    UpdateMotor(&M1);
    UpdateMotor(&M2);
    UpdateMotor(&M3);

    dT = TNew - TOld;             // dT Calculation
    TOld = TNew;

    WaitNextTimeSlice();
}

    DAC(0,0);
    DAC(1,0);
    DAC(6,0);
```

```
if(Counter<=(ExpLength-1))        // For Loop Break Condition
    {
    for(Array=Counter;Array<ExpLength;Array=Array+1)     // Write into the
    File
    {
      Scope00[Array] = 0;      // Experiment Time Value
      Scope01[Array] = 0;      // dT Value
      Scope02[Array] = 0;      // M1 Position Value (Pantograph)
      Scope03[Array] = 0;      // M2 Position Value (Pantograph)
      Scope04[Array] = 0;      // M1 Velocity Value (Pantograph)
      Scope05[Array] = 0;      // M2 Velocity Value (Pantograph)
      Scope06[Array] = 0;      // M1 Acceleration Value (Pantograph)
      Scope07[Array] = 0;      // M2 Acceleration Value (Pantograph)
      Scope08[Array] = 0;      // M3 Position Value (Linear)
      Scope09[Array] = 0;      // M3 Velocity Value (Linear)
      Scope10[Array] = 0;      // M3 Acceleration Value (Linear)
      Scope11[Array] = 0;      // M3 Force Value (Linear)
      Scope12[Array] = 0;
      Scope13[Array] = 0;
      Scope14[Array] = 0;
      Scope15[Array] = 0;
        }  // for close
  } // if close

  printf("%s \n","Writing Datas into the File has begun.");
    FilePointer1=fopen("C:\\Users\\student\\Desktop\\Experiments\\
   Experiments_2020_21_25(Position Check)\\TempExperiment08a.txt","wt");
       // Open the File
  for(PrintingIndex=0;PrintingIndex<ExpLength;PrintingIndex=PrintingIndex
   +1)              // Write into the File
    {
      fprintf(String1,"%f %f %f %f %f %f %f %f\n",Scope00[PrintingIndex],
   Scope01[PrintingIndex],Scope02[PrintingIndex],Scope03[PrintingIndex],
   Scope04[PrintingIndex],Scope05[PrintingIndex],Scope06[PrintingIndex],
   Scope07[PrintingIndex]);
  }
  fclose(FilePointer1);
```

```
    FilePointer2=fopen("C:\\Users\\student\\Desktop\\Experiments\\Experiments_2020_21_25(Position Check)\\TempExperiment08b.txt","wt"); // Open the File
  for(PrintingIndex=0;PrintingIndex<ExpLength;PrintingIndex=PrintingIndex+1)              // Write into the File
    {
      fprintf(String1,"%f %f %f %f %f %f %f %f\n",Scope08[PrintingIndex],Scope09[PrintingIndex],Scope10[PrintingIndex],Scope11[PrintingIndex],Scope12[PrintingIndex],Scope13[PrintingIndex],Scope14[PrintingIndex],Scope15[PrintingIndex]);
  }
  fclose(FilePointer2);

}
```

APPENDIX D: Main Algorithm Library-1

```
double VOB(struct MotorStruct *MS, struct FilterStruct *FS) // Filtered velocity estimation using "Backward Euler"
{return LPF(MS,FS,(1/MS->T)*(MS->Pos[0]-MS->Pos[1]));}

double AOB(struct MotorStruct *MS, struct FilterStruct *FS) // Filtered acceleration estimation using "Backward Euler"
{return LPF(MS,FS,(1/MS->T)*(MS->Vel[0]-MS->Vel[1]));}

double FOB(struct MotorStruct *MS, struct FilterStruct *FS) // Reaction Force estimation using "Backward Euler"
{return((LPF(MS,FS,((MS->IAct[0]*MS->Kn)+(MS->Vel[0]*MS->Mn*FS->G)))-(MS->Vel[0]*MS->Mn*FS->G)));}

double DOB(struct MotorStruct *MS, struct FilterStruct *FS) // Disturbance observer using "Backward Euler"
{return((1/MS->Kn)*(LPF(MS,FS,((MS->IAct[0]*MS->Kn)+(MS->Vel[0]*MS->Mn*FS->G)))-(MS->Vel[0]*MS->Mn*FS->G)));}

double LPF(struct MotorStruct *MS, struct FilterStruct *FS, double U0) // Low pass filter using "Backward Euler"
{
  FS->Y0 = (FS->Y1+FS->G*MS->T*U0)/(FS->G*MS->T+1);
  FS->Y1 = FS->Y0;
  FS->U1 = U0;
  return FS->Y0;
}

double INT(struct IntegratorStruct *IS, double U0) // Integrator "Backward Euler"
{
  IS->Y0 = IS->T*U0+IS->Y1;
  IS->Y1 = IS->Y0;
  IS->U1 = U0;
  return IS->Y0;
}
```

```
double Saturate(double I, double Sat_Level)
{
  if (I>Sat_Level)
  {
    I = Sat_Level;
  }
  else if (I<(-1*Sat_Level))
  {
    I = -1*Sat_Level;
  }
  return I;
}

double Signum(double Inp)
{
  double S;
  if (Inp>0)
  {
    S=1;
  }
  else if (Inp<0)
  {
    S=-1;
  }
  else if (Inp==0)
  {
    S=0;
  }
  return S;
}

double Absolute(double Inp)
{
  double S;
  if (Inp>0)
  {
    S=Inp;
```

```
  }
  else if (Inp<0)
  {
    S=(-1)*Inp;
  }
  else if (Inp==0)
  {
    S=0;
  }
  return S;
}
double Sgm(double x)
{

  //  Modified Sigmoid Function (2*S-1)
  double f;
  double a;

  a=1/(1+exp(-x));

  f=2*a-1;

  return f;
}

double Sgmd(double x)
{
  ////Derivative of Modified Sigmoid Function
  double f;
  double a;
  double b;
  //// If x is a function, numerator should be multiply with derivative
     of x in MainAlgorithm
  b=1/(1+exp(-x));
  a=exp(-x)/(1+exp(-x));
  f=2*a*b;

```

```
  return f;
}

double tanh(double x)
{
  ////Hyperbolic Tangent Function
  double f;

  f=(exp(-2*x)-1)/(exp(-2*x)+1);

  return f;
}

double tanhd(double x)
{
  //// Derivative of Hyperbolic Tangent Function
  double a;
  double f;

  //// If x is a function, numerator should be multiply with derivative
    of x in MainAlgorithm

  a=(2*exp(x))/(exp(2*x)+1);

  f=a*a;

  return f;
}

void ForwardKinematics(struct RobotStruct *RS)
{
  double M = (RS->Pos2 - RS->Pos1)/(2*RS->H);
  double N = (pow(RS->Pos1,2) - pow(RS->Pos2,2))/(4*RS->H);
  double A = M*M+1;
}
```

APPENDIX E: Main Algorithm Library-2

```
#define MOTORMEMO 3          // MOTORMEMO-1 defines the number of previous steps to be stored.
#define ROBOTMEMO 3          // MOTORMEMO-1 defines the number of previous steps to be stored.
#define BUFFLENGTH 200

struct MotorStruct
{
  double T;                  // Incremental time step;
  double Kn;                 // Nominal torque constant of the motor
  double Mn;                 // Nominal motor inertia
  double Pos[MOTORMEMO];         // Current motor position array (while calling write: Pos[i] for the ith previous step)
  double Vel[MOTORMEMO];         // Current motor velocity array (while calling write: Vel[i] for the ith previous step)
  double Acc[MOTORMEMO];         // Current motor acceleration array (while calling write: Acc[i] for the ith previous step)
  double For[MOTORMEMO];         // Current reaction force acting on the motor(while calling write: For[i] for the ith previous step)
  double Dis[MOTORMEMO];         // Current disturbance force over the motor (while calling write: Dis[i] for the ith previous step)
  double IDes[MOTORMEMO];        // Desired input current to the motor (Generated by the controller)
  double IDis[MOTORMEMO];        // Disturbance current over the motor (DOB output)
  double IRef[MOTORMEMO];        // Input current reference to the motor (IRef = IDes + IDis)
  double IAct[MOTORMEMO];        // Actual current input of the motor (Saturated IRef)
  double Der[MOTORMEMO];
  double Forc[MOTORMEMO];
};

struct RobotStruct
{
```

```
  double T;             // Sampling time
  double L;             // Length of the connection arms
  double H;             // Offset distance to center of two motors

  double PosX[ROBOTMEMO];      // End effector X position
  double PosY[ROBOTMEMO];      // End effector Y position
  double Pos1[ROBOTMEMO];
  double Pos2[ROBOTMEMO];
  double VelX[ROBOTMEMO];
  double VelY[ROBOTMEMO];
  double Vel1[ROBOTMEMO];
  double Vel2[ROBOTMEMO];
  double AccX[ROBOTMEMO];
  double AccY[ROBOTMEMO];
  double Acc1[ROBOTMEMO];      // Acceleration of Joint-1
  double Acc2[ROBOTMEMO];      // Acceleration of Joint-2
  double ForX[ROBOTMEMO];
  double ForY[ROBOTMEMO];
  double For1[ROBOTMEMO];
  double For2[ROBOTMEMO];
};

struct ABGStruct
{
  double T;           // Sampling Period
  double Al;          // Alpha Coefficient
  double Be;          // Beta Coefficient
  double Ga;          // Gamma Coefficient
  double X0;          // Old Position
  double V0;          // Old Velocity
  double A0;          // Old Acceleration
  double XM;          // Measured Data
  double R0;          // Residual Error
  double X1;          // New Position
  double V1;          // New Velocity
  double A1;          // New Acceleration
};
```

```
void UpdateMotor(struct MotorStruct * MS)
{
  int i;
  for(i=1;i<MOTORMEMO;i++)
  {
    MS->Pos[MOTORMEMO-i]=MS->Pos[MOTORMEMO-i-1];
    MS->Vel[MOTORMEMO-i]=MS->Vel[MOTORMEMO-i-1];
    MS->Acc[MOTORMEMO-i]=MS->Acc[MOTORMEMO-i-1];
    MS->For[MOTORMEMO-i]=MS->For[MOTORMEMO-i-1];
    MS->Dis[MOTORMEMO-i]=MS->Dis[MOTORMEMO-i-1];
    MS->IDes[MOTORMEMO-i]=MS->IDes[MOTORMEMO-i-1];
    MS->IDis[MOTORMEMO-i]=MS->IDis[MOTORMEMO-i-1];
    MS->IRef[MOTORMEMO-i]=MS->IRef[MOTORMEMO-i-1];
    MS->IAct[MOTORMEMO-i]=MS->IAct[MOTORMEMO-i-1];
    MS->Der[MOTORMEMO-i]=MS->Der[MOTORMEMO-i-1];
    MS->Forc[MOTORMEMO-i]=MS->Forc[MOTORMEMO-i-1];
  }
};

void UpdateRobot(struct RobotStruct * RS)
{
  int i;
  for(i=1;i<ROBOTMEMO;i++)
  {
    RS->PosX[ROBOTMEMO-i]=RS->PosX[ROBOTMEMO-i-1];
    RS->PosY[ROBOTMEMO-i]=RS->PosY[ROBOTMEMO-i-1];
    RS->Pos1[ROBOTMEMO-i]=RS->Pos1[ROBOTMEMO-i-1];
    RS->Pos2[ROBOTMEMO-i]=RS->Pos2[ROBOTMEMO-i-1];
    RS->VelX[ROBOTMEMO-i]=RS->VelX[ROBOTMEMO-i-1];
    RS->VelY[ROBOTMEMO-i]=RS->VelY[ROBOTMEMO-i-1];
    RS->Vel1[ROBOTMEMO-i]=RS->Vel1[ROBOTMEMO-i-1];
    RS->Vel2[ROBOTMEMO-i]=RS->Vel2[ROBOTMEMO-i-1];
    RS->AccX[ROBOTMEMO-i]=RS->AccX[ROBOTMEMO-i-1];
    RS->AccY[ROBOTMEMO-i]=RS->AccY[ROBOTMEMO-i-1];
    RS->Acc1[ROBOTMEMO-i]=RS->Acc1[ROBOTMEMO-i-1];
    RS->Acc2[ROBOTMEMO-i]=RS->Acc2[ROBOTMEMO-i-1];
    RS->ForX[ROBOTMEMO-i]=RS->ForX[ROBOTMEMO-i-1];
```

```
    RS->ForY[ROBOTMEMO-i]=RS->ForY[ROBOTMEMO-i-1];
    RS->For1[ROBOTMEMO-i]=RS->For1[ROBOTMEMO-i-1];
    RS->For2[ROBOTMEMO-i]=RS->For2[ROBOTMEMO-i-1];
  }
};

struct FilterStruct
{
  double T;          // Sampling Period
  double G;          // Gain of Filter
  double U0;         // Current Input Value
  double U1;         // Previous Input Value
  double Y0;         // Current Output Value
  double Y1;         // Previous Output Value
};

struct IntegratorStruct
{
  double T;          // Sampling Period
  double U0;         // Current Input Value
  double U1;         // Previous Input Value
  double Y0;         // Current Output Value
  double Y1;         // Previous Output Value
};

double VOB(struct MotorStruct *MS, struct FilterStruct *FS);
double AOB(struct MotorStruct *MS, struct FilterStruct *FS);
double FOB(struct MotorStruct *MS, struct FilterStruct *FS);
double DOB(struct MotorStruct *MS, struct FilterStruct *FS);
double LPF(struct MotorStruct *MS, struct FilterStruct *FS, double U0);
double INT(struct IntegratorStruct *IS, double U0);
double Sgm(double x);
double Sgmd(double x);



double Saturate(double I, double Sat_Level);
```

```
double Signum(double Inp);
double Absolute(double Inp);
double tanh(double x);
double tanhd(double x);

void ForwardKinematics(struct RobotStruct *RS);
```